

Erasmia Lyka

Magdalen College

Supervised by:

Professor Constantin-C. Coussios

Passive Acoustic Mapping for Improved Detection and Localisation of Cavitation Activity

A thesis submitted to the Department of Engineering Science
for the degree of Doctor of Philosophy

October 2016

ABSTRACT

Passive acoustic mapping (PAM) is a novel method for monitoring ultrasound therapies by mapping sources of acoustic activity, and in most cases cavitation activity, using an array of detectors. Although the range of its applications is indicative of its great potential, clinical adoption is currently hindered by its limited spatial resolution and the inherent difficulty of distinguishing, at depth, between nonlinear signals arising from nonlinear propagation and those arising from processes such as cavitation. The objective of this thesis is to address this limitation, by improving both the detection of the signal-of-interest and the source localisation.

An optimum data-adaptive array beamforming algorithm is proposed, Robust Beamforming by Linear Programming (RLPB), which exploits the higher-order-statistics of the recorded signals, aiming at improving PAM source localisation. Both simulations and *in vitro* experimentation demonstrated improvement in PAM spatial resolution compared to a previously introduced algorithm, Robust Capon Beamformer. More specifically, under the *in vitro* conditions examined here, a 22% and 14% increase in the axial and transverse PAM resolution is respectively achieved.

In terms of reliable signal-of-interest detection amongst interfering signals, a time-domain data-adaptive parametric model, Sum-of-Harmonics (SOH) model, is developed. This model enables accurate estimation of time-varying-amplitude narrowband components in the presence of broadband signals. Respectively, it can recover a weak broadband signal in the presence of a dominant narrowband component. Compared to conventional comb filtering, SOH model enables PAM of cavitation sources that better reflect their physical location and extent.

PAM performance enhancement achieved by combining the proposed beamforming and filtering approaches is assessed in a context where spatial resolution really matters, namely for distinguishing between cavitation activity occurring inside a channel and perivascularly following cavitation-mediated extravasation. Adoption of the proposed method results in more accurate isolation of the broadband emissions from inertially cavitating sources, and more reliable localisation of these sources despite the long source-to-array distance has been observed. Such an improvement to the spatial accuracy of PAM paves the way towards its clinical translation, and *in vivo* experimentation is the next step for further validation of PAM in conjunction with the proposed methods under clinically relevant conditions.

STATEMENT OF ORIGINALITY

I hereby declare that this submission is my own work and, to the best of my knowledge, it contains no materials previously published or written by another person, or substantial proportions of material which have been accepted for the award of any other degree of diploma at the University of Oxford or any other educational institution, except where due acknowledgement is made in the thesis.

Any contribution made to the research by others, with whom I have worked at the University of Oxford or elsewhere, is explicitly acknowledged in the thesis.

I also declare that the intellectual content of this thesis is a product of my own work, except to the extent that assistance from others in the project's design and conception or in style, presentation and linguistic expression is acknowledged.

Erasmia Lyka

October 2016

ACKNOWLEDGEMENTS

Undertaking this DPhil has been one of the most challenging, but at the same time rewarding experiences of my life. First and foremost, I would like to thank my supervisor, Professor Constantin-C. Coussios, who has been a constant source of inspiration and motivation to pursue my research. At one of my first formal college dinners Constantin told me that as a first-year DPhil student he will teach me, as a second-year student we will teach each other, and as a third-year student I will have the chance to teach him. It has been a great honour and privilege to work with Constantin both as a Master's and a DPhil student, and I hope I managed to live up to his expectations and he is proud of our work.

I would especially like to thank Dr Christian Coviello for his generous and constant support, as well as patience, throughout my DPhil. His passion for signal processing has been fundamental in shaping the direction of my research. It has been a privilege and joy for me to collaborate with such an experienced researcher.

Additionally, I would like to thank Professor Richard Kozick from Bucknell University for his valuable guidance and feedback throughout the development and validation of the Sum-of-Harmonics model.

I am also very grateful to be part of the BUBBL group. Having the opportunity to interact daily with such an interesting and diverse group of people had a significant impact on the quality of my work. More specifically, I would like to thank Catherine Paverd for the amazing collaboration we had during the last months of my DPhil, Dr Delphine Elbes for the countless enjoyable moments we shared during experiments, and Dr Michael Gray for the valuable discussions and feedback during the last year of my DPhil. My experience as a DPhil student would not have been the same if it was not for a specific group of colleagues with whom I shared a lot of coffee breaks, and had the most incredible discussions. Finally, I would like to acknowledge the contribution of our workshop technicians, Jim Fisk and David Salisbury, whose help on different aspects of my project has been valuable.

At this point I would like to say a heartfelt thank you to my parents, Dimitris and Sotiria, and my sister Thomi, to whom this thesis is dedicated. Their unconditional love and support guided me through all the difficult times of this journey, and my achievements are partly theirs as well.

Finally, a very special thank you to my best friend and other better half, Nikos, for his love and unceasing support. Sharing every moment of this journey with him made it much more enjoyable. His humour and positive attitude has served as a key source of encouragement for me.

RESEARCH DISSEMINATION

Peer-Reviewed Journal Papers

E. Lyka, C. Coviello, R. Kozick, C.-C. Coussios, "*Sum-of-harmonics method for improved narrowband and broadband signal quantification during passive monitoring of ultrasound therapies*", The Journal of the Acoustical Society of America, 140, 741-754 (2016)

E. Lyka, C. Coviello, C.-C. Coussios, "*Optimal higher-order-statistics-based beamforming for passive acoustic mapping*" (in preparation)

Conference Presentations

E. Lyka, D. Elbes, C. Coviello, R. Cleveland, C.-C. Coussios ,"*Monitoring of non-cavitational HIFU thermal ablation in ex-vivo ox liver using Passive Acoustic Mapping*", The 16th International Symposium on Therapeutic Ultrasound, Tel Aviv, Israel, 14-16 March 2016.

E. Lyka, C. Coviello, R. Kozick, C.-C. Coussios, "*A sum-of-harmonics time-domain method to distinguish harmonic and broadband signals during passive acoustic mapping of ultrasound therapies"*, The Journal of the Acoustical Society of America, 137, 2399 (169th Meeting of the Acoustical Society of America – 18-22 May, 2015)

CONTENTS

1. Introduction **1**
1.1. Non-invasive therapeutic ultrasound **1**
1.2. Mechanisms of ultrasound therapies **3**
1.2.1. Non-linear propagation **4**
1.2.2. Thermal mechanisms **5**
1.2.3. Mechanical effects and Acoustic Cavitation **7**
1.2.4. Therapeutic ultrasound applications and challenges **12**
1.3. Treatment monitoring **15**
1.3.1. Magnetic Resonance Imaging **15**
1.3.2. Active Ultrasound Imaging **18**
1.3.3. Passive Acoustic Monitoring **25**
1.4. Passive Acoustic Mapping (PAM) **28**
1.4.1. Passive Acoustic Mapping Principles **29**
1.4.2. Beamforming techniques for Passive Acoustic Mapping **39**
1.4.2.1. Time Exposure Acoustics (TEA) **39**
1.4.2.2. Data-adaptive Beamformers **43**
1.5. Project aims and objectives **49**
1.6. Thesis Outline **52**
1.7. References **53**
2. Optimal passive beamforming using higher order statistics **60**
2.1. Introduction **60**
2.2. Higher-order-statistics-based beamforming **62**
2.2.1. Introduction to Higher-Order-Statistics (HOS) **62**
2.2.2. Robust Beamforming by Linear Programming (RLPB) **63**
2.3. Numerical Simulations **69**
2.4. Experimental Results **84**
2.4.1. Experimental rationale **84**
2.4.2. Experimental apparatus **85**
2.5. Signal Processing **89**
2.5.1. Experimental Procedure **89**
2.5.2. Passive Beamforming **91**
2.6. Experimental Results **92**
2.6.1. Axial Resolution **92**
2.6.2. Transverse Resolution **96**
2.7. Conclusions **100**
2.8. References **103**
3. Sum-of-harmonics method for improved narrowband and broadband signal quantification during passive monitoring of ultrasound therapies **105**
3.1. Introduction **105**
3.2. Theory **108**
3.2.1. Initial Sum-of-harmonics (SOH) model **108**

3.2.2. Modified Sum-of-harmonics (SOH) model **112**
3.3. Numerical Simulations **114**
3.4. Experimental results **119**
3.4.1. Experimental setup **119**
3.4.2. Signal filtering **121**
3.4.3. Passive Acoustic Mapping **129**
3.5. Conclusions **136**
3.6. References **139**
4. Improved Passive Acoustic Mapping of cavitation following vascular extravasation **140**
4.1. Introduction **140**
4.2. Experimental methods **142**
4.2.1. Fluorescent sub-micron cavitation nuclei **142**
4.2.2. Experimental apparatus **143**
4.2.3. Experimental procedure **146**
4.2.4. Mapping of cavitation activity **150**
4.2.5. Signal processing and beamforming **151**
4.3. Experimental results **154**
4.4. Conclusions **183**
4.5. References **186**
5. Conclusions & Future work **187**
5.1. Conclusions **188**
5.2. Future work **195**

LIST OF FIGURES

Figure 1.1: Schematic of the steps of the PAM algorithm **34**
Figure 1.2: Example PAM maps (TEA and RCB) of cavitation activity **50**
Figure 2.1: Schematic representation of the simulated acoustic signal pathway **74**
Figure 2.2: Signal pathway components for single source energy estimation **77**
Figure 2.3: PAM spatial resolution simulation results (two single sources) **80**
Figure 2.4: Effect of parameter ε in PAM spatial resolution (simulations) **83**
Figure 2.5: PAM source resolvability - *in vitro* experimental setup **86**
Figure 2.6: PVC tubing configuration in *in vitro* experiments **87**
Figure 2.7: PAM axial resolution results for RCB and RLPB **94**
Figure 2.8: PAM axial resolution analysis based on Rayleigh's criterion **95**
Figure 2.9: PAM transverse resolution results for RCB and RLPB **97**
Figure 2.10: PAM transverse resolution analysis based on Rayleigh's criterion **99**
Figure 3.1: Effect of different parameters on SOH performance (simulations) **117**
Figure 3.2: *In vitro* experimental setup for SOH-PAM performance assessment **119**
Figure 3.3: Comb filters of different order comparison **124**
Figure 3.4: SOH vs comb filtering for broadband signal estimation **126**
Figure 3.5: PCD power spectra with increasing pressure **127**
Figure 3.6: Frequency spectra of signals filtered with SOH or comb filtering **128**
Figure 3.7: PAM for SOH and comb filtering – water in the pipette **131**
Figure 3.8: PAM for SOH and comb filtering – NCs in the pipette **134**
Figure 4.1: Inertial cavitation thresholds of NCs at different frequencies **143**
Figure 4.2: *In vitro* experimental setup of vascular extravasation mapping **145**
Figure 4.3: Schematic of experimental procedure **146**
Figure 4.4: Data analysis steps with different filtering and beamforming methods **152**
Figure 4.5: B-mode co-registration **154**
Figure 4.6: PAM maps for experimental set 1 (1^{st} insonation) **157**
Figure 4.7: PAM maps quantitative analysis - Set 1 (1^{st} insonation) **159**
Figure 4.8: PAM maps quantitative analysis (-3dB energy) - Set1 (1^{st} insonation) **161**
Figure 4.9: PAM maps for experimental set 1 (2^{nd} insonation) **163**
Figure 4.10: Spectral analysis of RF signal (set 1, 2^{nd} insonation) **164**
Figure 4.11: PAM overlaid with microscopy (set 1, 2^{nd} insonation, probe 1 & 2) **166**
Figure 4.12: PAM maps quantitative analysis - Set 1 (2^{nd} insonation) **168**
Figure 4.13: PAM maps for experimental set 2 (1^{st} insonation) **170**
Figure 4.14: Spectral analysis of RF signal (set 2, 1^{st} insonation) **171**
Figure 4.15: PAM maps quantitative analysis - Set 2 (1^{st} insonation) **172**
Figure 4.16: PAM maps for experimental set 2 (2^{nd} insonation) **174**
Figure 4.17: Spectral analysis of RF signal (set 2, 2^{nd} insonation) **175**
Figure 4.18: PAM overlaid with microscopy (set 2, 2^{nd} insonation, probe 2) **177**
Figure 4.19: PAM maps quantitative analysis - Set 2 (2^{nd} insonation) **178**
Figure 4.20: Bright field microscopy (set 3) **180**
Figure 4.21: PAM maps for experimental set 3 (2^{nd} insonation) **181**
Figure 4.22: Spectral analysis of RF signal (set 3, 2^{nd} insonation) **183**

LIST OF TABLES

Table 1.1: PAM algorithm key equations transformed into matrix format **43**
Table 2.1: Keller-Miksis and PAM simulation parameters – source energy **75**
Table 2.2: Keller-Miksis and PAM simulation parameters – source resolvability **79**
Table 2.3: In vitro experimental parameters- PAM spatial resolution assessment **88**
Table 3.1: Numerical simulations parameters **116**
Table 4.1: *In vitro* experimental parameters **149**

ACRONYMS

CPU	Central Processing Unit
GPU	Graphics Processing Unit
HIFU	High Intensity Focussed Ultrasound
MEG	Magnetoencephalography
MRI	Magnetic Resonance Imaging
PAM	Passive Acoustic Mapping
PSF	Point spread function
RCB	Robust Capon Beamforming
RF	Radio Frequency
RLPB	Robust Linear Programming Beamformer
ROI	Region of interest
SOH	Sum of Harmonics
TEA	Time Exposure Acoustics
TRITC	Tetramethylrhodamine

CHAPTER



INTRODUCTION

1.1 NON-INVASIVE THERAPEUTIC ULTRASOUND

Ultrasound, defined as propagating perturbations in pressure or density possessing frequency components above the threshold for human hearing, namely 20kHz, has traditionally been perceived as a diagnostic modality. The first published evidence of the use of ultrasound for medical imaging is found as early as 1942, when Dussik et al. published the first transcranial ultrasound image. This work motivated further early investigations of the interaction of ultrasound with tissue.

Over the years, significant improvements in diagnostic ultrasound, correlated with advances in electronics and signal processing theory, have been reported, leading to the establishment of ultrasound as one of the most widely used imaging modalities. The low cost and portability of ultrasound equipment, along with the fact that it does not have biological side-effects and provides real-time images of the mechanical

structures of the body and the dynamic motion of different organs, led to its widespread adoption compared to other modalities, such as X-ray, CT, and MRI (Szabo, 2004).

The idea of using ultrasound for medical imaging was quickly succeeded by the suggestion of applying ultrasound for therapeutic purposes. The bioeffects caused by ultrasound targeted and delivered non-invasively to the body were first introduced by Wood and Loomis (1927), and the first published evidence of applying focused therapeutic ultrasound in humans was in the field of neurosurgery (Fry and Fry, 1960). However, further adoption of the technique was hindered by the introduction of the L-dopa drug which was considered a more widely accepted treatment. Unlike diagnostic ultrasound, advances in therapeutic ultrasound followed a rather slower pace, mainly due to the limitations of the early equipment, the lack of treatment monitoring and control methodologies, the necessity in the early neurological applications of surgical intervention to remove part of the skull, and in some cases the appearance of a competing treatment.

By the 1970s, therapeutic ultrasound re-gained significant attention, becoming established in fields such as physiotherapy. The introduction of new transducer designs and materials that were able to provide improved focussing of high intensity ultrasound beams led to increased research and experimentation in the fields of neurosurgery (Wells, 1977) and cancer treatment (Kremkau, 1979). Since then, progress in the field of therapeutic ultrasound has kept up with technological improvements, especially in the fields of imaging, transducer technologies, signal processing and electronics. The range of applications has been dramatically expanded, and it currently covers areas such as localised tissue heating for treatment of solid tumours (Kennedy, 2005; ter Haar, 2007; ter Haar and Coussios, 2007a), targeted drug delivery for cancer treatment

(Carlisle et al., 2013; Liang et al., 2010; Mo et al., 2012), mechanical disruption of the blood-brain barrier (Hynynen et al., 2001a; McDannold et al., 2008), sonothrombolysis for stroke treatment (Alexandrov et al., 2008), and tissue fractionation (histotripsy) for tissue de-bulking or orthopaedic applications (Roberts et al., 2006). However, in order for ultrasound therapies to dominate in the clinical arena, there are still important challenges that need to be addressed, relating to treatment monitoring and control for maximising efficacy and minimising side effects.

The rest of the chapter is dedicated to discussing the mechanisms with which ultrasound interacts with tissue, in order to understand the ultrasound bioeffects associated with each of the aforementioned application areas. Currently available treatment monitoring techniques are then discussed, before presenting the key objectives of the present work alongside an outline of the thesis.

1.2 MECHANISMS OF ULTRASOUND THERAPIES

As ultrasound propagates through tissue and interacts with it, a set of mechanisms are triggered which are responsible for specific bioeffects. Depending on the application, different mechanisms are considered more beneficial, and the choice of the appropriate ultrasound parameters, in particular, excitation frequency, amplitude, pulse duration and repetition frequency will allow certain mechanisms to dominate over others. In this section, a review of these mechanisms is presented, along with their associated bioeffects.

1.2.1 NON-LINEAR PROPAGATION

The majority of therapeutic ultrasound treatments employ sufficiently large pressure amplitudes that they can no longer be considered small compared to the ambient state. In this nonlinear regime, as an ultrasound wave propagates through tissue, it becomes gradually distorted. The instantaneous velocity at a specific point in a medium depends on both the speed of sound and the local particle velocity, and the part of the waveform during the compressional phase, when the particle velocity is positive (in the direction of the wave propagation), travels faster compared to the part of the waveform that corresponds to the rarefactional phase, in which the particle velocity is negative (in the opposite direction of the wave propagation) (Muir and Carstensen, 1980). Through this process, an initially single-frequency sinusoid is gradually distorted into a sawtooth wave.

This gradual steepening of the waveform is known as shock formation. The distance required for shock formation for a progressive plane wave with sinusoid waveform is defined by the shock parameter σ (Muir and Carstensen, 1980):

$$\sigma = \beta \varepsilon k x \tag{1.1}$$

where β is the coefficient of nonlinearity of the medium, ε is the Mach number and it is equal to $p_0/\rho_0 c_0^2$, p_0 is the source pressure amplitude, ρ_0 the density of the medium, and c_0 the speed of sound in the medium. k is the acoustic wavenumber and is being defined as $2\pi/\lambda$, where λ is the wavelength of the waveform. Finally, x is the distance that the wave has propagated. When $\sigma \ll 1$, nonlinearity is considered negligible. As σ approaches unity and while $\sigma < 1$, nonlinearity becomes important, and by the time $\sigma > 1$ shocks are forming. This process, known as non-linear propagation, results

in part of the energy of the wave being transferred from the fundamental frequency f_0 to its harmonics. It is prevalent at higher frequencies, at elevated excitation amplitudes, and for long propagation distances into tissue.

The generation of higher frequencies due to nonlinear propagation also has an effect on the amplitude of the waveform due to the relationship between attenuation and frequency, $a = a_0|f|^n$. Attenuation is usually considered proportional to $f^{1.1}$ in tissue (Narayana and Ophir, 1983), and in the presence of nonlinear mechanisms the incident wave is more readily attenuated as more energy leaks out to higher harmonics. This has significant implications both for the delivery and monitoring of ultrasound therapies, as discussed in greater detail below, since the acoustic signal-of-interest, either to be delivered for therapeutic purposes or to be detected for monitoring purposes, is significantly attenuated.

1.2.2 THERMAL MECHANISMS

Therapeutic ultrasound, and more specifically High-Intensity Focused Ultrasound (HIFU), has been clinically shown to increase local heating rates deep into tissue through tight focusing of ultrasound energy (Kennedy, 2005). The key mechanism creating this thermal effect is attenuation, which arises from a combination of scattering and absorption. As the acoustic wave propagates through a medium, part of the incident ultrasonic energy is converted into heat through viscous absorption. An approximate formula that is widely used for estimation of the energy deposition per unit volume and time due to an ultrasound field, and applicable only in the case of plane waves (Clarke and ter Haar, 1997) is:

$$q = 2a(f)I_0 \tag{1.2}$$

where $a(f)$ denotes the frequency-dependent attenuation coefficient of the medium, and I_0 is the acoustic intensity at the focus of the acoustic source.

Under the effect of nonlinear propagation, as previously described, energy is redistributed to higher frequencies, which are more readily absorbed (Bacon and Carstensen, 1990). Simultaneously, assuming an inhomogeneous medium, scattering of both the linear and nonlinear components of the incident wave will occur, resulting in an increased wave propagation path through the medium that once again leads to greater attenuation and absorption.

When tissue temperature exceeds the body temperature, namely 37^{o}C, different bioeffects are observed. Depending on the temperature rise, the rate and duration of heating, the tissue damage caused could be either reversible or irreversible. In HIFU tissue ablation, the goal is to deposit enough heat in tissue in order to cause cell death due to protein denaturation (Lepock et al., 1993). Under specific exposure conditions, this process of protein structure disruption is permanent, leading to tissue necrosis and the formation of lesions. In order to assess in clinically relevant terms the thermal damage induced, a thermal dose parameter has been suggested by Sapareto and Dewey (1984) that is widely used, and it aims at describing the thermal tolerance of cells during hyperthermia treatments. This thermal dose parameter, known as Cumulative Equivalent Minutes (CEM), integrates the temperature profile of tissue over time, and establishes an equivalent exposure time at a reference temperature, most commonly 43^{o}C, in order to induce the same biological effects (Sapareto and Dewey, 1984; Nandlall et al., 2009).

$$CEM_{43} = \int_0^{t_{total}} R(T)^{43-T} dt \qquad (1.3)$$
$$R(T) = \begin{cases} 0.5 & T \geq 43℃ \\ 0.25 & T < 43℃ \end{cases}$$

A typical threshold value of CEM_{43} for kidney and liver damage is 340min (Graham et al., 1999).

1.2.3 MECHANICAL EFFECTS AND ACOUSTIC CAVITATION

There are several mechanical effects of ultrasound, including acoustic radiation force (Eller, 1968) and acoustic streaming (Lighthill, 1978; Nyborg, 1958), that have thus far found limited applicability in the context of therapy. Here, we focus on the main therapeutic mechanical effect, namely acoustic cavitation.

The term 'acoustic cavitation' refers to the oscillations of bubbles present in the sound field under sonication (Neppiras, 1980). Occasionally in the literature the term "cavitation" also encompasses the concept of nucleation, but in the present work, these two phenomena are clearly distinguished.

By defining nucleation, what is essentially defined is the origin of the bubbles in the medium. Theoretically, bubbles could form in a liquid, when the induced acoustic pressure overcomes the tensile strength of the liquid. This process is known as "homogeneous nucleation", and it is not usually expected in real tissue, since it assumes that the liquid is perfect with no inhomogeneities and requires pressures of a magnitude not encountered in biomedical ultrasound (Apfel, 1981). A more realistic theory for acoustic nucleation arises from either of the two following situations: small gas bubbles

pre-existing on the surface of impurities in the liquid, and imperfectly wet crevices on surfaces and boundaries acting as nucleation sites (Harvey et al., 1944; Apfel, 1970; Atchley and Prosperetti, 1989). The combination of the above two conditions significantly enhances the probability of acoustic nucleation, since now, the pressure required to overcome the tensile strength of the liquid is significantly reduced.

Bubble oscillations can be either linear or nonlinear. In the linear case under exposure to low-amplitude pressure waves, bubbles behave in a way analogous to that of a mass-spring-damper system (mass = inertia of the surrounding medium, spring = compressibility of gas, damper = viscous/thermal/damping losses). Like all second-order mechanical systems, in a linear regime bubbles exhibit a resonance frequency,

$$f_0 = \frac{1}{2\pi}\sqrt{\frac{3\gamma P_0}{\rho R_0^2} + \frac{4\sigma}{\rho R_0^3}} \tag{1.4}$$

where f_0 is the resonance frequency, γ the polytropic exponent for the gas, P_0 the ambient pressure, ρ the density of the medium, σ the surface tension at the liquid-gas interface, and R_0 the equilibrium radius in the absence of ultrasound (Minnaert, 1933; Brennen, 1995). In the linear regime, the bubble will scatter the incident wave in a linear fashion. Therefore, the frequency of the scattered wave will be the same as that of the incident wave, and the amplitude of the scattered wave will be maximized when the frequency of the incident wave is equal to the resonance frequency of the bubble.

In the nonlinear regime, bubbles perform non-symmetric, large excursions from their equilibrium radius, with the level of how nonlinear their behaviour is depending mostly on their size, the amplitude and frequency of the incident wave, and the properties of the surrounding medium. This results in a scattered wave that is no longer

the output of a linear relationship with respect to the frequency of the incident wave (Neppiras, 1980; Holt and Crum, 1992; Leighton, 1995, 1997). Pre-existing small bubbles or other nucleated cavities can also grow in size through a process known as rectified diffusion. This process can be described by two complementary effects, the area and shell effect, both related to the changes in bubble surface area over time. In one oscillatory cycle the pressure difference between the inside and outside area of a bubble causes gas to diffuse in and out of the bubble during the rarefactional and compressional phase respectively. However, since the transferal interface, i.e. the area of the bubble wall, is larger during the rarefactional compared to the compressional phase, more gas is pumped in the bubble from the surrounding liquid than the gas diffused out of the bubble leading to a net mass and radius increase. This is known as area effect, and it is one of the factors that contribute to bubble growth due to rectified diffusion. The second factor is shell effect and it refers to the variations in thickness of the liquid shell surrounding the bubble due to bubble contraction and expansion. Such variations result in changes in the concentration gradient across the bubble wall, and the net effect caused is the same as in the case of the area effect.

Depending on the level of the excitation pressure, the acoustic response of a bubble may vary significantly, and the bubble behaviour could be associated with different physical effects and types of acoustic emissions. Two main regimes of acoustic cavitation are identified at this point: non-inertial and inertial cavitation. Non-inertial cavitation is characterized by repetitive linear or nonlinear oscillations over many acoustic cycles. This type of response is expected for gas-filled bubbles of radius equal or larger than the resonant size. The acoustic emissions generated during non-inertial cavitation are characterized by narrowband signals at multiples and fraction

multiples of the excitation frequency, i.e. harmonic, sub- and super-harmonic acoustic emissions owing to the periodicity of the bubble oscillations (Neppiras, 1980; Stride and Coussios, 2010).

On the other hand, inertial cavitation is usually exhibited when the excitation pressure exceeds a certain threshold for a given bubble radius and excitation frequency. This so-called inertial cavitation threshold may in many cases have a rather subjective definition, and there are three criteria that are most commonly used: (i) the maximum bubble radius being equal or larger than twice the initial bubble radius; (ii) the maximum temperature during the bubble collapse exceeding 5000K; and (ii) the bubble wall velocity just before the collapse exceeding the speed of sound in air (Apfel, 1981; Flynn, 1975). In this type of cavitation gas- or vapour-filled bubbles expand unstably during the rarefactional phase and collapse violently during the compressional phase, under the inertia of the surrounding medium. This violent collapse leads to energy radiation and generation of broadband acoustic emissions (Brennen, 1995; Leighton, 1997; Neppiras, 1980).

Acoustic cavitation can induce a variety of thermal and mechanical bioeffects. As far as thermal effects are concerned, cavitation activity in a medium can increase heat deposition due to a combination of physical phenomena (Holt and Roy, 2001; Farny et al., 2010; Khokhlova et al., 2006). Multiple bubbles present in the ultrasound propagation path act as linear and nonlinear scatterers of the incident wave, resulting in increasing propagation distance and therefore, in increased viscous absorption. At the same time, nonlinear bubble oscillations result in higher-harmonics being generated which are more readily absorbed by the medium. Moreover, enhanced heating due to viscous absorption takes place at the boundary layer between an oscillating bubble and

the surrounding liquid, where increased shear stresses are generated. Finally, inertial cavitation is also responsible for increased heat deposition due to the generation of secondary acoustic emissions, which, as already discussed, span a broad frequency range. These broadband emissions at high frequencies are more readily absorbed by the medium due to the frequency dependence of the absorption coefficient (Huisman and Thijssen, 1996).

Cavitation activity is also responsible for a variety of mechanical effects on tissue and cells. Acoustic microstreaming occurs around bubbles undergoing non-inertial oscillations in a sound field, and it is expected at low amplitude excitations and for bubbles of the resonant size being close to boundaries. Steady currents form around the oscillating bubble due to a momentum transfer from the boundary layer to the surrounding liquid, and the flow patterns created depend on the bubble oscillation mode. As a result, shear stresses are imposed on neighbouring structures and surfaces altering the local environment (Kolb and Nyborg, 1956; Nyborg, 1958; Wan et al., 2015). Another important mechanical effect of cavitation activity, and in this case inertial cavitation, is microjetting. The violent collapse of an oscillating bubble could result in generation of high-speed liquid jet directed towards nearby solid surfaces. This phenomenon takes place when a bubble oscillates in an assymetric fashion due to its proximity to a rigid boundary. As the bubble oscillates, it deforms significantly and eventually collapses violently forming a high-speed liquid jet, which travels through the bubble towards the opposite boundary of the bubble (Plesset and Chapman, 1971; Wan et al., 2015).

1.2.4 THERAPEUTIC ULTRASOUND APPLICATIONS AND CHALLENGES

The use of ultrasound in different applications requires the selection of the appropriate exposure parameters that will trigger the right mechanisms in order to induce the desired bioeffects. Several ultrasound-induced bioeffects have already been associated with specific applications, demonstrating the extent and potential of therapeutic ultrasound.

A particularly promising application area of therapeutic ultrasound is the use of the localised heat deposition to destroy cancerous tissue via protein denaturation (ter Haar et al., 1991; Chapelon et al., 1992; Kennedy, 2005; ter Haar and Coussios, 2007a, 2007b). The thermal effects of ultrasound have also been used to induce mild hyperthermia during cancer treatment accompanied with chemotherapy, as it has been found to weaken the tumour cells (Kinoshita and Hynynen, 2006).

As far as cavitation-induced bioeffects are concerned, a plethora of ultrasound-based treatments are reported in the literature for which cavitation activity plays a significant role. HIFU ablation is one of them, where cavitation-induced heating has been proven to facilitate ablation of cancerous tissue (Farny et al., 2010; Holt and Roy, 2001). Dissolution of blood clots using ultrasound, known as sonothrombolysis, has also been extensively investigated. It has been found that cavitation activity, both non-inertial cavitation causing microstreaming (Datta et al., 2006) and inertial cavitation generating significant amounts of energy and inducing mechanical stresses (Soltani et al., 2011), is the key mechanism for the enhancement of the uptake of the thrombolytic drug recombinant plasminogen activator (rt-PA).

Enhanced drug delivery due to ultrasound is another promising area of application of ultrasound, and it relies mainly in the exploitation of the bioeffects induced due to cavitation. It has been demonstrated that inertial cavitation is the key mechanism for targeted delivery and release of different therapeutic agents, such as oncolytic viruses, with and without the use of microbubbles (Carlisle et al., 2013; Unger et al., 2002).

Non-inertial cavitation has also been proven to be beneficial for drug transport in the brain. Promising results have been presented regarding the opening of the blood-brain barrier (BBB) and the transport of drugs due to microstreaming (Hynynen et al., 2005, 2001a; McDannold et al., 2006).

A field related to drug delivery is drug transport through the skin. The use of ultrasound to facilitate penetration of molecules through soft tissues, such as skin, is known as sonophoresis. Low-frequency excitations are pre-dominantly used in this application, and the mechanism that seems to play the key role in the permeability enhancement is inertial cavitation via shock wave formation and microjetting (Mitragotri and Kost, 2004; Bhatnagar et al., 2014).

Another field with a long history, where ultrasound has been clinically established, is lithotripsy. Shockwave lithotripsy applies short duration pulses of very high amplitudes for the treatment of urinary stone disease. Stone fragmentation is mainly achieved via inertial cavitation (Coleman and Saunders, 1993; Sass et al., 1991), but the same mechanism is also responsible for causing haemorrhagic lesions that damage the kidney (Sapozhnikov et al., 2002), and therefore, better control of the exposure parameters is required to avoid tissue damage.

However, in some cases, inertial cavitation-induced soft tissue damage is a desired bioeffect, and the relevant technique is called histotripsy. Tissue erosion or damage is the aim during histotripsy, and it can be achieved via two approaches, cavitation-based or boiling histotripsy. In cavitational histotripsy, mechanical damage is induced due to inertial cavitation of bubble clouds as a result of high-amplitude short-duration excitations, while in boiling histotripsy longer duration high-amplitude excitations are used, resulting in the generation of large (on the order of millimetres) boiling bubbles that cavitate and interact with the incident shock waves causing tissue disintegration (Khokhlova et al., 2015; Xu et al., 2005; Wan et al., 2015).

The wide range of applications highlights the increasing interest that ultrasound attracts as a therapeutic modality, mainly due to its non-invasive nature, low cost, and its applicability over different therapeutic platforms. Although significant results have been reported related to the beneficial bioeffects of ultrasound, important issues have been raised, at the same time, with respect to adverse bioeffects due to overtreatment, such as haemorrhage during lithotripsy due to excessive uncontrolled cavitation, or tissue boiling during HIFU ablation that leads to large potentially uncontrolled lesions. Therefore, the key challenge, common across all the therapeutic ultrasound applications, is the establishment of a reliable monitoring technique that will be integrated in the therapeutic ultrasound system. Ideally this technique will be characterised by high spatio-temporal resolution, it will be non-invasive and cost-effective, and its output could be accurately correlated with the desired bioeffect depending on the application.

1.3 TREATMENT MONITORING

Several imaging modalities have been investigated in the context of monitoring ultrasound therapies, and the two methods that are currently clinically approved and used in various ultrasound treatments is magnetic resonance imaging and ultrasound imaging. Within these two modalities there are variations depending on the monitoring goal. More specifically, several modalities aim at estimating the temperature changes in tissue and they are used in thermal ultrasound treatments. Others focus on lesion detection by assessing the changes in tissue properties. And finally, there is a third category that monitors cavitation activity in order to be correlated with the associated bioeffects.

In the sections that follow magnetic resonance and ultrasound-based monitoring techniques will be discussed, along with their current applications, advantages and disadvantages.

1.3.1 MAGNETIC RESONANCE IMAGING

The first of the two clinically approved monitoring techniques is magnetic resonance imaging (MRI), which according to a general definition is based on measuring the response of atomic particles to high frequency radio waves in a magnetic field. In the context of ultrasound therapies MR thermal monitoring (MR-thermometry) has been established as a real-time non-invasive method for focal region detection of a HIFU transducer, and real-time temperature changes tracking during a HIFU exposure. Thermal dose can be consequently calculated and associated with the extent of tissue

damage allowing more controlled guidance of thermal coagulation therapies (Chung et al., 1999; Graham et al., 1999; Jenne et al., 2012; Quesson et al., 2000).

Excluding cases where fat is involved, MR parameters, such as proton resonance frequency (PRF) shift, diffusion (D) and relaxation (T1), are sensitive to temperature changes; and therefore, MRI, and in most cases PRF- based MRI thermometry is an established technique for three-dimensional temperature mapping (Peters et al., 1998; Rivens et al., 2007). The PRF shift has significantly outperformed the other parameters mainly because it is less dependent on the tissue changes due to rapid heating reaching ablative temperatures, as is the case in HIFU thermal therapies. Its temperature dependence is also linear above 50^{o}C, and therefore, at the ablation-relevant temperatures tissue temperature can be accurately estimated (Hynynen et al., 1996).

Several clinical studies have been reported in the literature where tumour thermal ablation was performed in different parts of the body using MR-guided focused ultrasound (MRgFUS). Treatment of uterine fibroids (Hindley et al., 2004; Stewart et al., 2003), breast fibroadenoma tumour coagulation (Gianfelice et al., 2003; Huber et al., 2001; Hynynen et al., 2001b), metastatic bone tumour treatment for pain palliation (Gianfelice et al., 2008), HIFU thermal ablation of liver tumours (Okada et al., 2006), and brain tumours (Hynynen et al., 2004) are only some of the ultrasound-based treatments that MR thermometry as a monitoring modality has been put in clinical practice.

The main advantage of MRI thermometry is that it is able to provide valuable temperature feedback during ultrasound-based treatments, such as thermal ablation (Senneville et al., 2007), with relatively high temporal and spatial resolution. There is a

trade-off between spatial and temporal requirements that needs to be taken into consideration, i.e. increased spatial resolution comes at a cost of longer image acquisition times and potential motion artefacts, while increased temporal resolution will result in spatial averaging and therefore, potential miscalculation of temperature. Typical resolution values for PRF-based MRI thermometry are sub-Hz and approximately 1mm.

During HIFU ablation the goal is to monitor lesion formation and estimate lesion extent. Therefore, temperature measurements obtained by MR thermometry are combined with models that predict cell death. The most commonly used model is the CEM thermal dose metric (Sapareto and Dewey, 1984) for assessment of heat induced tissue damage. However, this metric has been originally proposed to characterise cell cultures in conditions of mild hyperthermia and low heating rates. In HIFU therapies these conditions are not satisfied anymore, raising concerns regarding the reliability of the metric (Nandlall et al., 2009). Another drawback of MR thermometry is that it cannot be used for non-thermal ultrasound therapies, such as drug delivery for cancer treatment, and that it is incapable of monitoring cavitation, which is a key mechanism in many emerging therapeutic ultrasound applications. Its clinical adoption is also limited due to its inherent high cost of equipment, compatibility issues due to the high magnetic field environment, sensitivity to motion artefacts, and relatively low spatial resolution (1-3mm) (Rivens et al., 2007; Senneville et al., 2007)

1.3.2 ACTIVE ULTRASOUND IMAGING

The second clinically approved technique for monitoring ultrasound-based therapies is active ultrasound imaging, and the different modalities belonging in this category share the same advantages, i.e. the non-invasive nature of ultrasound, its inherently low cost and portable equipment. However, a significant drawback of all these techniques is that they cannot be performed simultaneously with therapy due to the interference of the therapeutic with the diagnostic pulse (Rabkin et al., 2005), resulting in reliability issues.

The simplest, clinically available method of active ultrasound imaging is conventional B-mode ultrasound imaging. This technique involves a multi-element imaging transducer transmitting a wave that propagates through tissue and its echoes are consequently detected by the transducer. It is generally based on the principle of hyperechogenicity (Rivens et al., 2007), i.e. hyperechoic regions appear in a grayscale image due to impedance mismatches at different interfaces present in tissue. Such mismatches result in different portions of the incident signal being reflected back towards the imaging transducer or transmitted further inside the tissue. A characteristic example is the impedance mismatch at the liquid-air interface of bubbles resulting in scattering of the incident sound field, and therefore, detection of the presence of these gas pockets. One of the most common applications of B-mode imaging is in monitoring HIFU ablation, where bright-up areas appearing after exposure of a region on high-intensity ultrasound are correlated with boiling and irreversible tissue damage (Rabkin et al., 2006, 2005). Although hyperechogenicity is considered to be an indicator of

tissue necrosis, the correlation between hyperechogenicity and level of tissue damage is difficult to be accurately defined (Yu and Xu, 2008).

A B-mode image is typically formed by sending a short, broadband pulse from one element on the array on a radial or perpendicular direction with respect to the array, and receiving the echo signals due to reflections from different structures. The received signal in the time domain, known as an A-line, is transformed in the space domain using the speed of sound in the medium, and its amplitude determines the pixel intensity at each corresponding distance from the array. This process is repeated consecutively for all elements of the array in order to form the two-dimensional B-mode image. The above description indicates that the time required for a B-mode to form depends on the number of scans, i.e. A-lines, which is typically equal to the number of elements on the array, and the desired maximum imaging depth. The transmitted pulse frequency is the parameter that determines the axial resolution of B-mode imaging. More specifically, the spatial pulse length is determined by the number of cycles multiplied by the wavelength of the transmitted pulse. As the wavelength becomes shorter (higher frequency), the number of waves of compression and rarefaction for a certain distance increases, and two structures along the axial direction can be distinguished more easily. However, as the frequency increases, so does attenuation, resulting in decreased acoustic wave penetration depth. Therefore, higher frequencies are used mainly in applications where imaging of superficial or small depth structures is required (Chan and Perlas, 2011; Szabo, 2004).

Apart from the basic B-mode imaging approach, several improvements in the image resolution have been suggested and implemented, resulting in widening of the range of clinical applications for this ultrasound imaging modality. The first is

harmonic imaging, and the principle of this technique is to transmit at a frequency f_0 that allows adequate penetration depth, and then use the part of the echo signal that corresponds to the second harmonic, $2f_0$, in order to produce a B-mode image. This technique exploits, in general, the sources of nonlinearity, i.e. nonlinear propagation of the incident wave in tissue (tissue harmonic imaging) (Averkiou, 2001; Thomas and Rubin, 1998), or nonlinear scattering of the incident wave from bubbles and contrast agents (harmonic contrast imaging) (Burns, 1996). Detection of higher harmonics provides both improved signal-to-noise ratio, since linear sources of backpropagated signal, such as interfaces close to the transducer, are rejected, and enhanced spatial resolution due to the narrower beam at the second harmonic. In the context of HIFU, and specifically, in the presence of bubbles, B-mode harmonic contrast imaging is used to monitor cavitation. These cavitating bubbles respond nonlinearly to the incident wave, and act as strong harmonic scatterers. Therefore, the detected signal at the second harmonic provides feedback on the location of the cavitating bubbles with increased spatial resolution and contrast.

However, there are situations where a harmonic signal could be generated near the transducer due to wide transmit bandwidth or nonlinearity of the transducer, leading to linear propagation of the first harmonic as well. This signal will interfere with the desired harmonic signal generated due to nonlinear propagation, and it cannot be filtered out during the receive because it occupies the same frequency band. Reduction of such an undesired interference could be achieved by a method known as pulse inversion. For each A-line two transmissions take place, and the pulse corresponding to the second transmission is the inverted pulse from the first transmission. At the end, the echoes of the two transmissions are summed to obtain the intensity for the specific A-

line, rejecting any linearly responding structure, and improving the signal-to-noise ratio (Chan and Perlas, 2011; Eckersley et al., 2005; Shen et al., 2005).

Another suggested technique for improved contrast in B-mode imaging and clutter reduction is spatial compound imaging. This technique is based on electronic steering of the ultrasound pulses transmitted by the elements of the array in order to image the same area-of-interest from different angles. The ultrasound beams are parallel to each other and their angle with respect to the array varies. The images produced by the different steering angles are averaged to produce the final B-mode image. Despite the improvement in the image quality, this technique is time consuming, as the formation of one image requires multiple acquisitions from all elements of the array (Chan and Perlas, 2011; Jespersen et al., 1998).

The necessity in conventional B-mode imaging to interlace the therapeutic and imaging pulses, as well as the low frame rate of the technique (typically in HIFU at approximately 30Hz) (Khokhlova et al., 2006), does not allow reliable capture of the transient behaviour of bubbles, which might also dissolve in the interval between HIFU turning off and B-mode imaging. Typical values of dissolution time for currently available contrast agents are between 1 and 30ms, which lower than the time required for the formation of a B-mode image (Uhlendorf et al., 2000). An ultrafast active ultrasound imaging technique was recently introduced (Sandrin et al., 1999; Gateau et al., 2011) which, although requiring interlacing with the therapeutic pulse, provides significantly increased frame rate. A single plane wave is emitted by the entire array at once, instead of one pulse from each element consecutively, and the backscattered signals are recorded simultaneously by all the elements of the array. Therefore, a full B-mode image forms after only one transmission-receive sequence. However, the lack of

focussing results in degraded image quality mainly due to reduced signal-to-noise ratio. Coherent plane-wave compounding for ultrafast active ultrasound imaging offered a solution to this problem (Montaldo et al., 2009). By emitting multiple plane waves at different angles, and averaging the backscattered received signals from all angles to form the B-mode image, the signal-to-noise ratio and contrast in the final image is improved, offering a good compromise between image quality and frame rate. The method went one step further in terms of spatial and temporal resolution due to the combination of the plane wave transmission with data-adaptive beamforming algorithms applied on the received signals (Hu et al., 2015). Beamforming allows dynamic receive focusing, and the use of data-adaptive beamforming algorithms enables optimal interference suppression and signal-of-interest power estimation. The concept of beamforming and details on beamforming algorithms will be further presented in the context of passive acoustic mapping later in this chapter. Finally, ultrafast acoustic imaging was combined with pulse-inversion and amplitude modulation techniques for combined improved image quality and frame rate compared to conventional B-mode image, in order to study the complex dynamics of contrast agents (Couture et al., 2009).

Although hyperecho B-mode imaging is a clinically approved and widely used method for monitoring ultrasound-based therapies, its implementation in thermal ultrasound therapies in the absence of cavitation or boiling is hindered by the lack of hyperechoic sources. It has been observed that as temperature increases, tissue echogenicity does not change significantly (Hill and ter Haar, 1995), and unless boiling occurs (Khokhlova et al., 2006) or large bubble populations are present, the method is unreliable (Jensen et al., 2012).

Due to the above limitations, other active ultrasound imaging techniques have been proposed for monitoring HIFU thermal therapies that aim at either estimating changes in tissue temperature or identifying areas of lesioning. The first family of techniques attempts to replace MR thermometry as a lower-cost alternative, and the most promising among these techniques is echo-shift thermometry. It is based on the principle that as temperature increases, the speed of sound, i.e. the compressibility and density of the medium, changes. During B-mode imaging, the speed of sound used is constant and therefore, potential local changes in the speed of sound will cause displacements of structures in the B-mode image. By using correlation techniques, these displacements are quantified and used to estimate the changes in temperature (Miller et al., 2004). However, there are certain limitations associated with this technique, and the most important ones are the artifacts in the displacement calculation due to motion, and the varying temperature dependence of speed of sound in different tissue types. Especially in non-fatty tissues, the speed of sound initially increases as temperature increases but then reaches a plateau at around 60^{o}C and subsequently decreases if the temperature is raised further. This non-monotonic relationship between speed of sound and temperature, and the fact that the regime where this relationship becomes uncertain coincides with the regime where ablation starts occurring, limits the applicability of this method to mild hyperthermia but renders it unsuitable for monitoring HIFU ablation (Bamber and Hill, 1979; Techavipoo et al., 2004).

The second category of active ultrasound monitoring techniques aims at identifying ablated regions, and it is based on the observation that tissue attenuation and stiffness increase when lesioning occurs (Damianou et al., 1997; Jackson et al., 2014). As far as attenuation changes are concerned, a method has been proposed by Ribault et

al. (1998) where changes in the intensity of the received echo signals are correlated with changes in attenuation at corresponding distances in tissue. More promising results were demonstrated with regards to tissue stiffness changes as a measure of lesioning, and one of the associated areas of research is known as radiation force-based monitoring. One of the early proposed techniques was acoustic radiation force imaging (ARFI), which is based on the application of an acoustic radiation force at the focal region, and the subsequent B-mode imaging to identify tissue displacements for estimation of changes in stiffness (Fahey et al., 2004; Lizzi et al., 2003). However, the main limitation of this technique is the difficulty in quantifying displacements due to motion artifacts. Another radiation-force method has been then proposed by (Konofagou and Hynynen, 2003) that applies a harmonic radiation force produced by two focussed ultrasound transducers with overlapping beams at slightly different frequencies. This method, known as harmonic motion imaging, tracks the received echo signals from a diagnostic array at different time stamps, and applies cross-correlation techniques to estimate the tissue oscillatory motion. An improvement to this technique was amplitude-modulated harmonic motion imaging, which requires use of a single transducer for simultaneous treatment and monitoring (Maleke and Konofagou, 2008). The therapeutic pulse is amplitude-modulated by a low-frequency pulse which is responsible for the harmonic acoustic radiation force that results in the harmonic tissue oscillation at the modulation frequency. Finally, an alternative technique for stiffness estimation at high frame rates is supersonic shear wave imaging (Arnal et al., 2011; Bercoff et al., 2004). This method applies an acoustic radiation force to create shear waves, whose speed of propagation through the focal region is then imaged using ultrafast ultrasound imaging, and further associated with changes in tissue stiffness.

1.3.3 PASSIVE ACOUSTIC MONITORING

In the previous section, various techniques falling in the category of active ultrasound imaging were presented, the majority of which require interlacing of the therapeutic and monitoring pulse. This limitation forces a significant compromise in terms of real-time monitoring. More importantly, active imaging *in vivo* can only provide limited information as to the location and extent of cavitation activity, but cannot readily distinguish between non-inertial and inertial cavitation. In therapeutic ultrasound treatments, it is often the detection, maintenance and control of the right type of bubble behaviour that functionally determines the likelihood of success of a therapy.

An alternative approach is passive acoustic monitoring, which is based on recording acoustic signals during ultrasound exposure passively, without requiring diagnostic pulse transmission for monitoring purposes (Greenspan and Tschiegg, 1967; Atchley et al., 1988; Roy et al., 1988; Madanshetty et al., 1991). In a typical clinical setup, this method involves a therapeutic transducer of low or high power and a single-element detection transducer or multi-elements array to provide spatiotemporal information on all linear and non-linear processes taking place during acoustic therapies. Therefore, this technique has the potential to provide real-time monitoring for a wide range of applications of therapeutic ultrasound combined with all the advantages of an ultrasound-based method, i.e. non-invasiveness, and low cost of equipment.

The signals recorded during passive acoustic monitoring could be classified according to their signatures in the frequency domain into narrowband and broadband emissions. Each of these categories is linked to different physical phenomena taking place during sonication. Narrowband emissions correspond to harmonics, sub- or ultra-

harmonics (i.e. integer or fraction multiples) of the driving frequency of the therapeutic transducer, and their origin is non-linear propagation and scattering of the incident wave from tissue structures, gas or vapour bubbles, and non-inertial cavitation (Hamilton and Blackstock, 1998; Muir and Carstensen, 1980; ter Haar and Coussios, 2007a, 2007b). As far as broadband emissions are concerned, they are uniquely associated with inertial cavitation.

Depending on the application and its key underlying mechanism, different component of the emissions is of interest, and isolation of the signal-of-interest is one of the challenges in passive acoustic monitoring. One approach, especially useful in applications where inertial cavitation activity is of interest, involves the use of therapeutic and monitoring transducers with bandwidths that do not overlap. Along with the use of a digital high-pass filter, only the broadband emissions, and more precisely a portion of them, is recorded (McLaughlan et al., 2010). In cases where overlapping bandwidths cannot be avoided, combination of digital high-pass filters, that eliminate interference from linear reflections of the driving frequency, and comb filters applied on the recorded radiofrequency data to filter out harmonics of the transmitted signal, can enable recovery of broadband acoustic emissions (Farny et al., 2009). Equivalent approaches could also be used in order to isolate the narrowband components of the recorded signal.

As already briefly mentioned, passive acoustic monitoring could provide spatial information related to the recorded acoustic emissions by using a multi-element array of passive receivers. Two main approaches have been proposed in the literature in order to achieve this (Gyongy and Coussios, 2010; Salgaonkar et al., 2009). The first approach by (Salgaonkar et al., 2009) used diagnostic ultrasound scanners available at the time to

passively record cavitation activity, and the main limitation of this equipment was that it provided access only to radiofrequency signals post-beamforming. Post-processing of these beamformed signals in the frequency domain was proposed in this method to retrieve source power of different frequency components in space by integrating over a range of frequencies. The main advantage of this technique is related to processing in the frequency domain, which allows direct, convenient filtering of the recorded signals to isolate frequency bands of interest. On the other hand, the use of already beamformed data for source energy estimation compromised the image resolution in the axial direction with respect to the array, since the resolution of this technique in this direction depends on the beamforming configuration, and more specifically on the size of the synthetic focus (Salgaonkar et al., 2009). Finally, the use of Fresnel approximations (Mast, 2007) for the calculation of the signal emissions received by an element on the array due to the presence of a bubble at a certain location, limits the use of this method to mapping of sources in the near field of the array.

The second approach of passive acoustic monitoring proposed by Gyongy and Coussios (2010) utilises the raw, non-beamformed data available by a different diagnostic ultrasound scanner system (z.one, Zonare, Mountain View, CA). Application of conventional or optimal beamforming algorithms in the time domain data allows power estimation of wideband sources in both the near and far field with improved spatial resolution. The next section of this chapter is dedicated in describing in detail the principles of this technique, known as passive acoustic mapping, as well as its applications, advantages and disadvantages.

1.4 PASSIVE ACOUSTIC MAPPING (PAM)

Although it is a recently introduced method in the field of monitoring ultrasound therapies, PAM has already been used in various applications demonstrating its advantages over the competing active ultrasound methods. More specifically, it has already been shown to provide successful monitoring of tissue ablation during HIFU treatments compared to conventional B-mode imaging (Jensen et al., 2012). In addition, a complete method for temperature rise estimation in the region of interest during HIFU exposure using PAM combined with heat deposition modelling has been proposed, which allows prediction of cell death and improved guidance of HIFU treatments (Jensen et al., 2013). In the context of drug delivery, several studies demonstrate the benefits of using PAM in monitoring acoustic emissions related to inertial cavitation that seem to correlate well with drug extravasation and delivery (Choi et al., 2014; Kwan et al., 2015). Another field that PAM made a significant contribution was the analysis of the cavitation dynamics of flowing microbubbles under different acoustic exposure conditions (Choi and Coussios, 2012). Finally, cavitation mapping through the skull using PAM has also been demonstrated, and the artefacts in PAM images due to the presence of skull have been simulated and addressed enabling the use of PAM as a monitoring method of transcranial focused ultrasound treatments, such as sonothrombolysis or cavitation-induced blood-brain barrier disruption (Arvanitis et al., 2013; Jones et al., 2013; O'Reilly et al., 2014).

The sections that follow are dedicated to describing the principles of passive acoustic mapping, emphasizing the different steps required towards the calculation of a source energy map. Special attention is given to the beamforming process involved in

PAM, and the different beamforming algorithms applied in the context of PAM are presented in detail.

1.4.1 PASSIVE ACOUSTIC MAPPING PRINCIPLES

Having its origins in passive sonar used in naval detection systems (Carter, 1981), and subsequently in mapping underground sources of seismic acoustic emissions (Norton and Won, 2000), PAM was proposed by Gyongy and Coussios (2010) to provide spatio-temporal monitoring of sources of acoustic emissions, and in particular cavitating bubbles, during HIFU therapy. More specifically, acoustic emissions originating from the focal region of the HIFU transducer are recorded passively during the course of the treatment using a multi-element array, and combined using beamforming techniques to provide estimations of source energy at different locations within a pre-defined area of interest. The key steps of this method are demonstrated in Fig. 1.1 and presented in further detail in this section.

In linear wave propagation theory in fluids, the momentum equation, which uses Newton's second law of motion to state that the net force on a control volume is equal to the acceleration times mass of the particles in the control volume, can provide an expression for the pressure field relative to the particle velocity in the medium. When viscous stresses are neglected, and only compressibility and inertia of the medium are considered, the linearized equation of momentum is expressed, assuming small perturbations of pressure and density around their ambient state, as (Lighthill, 2001):

$$\rho_0 \frac{\partial \boldsymbol{u}}{\partial t} = -\nabla p \tag{1.5}$$

where ρ_0 is the density of the medium, $\boldsymbol{u}$ the vector velocity field, and p the pressure field.

Considering that the velocity consists of a rotational and an irrotational part, and the rotational part, known as vorticity is independent of time in the linear regime, the velocity field is solely characterised by its irrotational part, defined as the gradient of a 'velocity potential' ϕ:

$$\boldsymbol{u} = \nabla \phi \tag{1.6}$$

From equations (1.5) and (1.6), an expression for the induced excess pressure and the velocity potential can be defined (Lighthill, 2001):

$$p - p_0 = -\rho_0 \frac{\partial \phi}{\partial t} \tag{1.7}$$

in the linear regime where the gradients of the two sides of (1.7) are equal everywhere in space, and in an undisturbed medium both sides equal to zero.

In order to describe a simple source, i.e. a source that radiates sound equally in all directions, the velocity potential spherically symmetrical about a point is expressed as $\phi = \phi(r, t)$, where r is the distance from the central point and *t* is the time variable. According to classical fluid dynamics theory, the velocity potential is related to the rate of volume outflow $m(t)$ from the centre of the simple source through the following equation:

$$\phi = -m(t)/4\pi r \tag{1.8}$$

Considering a sound wave that travelled distance r, with speed of sound c, the rate of volume outflow that travelled the same distance can be expressed as:

$$\phi = -m(t - r/c)/4\pi r \tag{1.9}$$

The derivative with respect to time of (1.9) is now:

$$\frac{\partial \phi}{\partial t} = -\dot{m}(t - r/c)/4\pi r \tag{1.10}$$

By defining for a simple source the rate of change of mass outflow as:

$$q = \rho_0 \dot{m}(t) \tag{1.11}$$

combination of equations (1.7), (1.10) and (1.11) provides a direct relationship between the rate of change of mass outflow from the source, also known as the source strength, and the resulting excess pressure (Lighthill, 2001):

$$p - p_0 = q(t - r/c)/4\pi r \tag{1.12}$$

For reasons of compatibility with notation presented later in this chapter, equation (1.12) is re-written here for a simple source at location $\boldsymbol{r}$ and source strength q, resulting in pressure p at location $\boldsymbol{r}'$ and time t:

$$p(\boldsymbol{r}', t) = \frac{q(\boldsymbol{r}, t - |\boldsymbol{r}' - \boldsymbol{r}|/c)}{4\pi|\boldsymbol{r}' - \boldsymbol{r}|} \tag{1.13}$$

The above relationship allows us to define the inverse problem of estimating the source strength using the pressure waves recorded by the sensors of an array. As already stated, the expression in (1.12) is only true in the linear regime, and does not account for attenuation. Since non-linear wave propagation is expected in the various applications of PAM, it could be evaluated using variations of the nonlinear wave equation that include higher than first order terms to account for nonlinear phenomena. The most commonly used equation is the Westervelt equation, and its simplification, the Burgers equation, which uses up to second order terms. An alternative is the KZK (Khokhlov-Zabolotskaya-Kuznetsov) equation that accounts for non-linearity, diffraction and absorption, but the main disadvantage of all the above equations is the high computational cost in order to acquire a numerical solution. For this reason, an assumption of sufficient representation of the pressure-source strength relationship for PAM using (1.13) has been made. The validity of this assumption is supported by previously reported numerical simulations and experimental results (Collin and Coussios, 2011). In this study, the authors demonstrated that the propagation of sound at a distance large enough compared to the source radius and small enough compared to the shock wave formation distance can be accurately modelled by neglecting the nonlinear effects. The underlying physical phenomena resulting in the above observation are a combination of increased attenuation at higher frequencies generated very close to the cavitating bubble, and spherical spreading that rapidly reduces the amplitude of the emissions a short distance from the source.

Following the steps described below, and using equation (1.13), the aim of passive acoustic mapping is to create maps of sources of acoustic activity by estimating

the source strength at different locations of interest, in the presence of interfering signals.

Step 1: Grid definition

Depending mainly on the size of the focus of the HIFU transducer, a two-dimensional area of interest is defined in front of the receiving array. This area is organised in voxels and for each voxel source strength or energy will be estimated. The choice of the size of each voxel in each direction (axial or transverse with respect to the array) is mostly governed by the resolution limits of PAM, which will be discussed later on.

Step 2: Recording of acoustic emissions

During an ultrasound treatment, acoustic emissions associated with both linear and nonlinear processes are generated, and propagate spherically outwards from the source location. A subset of these acoustic waveforms impinges on the array, and it is recorded by all elements of the array. The signals available from the electronics of the data acquisition system are voltage traces, and to be used for source energy estimation, a conversion from voltage to pressure units is required at this stage. For this purpose, calibration of the receiving array over a range of frequencies, which cover the effective receive bandwidth of the array, is used.

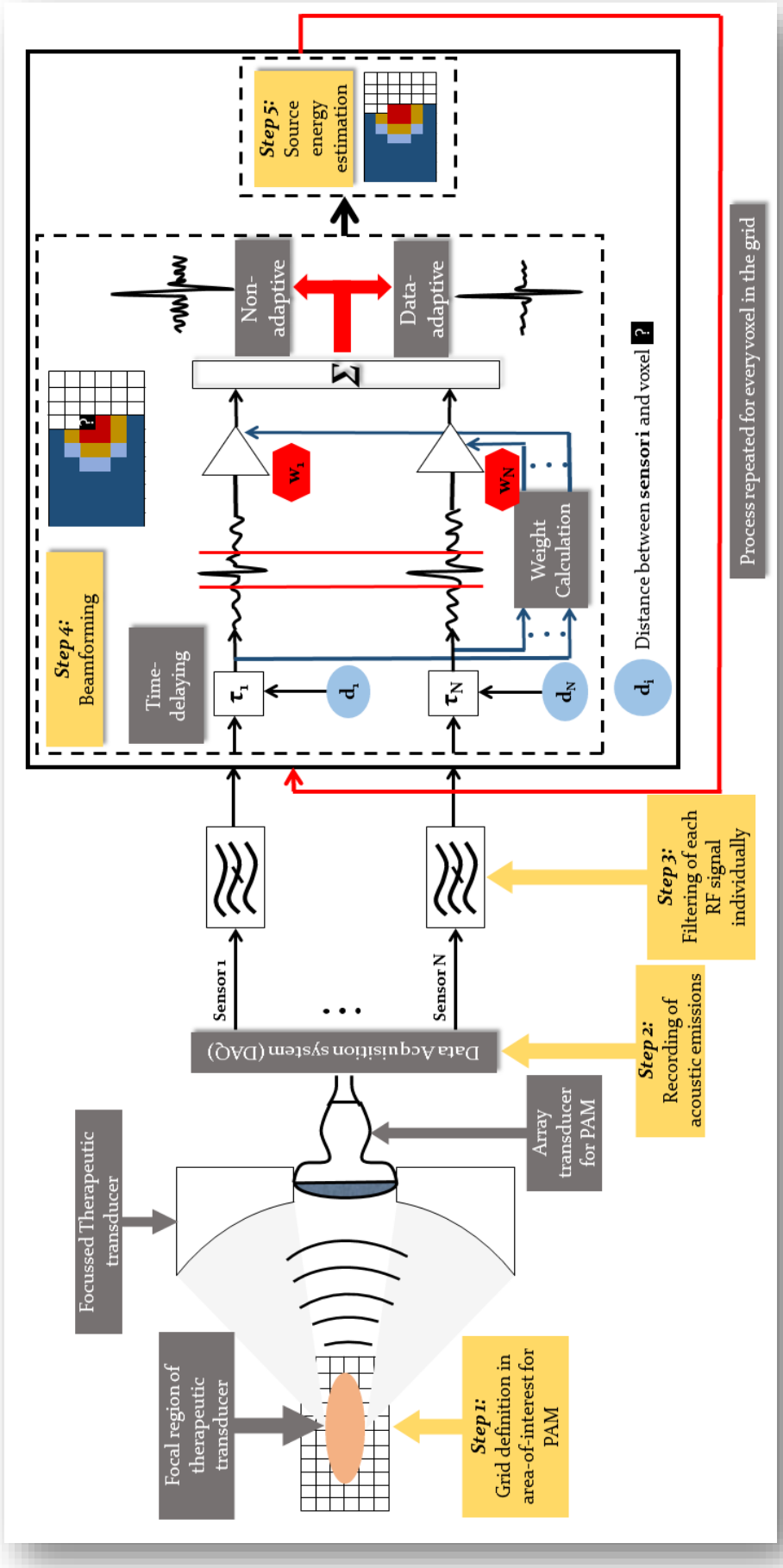


Figure 1.1 Schematic of the steps included in the PAM algorithm, from the recording of the pressure signals until the generation of PAM maps.

Step 3: Filtering of the recorded signals

As already briefly discussed, clinically available therapeutic transducers and monitoring arrays, when combined in a setup, may be characterised by overlapping bandwidths. This implies that during treatment, acoustic emissions due to a variety of physical phenomena are simultaneously recorded by the elements of the array. A characteristic example would be the recording of harmonics of the driving frequency due to scattering from interfering structures, along with broadband emissions due to inertial cavitation. Depending on the application, a different subset of these acoustic emissions is of interest, and in some cases this subset has a distinct signature in the frequency domain compared to the unwanted interfering signals. Therefore, filtering of each waveform individually is performed to isolate the signal of interest prior to further processing.

The steps that follow are repeated for all voxels in the defined grid individually to calculate the source energy that corresponds to each voxel.

Step 4: Beamforming

The concept of beamforming involves the use of a spatial aperture for signal recording, and the implementation of a spatial filter for separation (in space) of sources and interfering signals (Van Veen and Buckley, 1988). Considering equation (1.13), in the presence of multiple sources in the field of interest, estimation of the source strength at position $\boldsymbol{r}$ could be achieved by back-propagating the signals received by the array to the location of interest and coherently summing them for noise and interference rejection (Gyöngy and Coussios, 2010):

$$\tilde{q}(\boldsymbol{r},t) = \frac{1}{N}\sum_{i=1}^{N} 4\pi|\boldsymbol{r_i} - \boldsymbol{r}|\,\tilde{p}(\boldsymbol{r_i}, t + |\boldsymbol{r_i} - \boldsymbol{r}|/c) \tag{1.14}$$

where i is the index of the element on the array, $\boldsymbol{r_i}$ the location of the ith element of the array, $\tilde{p}$ the pressure recorded on each element of the array, and c the speed of sound in the medium.

As demonstrated in Fig. 1.1 and in equation (1.14), beamforming requires the knowledge of the coordinates of the elements of the array and the speed of sound in the propagation medium. This way, depending on the location of the voxel of interest with respect to the array, the time traces recorded are time-delayed/shifted in time according to the propagation distance between the voxel and the corresponding element. This process essentially enables alignment in time of the emissions originating from the voxel of interest on all elements of the array, as if all the elements where located at the same distance away from this voxel. At the same time, the averaging process described in equation (1.14) allows noise reduction and suppression of interfering signals due to sources located elsewhere.

Another important feature of beamforming is the calculation and application of weights, w_i, to all time-delayed signals, a process known as apodization, which, depending on the choice of beamforming algorithm, might be the same for all elements of the array, or it could be data-adaptive and calculated through an optimization process. Therefore, equation (1.14) is modified as follows:

$$\tilde{q}(\boldsymbol{r},t) = \frac{1}{N}\sum_{i=1}^{N} w_i 4\pi|\boldsymbol{r_i} - \boldsymbol{r}|\,\tilde{p}(\boldsymbol{r_i}, t + |\boldsymbol{r_i} - \boldsymbol{r}|/c) \tag{1.15}$$

Application of different weights on each element enables improved interference rejection, and therefore, better spatial resolution. Different beamforming algorithms have been proposed in the context of PAM and they will be discussed in detail later on.

Step 5: Source energy estimation

From the estimation of the source strength distribution, other quantities potentially more useful could be extracted, such as source power and source energy. Source power can be calculated via acoustic intensity which is defined for plane waves as follows, and combined with equation (1.13) it is directly related to source strength:

$$I(\boldsymbol{r},t)=\frac{p^2(\boldsymbol{r},t)}{\rho_0 c}=\frac{q^2(\boldsymbol{r}',t-|\boldsymbol{r}-\boldsymbol{r}'|/c)}{(4\pi|\boldsymbol{r}-\boldsymbol{r}'|)^2\rho_0 c} \tag{1.16}$$

where ρ_0 and c are the density and speed of sound of the medium respectively.

The assumption of plane waves is only valid when the source is in the far field of the detector. Source power defined as the acoustic intensity crossing a spherical surface at time *t* is then:

$$P(\boldsymbol{r},t)=4\pi|\boldsymbol{r}-\boldsymbol{r}'|^2 I(\boldsymbol{r},t)=\frac{q^2(\boldsymbol{r}',t-|\boldsymbol{r}-\boldsymbol{r}'|/c)}{4\pi\rho_0 c} \tag{1.17}$$

Finally, integration of power over time $[t_0, t_0+T]$ provides us with source energy:

$$\Psi(\boldsymbol{r})=\int_{t_0}^{t_0+T}P(\boldsymbol{r},t)=\int_{t_0}^{t_0+T}\frac{q^2(\boldsymbol{r}',t-|\boldsymbol{r}-\boldsymbol{r}'|/c)}{4\pi\rho_0 c}\,dt \tag{1.18}$$

Therefore, in the context of PAM, source energy maps can be obtained by combining equations (1.14) and (1.18):

$$\Psi(\boldsymbol{r}) = \int_{t_0}^{t_0+T} \frac{\tilde{q}^2(\boldsymbol{r}', t - |\boldsymbol{r} - \boldsymbol{r}'|/c)}{4\pi\rho_0 c} dt \tag{1.19}$$

where $\tilde{q}$ is the source energy estimate.

Spatial resolution of Passive Acoustic Mapping

Assuming a point source placed in front of a finite element linear array, the spatial resolution of the passive acoustic mapping method can be determined by determining the point spread function (PSF) of the imaging system. The PSF is a measure of the diffraction limits of the system, and in two dimensions, the PSF describes the blurring occurring during mapping of the simple source in each dimension, transverse and axial, with respect to the array.

In the context of PAM, an expression for the theoretical PSF has been derived in (Gyöngy, 2010; Gyöngy and Coussios, 2010) for a broadband source placed in the near filed of a linear array of discrete receivers in both the transverse and axial direction assuming uniform weighting of the elements on the array and exploiting the Fresnel approximation (Mast, 2007). A useful quantity is also introduced, the -3dB width of the PSF, which essentially represents the minimum distance required between two point sources in order for them to be distinguished in an image.

Transverse Resolution $\Delta x_{-3dB} \approx 0.89 f_{\#} \lambda$ (1.20)

Axial Resolution $\Delta z_{-3dB} \approx 6.95 f_{\#}^2 \lambda$ (1.21)

where $f_{\#} = z/D$ with z representing the axial distance between the source and the array, D the aperture of the linear array, and λ the wavelength corresponding to the centre frequency of the linear array.

1.4.2 BEAMFORMING TECHNIQUES FOR PASSIVE ACOUSTIC MAPPING

Beamforming algorithms are categorised into non-adaptive or data-adaptive algorithms depending on the way the weights that are applied to the signals of the receiving elements are calculated (equation (1.15)). The choice of a beamforming algorithm depends on the requirements of the system, and most of the times a compromise needs to be made related to improved spatial resolution and source energy estimation, versus computational cost and algorithmic complexity.

In this section, the two existing beamforming algorithms implemented in the context of PAM, Time Exposure Acoustics and Robust Capon Beamformer, are presented and discussed in detail.

1.4.2.1 TIME EXPOSURE ACOUSTICS (TEA)

TEA was originally introduced by (Norton and Won, 2000) as a passive imaging method of underground scatterers illuminated by ambient seismic noise. This method provides a source intensity map (arbitrary units), and the intensity of each pixel/location, $\bar{O}$, is calculated according to the following equation:

$$\overline{O}(\boldsymbol{r}) = E\left\{\left|\sum_{i=1}^{N} \hat{u}_n(\boldsymbol{r})\right|^2\right\} - E\left\{\sum_{i=1}^{N} |\hat{u}_n(\boldsymbol{r})|^2\right\} \tag{1.22}$$

where $E\{\cdot\}$ denotes the statistical expectation operator, and $\hat{u}_n(\boldsymbol{r})$ is defined as:

$$\hat{u}_n(\boldsymbol{r}) = 4\pi|r - \boldsymbol{r}_n|\hat{u}(\boldsymbol{r}_n, |r - \boldsymbol{r}_n|/c) \tag{1.23}$$

$\hat{u}(\boldsymbol{r}_n, t)$ being the signal recorded by the sensor *n* positioned at $\boldsymbol{r}_n$ after being filtered.

In the context of PAM, equation (1.22) can be written as (Gyongy et al., 2008; Gyongy and Coussios, 2010):

$$I(\boldsymbol{r}) = \frac{1}{T}\int_{t_0}^{t_0+T}\left[\left(\sum_i H_i(\boldsymbol{r}, t)\right)^2 - \sum_i H_i(\boldsymbol{r}, t)^2\right]dt \tag{1.24}$$

where $H_i(\boldsymbol{r}, t)$ is the back-propagated signal:

$$H_i(\boldsymbol{r}, t) = a(d_i(\boldsymbol{r}))p_i(t + d_i(\boldsymbol{r})/c) \tag{1.25}$$

with $d_i(\boldsymbol{r})$ denoting the distance between the i^{th} element of the array and location $\boldsymbol{r}$ in the grid, $p_i(t)$ the pressure signal detected by the i^{th} element of the array, and $a(d_i(\boldsymbol{r}))$ a receiver spatial sensitivity term.

Exploiting the identity:

$$\left(\sum_i a_i\right)^2 - \sum_i {a_i}^2 = 2\sum_{i<j} a_i a_j \tag{1.26}$$

and re-arranging the summation and integration, the above equation becomes (Gyongy et al., 2008):

$$I(\boldsymbol{r}) = \sum_{i<j} \left[\frac{2}{T} \int_{t_0}^{t_0+T} H_i(\boldsymbol{r}, t) H_j(\boldsymbol{r}, t) dt \right] \tag{1.27}$$

This equation indicates that the intensity map created by PAM-TEA also corresponds to the summation of all cross-correlations of the time-delayed and amplitude compensated signals. However, (1.27) is more computationally expensive compared to (1.24), and this is the rationale behind the choice of equation (1.24) by Gyongy and Coussios (2010). Moreover, the second term in (1.24) aims at removing a DC bias from the image intensity by subtracting the variance of the received signals. However, this term is typically omitted (Gyöngy, 2010; Gyongy and Coussios, 2010) as it lowers the intensity estimated at the source locations. Therefore, the intensity map expression for PAM using TEA is reduced to the following equation:

$$I(\boldsymbol{r}) = \frac{1}{T} \int_{t_0}^{t_0+T} \left(\sum_i H_i(\boldsymbol{r}, t) \right)^2 dt \tag{1.28}$$

which in Cartesian coordinates for a three-element vector $\boldsymbol{x} = [x, y, z]^T$ is:

$$I(\boldsymbol{x}) = \frac{1}{T} \int_{t_0}^{t_0+T} \left(\sum_i H_i(\boldsymbol{x}, t) \right)^2 dt \tag{1.29}$$

It can be observed that this equation is directly proportional to equation (1.19) in Cartesian coordinates that provides an energy map (Coviello et al., 2015):

$$\Psi(\boldsymbol{x}) = \int_{t_0}^{t_0+T} \frac{\tilde{q}^2(\boldsymbol{x}, t)}{4\pi\rho_0 c}\, dt \tag{1.30}$$

where

$$\tilde{q}(\boldsymbol{x}, t) = \sum_{i=1}^{N} w_i 4\pi d_i(\boldsymbol{x})\, \tilde{p}_i(t + d_i(\boldsymbol{x})/c) \tag{1.31}$$

and the distance between a voxel at $[x, y, z]^T$ and a sensor i at $[x_i, y_i, z_i]^T$ is:

$$d_i(\boldsymbol{x}) = \sqrt{(x - x_i)^2 + (y - y_i)^2 + (z - z_i)^2} \tag{1.32}$$

The weights w_i are pre-defined and equal for all elements of the array to $1/N$, where N is the number of sensors, and it is, therefore, apparent that TEA is effectively a non-adaptive beamformer. The lack of data-adaptive apodization results in imaging artifacts related to inaccuracies in the coordinates of the array elements, imperfections of the array elements, such as varying receive sensitivity, and multi-bubbles interference. Specifically, the presence of multiple bubbles interacting with each other in the region of interest, along with decreasing axial resolution as we move away axially from the array has been found to result in a post-focus "tail-artifact" that falsely indicates activity beyond the actual source (Coviello et al., 2015).

1.4.2.2 DATA-ADAPTIVE BEAMFORMERS

The limitations in spatial accuracy introduced by the TEA algorithm naturally led to investigation of optimal beamformers, as an approach to improve the spatial resolution of PAM and remove artifacts, and, as a consequence, attempt to enhance the reliability of PAM in more challenging scenarios where array imperfections exist and multiple-bubble interferences occur. The two optimal beamforming algorithms proposed by Coviello et al. (2015) in the context of PAM that attempt to address the above challenges, are Capon Beamformer (Capon, 1969) and Robust Capon Beamformer (Li et al., 2003; Stoica et al., 2003), and they are presented here. For better comparison among all beamforming algorithms the key equations are transformed in matrix format, as suggested in (Coviello et al., 2015), and they are summarised in the following table:

Table 1.1 PAM algorithm key equations transformed into matrix format

$\boldsymbol{d_i(x) = \sqrt{(x - x_i)^2 + (y - y_i)^2 + (z - z_i)^2}}$	$\boldsymbol{D(x) = diag[d_i(x), \dots, d_N(x)]}$
$\boldsymbol{\tilde{p}_i(t + d_i(x)/c)}$	$\boldsymbol{p(x,t) = \begin{bmatrix} \tilde{p}_1(t + d_1(x)/c) \\ \vdots \\ \tilde{p}_N(t + d_N(x)/c) \end{bmatrix}}$ $\boldsymbol{R_p(x) = \int_{t_0}^{t_0+T} p(x,t)p(x,t)^T dt}$
$\boldsymbol{\tilde{q}(x,t) = \sum_{i=1}^{N} w_i 4\pi d_i(x) \tilde{p}_i(t + d_i(x)/c)}$	$\tilde{q}(x,t) = 4\pi w^T D(x) p(x,t)$
$\boldsymbol{\Psi(x) = \int_{t_0}^{t_0+T} \frac{\tilde{q}^2(x,t)}{4\pi\rho_0 c} dt}$	$\Psi(x) = \frac{4\pi}{\rho_0 c} w^T D(x) R_p(x) D(x) w$

Capon Beamformer (CB)

The Capon Beamformer, or Minimum Variance Distortionless Response (MVDR) Beamformer was introduced by Capon (1969), and seeks to adapt the weights $\boldsymbol{w}$ by minimising the variance of the array output subject to a linear constraint that allows the signal-of-interest to remain undisturbed. The optimisation problem can be, therefore, described by the following expression for pre-steered and amplitude-compensated signals $\boldsymbol{D}(\boldsymbol{x})\boldsymbol{p}(\boldsymbol{x},t)$, and steering vector corresponding to the direction-of-arrival (DOA) of the signal-of-interest to be equal to the unity vector ($\boldsymbol{a}_0 = \boldsymbol{1}$) due to pre-steering:

$$\min_{w} \boldsymbol{w}^T \boldsymbol{D}(\boldsymbol{x}) \boldsymbol{R}_p(\boldsymbol{x}) \boldsymbol{D}(\boldsymbol{x}) \boldsymbol{w} \quad \text{subject to } \boldsymbol{w}^T \boldsymbol{a}_0 = 1 \tag{1.33}$$

where $\boldsymbol{R}_p$ represents the covariance matrix of the time-delayed recorded signals.

At this point it is important to take a step back and discuss the rationale behind the formulation of the above optimisation problem. Assuming the array output at any point in time is:

$$r(t) = s(t)a_0 + \sum_i s_i(t)\, a_i + v(t) \tag{1.34}$$

where $s(t)$ is the signal-of-interest arriving from DOA a_0, $s_i(t)$ is the ith interfering signal arriving from DOA a_i, and $v(t)$ is the noise of the system.

The output of the beamformer is

$$y(t) = \boldsymbol{w}^T r(t) \tag{1.35}$$

and the goal is to choose the weights so that the desired signal $s(t)$ is preserved and the interfering signals and noise are suppressed. One performance measure of a beamformer that has also been used in the case of CB is the output signal-to-interference-plus-noise ratio (SINR):

$$SINR = \frac{E\{|\boldsymbol{w}^T s(t)a_0|^2\}}{E\{|\boldsymbol{w}^T(\sum s_i(t)a_i + v(t))|^2\}} = \frac{\sigma_s^2|\boldsymbol{w}^T a_0|^2}{E\{|\boldsymbol{w}^T(\sum s_i(t)a_i + v(t))|^2\}} = \frac{\sigma_s^2|\boldsymbol{w}^T a_0|^2}{\boldsymbol{w}^T \boldsymbol{R_{i+v}} \boldsymbol{w}} \quad (1.36)$$

where $\sigma_s^2 = E\{|s(t)|^2\}$ is the power of the signal-of-interest, and $\boldsymbol{R_{i+v}} = \int_{t_0}^{t_0+T}(\sum s_i(t)a_i + v(t))(\sum s_i(t)a_i + v(t))^{\boldsymbol{T}} dt$ is the covariance matrix of the interfering signals plus noise vector.

The goal of the beamformer is now to maximise the SINR while preserving the signal-of-interest, i.e. $\boldsymbol{w}^T a_0 = 1$, and to achieve this, the denominator needs to be minimised. However, minimisation of the variance of the array output with respect to the interferences and noise is not possible, since these signals and their origin are unknowns of the problem. Instead, minimisation of the variance of the output of the beamformer is proposed, which is equivalent, since:

$$\min_w E\{|y(t)|^{\boldsymbol{2}}\} = \min_w \boldsymbol{w}^T \boldsymbol{R} \boldsymbol{w} = \min_w(\sigma_s^2|\boldsymbol{w}^T a_0|^2 + \boldsymbol{w}^T \boldsymbol{R_{i+v}} \boldsymbol{w}) = \min_w(\boldsymbol{w}^T \boldsymbol{R_{i+v}} \boldsymbol{w}) \quad (1.37)$$

where $\boldsymbol{R} = \int_{t_0}^{t_0+T} \boldsymbol{r}(t)\boldsymbol{r}(t)^{\boldsymbol{T}} dt$ is the covariance matrix of the array output vector.

Returning to the description of the CB, the solution to this constrained optimisation problem is found analytically using the method of Lagrange multipliers (Coviello et al., 2015):

$$w_{CB} = \frac{\boldsymbol{D}(\boldsymbol{x})^{-1}\boldsymbol{R}_p(\boldsymbol{x})^{-1}\boldsymbol{D}(\boldsymbol{x})^{-1}\boldsymbol{a}_0}{\boldsymbol{a}_0{}^T\boldsymbol{D}(\boldsymbol{x})^{-1}\boldsymbol{R}_p(\boldsymbol{x})^{-1}\boldsymbol{D}(\boldsymbol{x})^{-1}\boldsymbol{a}_0} \tag{1.38}$$

The PAM energy map based on CB is calculated accordingly:

$$\Psi(\boldsymbol{x}) = \frac{4\pi}{\rho_0 c}\frac{1}{\boldsymbol{a}_0{}^T\boldsymbol{D}(\boldsymbol{x})^{-1}\boldsymbol{R}_p(\boldsymbol{x})^{-1}\boldsymbol{D}(\boldsymbol{x})^{-1}\boldsymbol{a}_0} \tag{1.39}$$

Due to the data-adaptive calculation of the weights, the spatial resolution of PAM has been significantly improved, allowing better localisation of sources of acoustic activity (Coviello et al., 2015). However, it is clear from (1.39) that, in order to achieve optimised calculation of w_{CB}, the nominal steering vector $\boldsymbol{a}_0$ must be accurately estimated. However, in the case of CB, it is fixed to unity, and even small array sensitivity issues, and errors in the input coordinates of the array elements might cause divergence of the actual steering vector from $\boldsymbol{a}_0$. It has already been shown that such misalignment leads to significant degradation of the PAM-CB performance, that in some cases is even worse than the non-adaptive beamformer, TEA (Coviello et al., 2015).

Robust Capon Beamformer (RCB)

Under clinical and experimental conditions, it is expected that array variabilities exist related to sensors' relative positions and gain, or varying speed of wave propagation in inhomogeneous media. Therefore, the adoption of a beamforming technique for PAM that will be flexible to such conditions is necessary to ensure optimised performance of PAM. A natural extension of CB has been proposed, the

Robust Capon Beamformer, that re-formulates the problem allowing the steering vector to vary within an ellipsoidal region, and therefore, compensates for the array imperfections (Li et al., 2003; Stoica et al., 2003).

Assuming a nominal steering vector $\bar{\boldsymbol{a}} = \mathbf{1}$, estimation of the actual steering vector $\boldsymbol{a}$ is now the goal of the optimization problem, which is formulated as:

$$\min_{a} \boldsymbol{a}^T \left(\boldsymbol{D}(\boldsymbol{x}) \boldsymbol{R}_p(\boldsymbol{x}) \boldsymbol{D}(\boldsymbol{x}) \right)^{-1} \boldsymbol{a} \quad \text{subject to } \|\boldsymbol{a} - \bar{\boldsymbol{a}}\|^2 \leq \varepsilon \tag{1.40}$$

The constraint imposed accounts for the region of uncertainty, in which $\boldsymbol{a}$ can vary, and ε is the parameter of uncertainty that allows the region to expand or shrink. The choice of the right value for ε depends primarily on the experimental conditions, and it will involve a compromise between tolerance to steering vector mismatches and interference suppression capability (Coviello et al., 2015).

Using again the Lagrange multiplier methodology, the optimal solution for the steering vector of the signal-of-interest is (Li et al., 2003):

$$\hat{\boldsymbol{a}}_0 = \bar{\boldsymbol{a}} - \boldsymbol{U}(\boldsymbol{I} + \lambda \boldsymbol{\Gamma})^{-1} \boldsymbol{U}^* \bar{\boldsymbol{a}} \tag{1.41}$$

where the columns of $\boldsymbol{U}$ contain the eigenvectors of $\boldsymbol{D}(\boldsymbol{x}) \boldsymbol{R}_p(\boldsymbol{x}) \boldsymbol{D}(\boldsymbol{x})$, the diagonal elements of $\boldsymbol{\Gamma}$ are the corresponding eigenvalues, and λ is the calculated Lagrange multiplier. The energy of the signal-of-interest, and consequently, the RCB-PAM energy map is calculated, after normalisation and units conversion, according to the following equation (Coviello et al., 2015; Li et al., 2003):

$$\Psi(\boldsymbol{x}) = \frac{4\pi}{\rho_0 c}\frac{\|\hat{\boldsymbol{a}}_0\|^2}{N}\frac{1}{\bar{\boldsymbol{a}}\boldsymbol{U}\boldsymbol{\Gamma}(\lambda^{-2}\boldsymbol{I} + 2\lambda^{-1}\boldsymbol{\Gamma} + \boldsymbol{\Gamma}^{\boldsymbol{2}})^{-1}\boldsymbol{U}^{*}\bar{\boldsymbol{a}}} \tag{1.42}$$

The performance of RCB-PAM has been evaluated under *in vitro* and *in vivo* experimental conditions, and it has been shown that the localisation of the recorded acoustic activity has been significantly improved. It is, however, important to mention that optimal beamforming using RCB suffers from increased computational cost compared to TEA. The continuous development of hardware and software, though, allows real-time implementation of RCB-PAM method based on Graphics Processing Units (GPUs) or a cluster of GPUs-CPUs, increasing significantly its temporal resolution. More importantly, RCB assumes that the recorded by the elements of the array signals follow a Gaussian distribution, since the weights are calculated via the minimisation of the variance of the array output. However, it is expected that biomedical signals, and more specifically, cavitation emissions might also contain important information on higher- than the second-order statistics (Chua et al., 2010). Such an assumption is, therefore, expected to compromise the weight calculation, and subsequently the spatial resolution and accuracy of the generated PAM maps. Therefore, further improvement of the spatial resolution is desirable especially in drug delivery applications, in which the targeting depth might be big and the areas to be mapped and distinguished small and close to each other, creating, as a consequence, a challenging situation for PAM.

1.5 PROJECT AIMS AND OBJECTIVES

Passive Acoustic Mapping (PAM) is already finding a wide variety of applications and has great potential as a real-time monitoring technique of cavitation activity for ultrasound therapies, both thermal and non-thermal. As an ultrasound-based modality, it is cost-effective and suffers from the same distortions and limitations as the therapeutic ultrasound is intended to monitor. Moreover, due to its passive nature, there is no need for interlacing treatment and monitoring, providing truly real-time functional estimates of acoustic sources during therapy. It is therefore both a direct competitor and complimentary to already clinically approved monitoring techniques, such as MRI thermometry and active ultrasound imaging, which are not capable of monitoring and classifying cavitation activity during treatment.

Real-time monitoring using PAM of the progress of the treatment through reliable distinction of acoustic emissions of interest and accurate localisation of the sources of these acoustic emissions is crucial for all the ultrasound-based treatments to ensure safety. Fig. 1.2 is a characteristic example of the misleading spatial information offered by PAM, when either TEA or RCB is used as a beamforming algorithm. An agar phantom with a central channel has been used in this *in vitro* experiment, and a solution of the contrast agent Sonovue (Schneider, 1999) is flowing through the channel. A 0.5MHz HIFU transducer is focused on the channel, causing cavitation inside the channel. However, as it is observed from the PAM maps, activity is mapped well outside the physical boundaries of the channel, outlined on the B-mode image, which is overlaid with the PAM maps. Additionally, activity is also mapped on the boundary between the phantom and the water bath, where no cavitation is expected to occur. This misleading activity is potentially caused by reflections of the incident wave

by the agar-water interface. These reflections are characterised by harmonics of the fundamental frequency that have probably not been efficiently removed with the use of a comb filter.

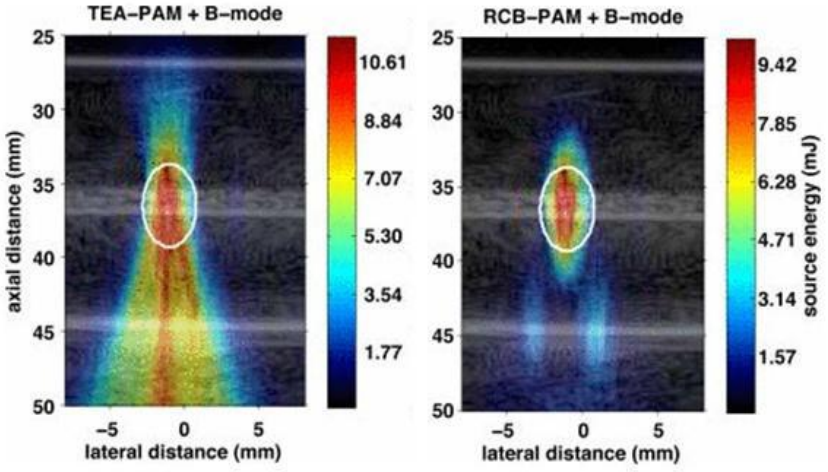


Figure 1.2 PAM maps using TEA (left) and RCB (right) beamforming algorithm overlaid with B-mode, indicating cavitation activity due to Sonovue contrast agent flowing through a channel formed in an agar gel (Coviello et al., 2015).

As demonstrated from the above example, PAM still requires significant improvements in its spatial accuracy and its ability to suppress interfering signals. The overall aim of the work carried out as part of this doctoral thesis aims at addressing the above shortcomings, which presently hinder clinical adoption of PAM. Specific objectives are highlighted here:

1. Improvement in the spatial resolution of PAM and its artefact rejection ability is expected to be achieved via the adoption of *optimal data-adaptive beamforming algorithms*. The currently available beamforming algorithm aims at minimizing the variance of the array output, assuming, therefore, that the key information about acoustic activity is hidden in the second order statistics of the signal. Adoption of an alternative beamforming algorithm for PAM that would better exploit the statistics of

the received signal, i.e. take into account the higher order statistics rather than just the variance of the signal output of the array is investigated.

2. *Accurate separation of the signal-of-interest from interfering signals* in the recorded by the elements of the array emissions prior to beamforming is also essential for improved spatial resolution. Depending on the application, the signal-of-interest could have different frequency signatures, narrowband or broadband, and the aim is to isolate one component from the other. A characteristic example, encountered in treatments where the key mechanism is inertial cavitation, is the isolation of broadband emissions due to inertial cavitation from strong narrowband signals due to reflections from structures such as bones. Over the course of the treatment the relative magnitude of the signal-of-interest with respect to the interferences might vary significantly. Filtering of the received signal in PAM is typically achieved using non-adaptive pre-defined comb filters with limited performance due to their fixed response. Therefore, the performance of a data-adaptive filtering technique in classifying and quantifying broadband and narrowband components of the received signal is evaluated in comparison to non-adaptive comb filtering.

3. Evaluation of the improvements in source detectability and spatial resolution afforded by combining the proposed improved beamforming and signal filtration methods, relative to currently available techniques, namely RCB combined with comb filtering.

1.6 THESIS OUTLINE

In Chapter 2 a new beamforming approach for PAM based on higher-order-statistics is proposed, and the numerical simulations and *in vitro* experimental results for the performance validation of the method are presented. In Chapter 3, a data-adaptive model for accurate signal-of-interest separation among interferences is introduced. Both simulations and *in vitro* experimentation are performed to assess the performance of the proposed filtration method. In Chapter 4 the proposed beamforming and filtering methods are applied in cavitation mapping following vascular extravasation and the improvement in PAM spatial resolution is examined. Finally, an overall summary of the work presented in this thesis together with suggestions for future work are presented in Chapter 5.

1.7 REFERENCES

Alexandrov, A.V., Mikulik, R., Ribo, M., Sharma, V.K., Lao, A.Y., Tsivgoulis, G., Sugg, R.M., Barreto, A., Sierzenski, P., Malkoff, M.D., Grotta, J.C., 2008. A pilot randomized clinical safety study of sonothrombolysis augmentation with ultrasound-activated perflutren-lipid microspheres for acute ischemic stroke. Stroke J. Cereb. Circ. 39, 1464–1469.

Apfel, R.E., 1981. Acoustic cavitation prediction. J. Acoust. Soc. Am. 69, 1624–1633.

Apfel, R.E., 1970. The Role of Impurities in Cavitation-Threshold Determination. J. Acoust. Soc. Am. 48, 1179–1186.

Arnal, B., Pernot, M., Tanter, M., 2011. Monitoring of thermal therapy based on shear modulus changes: I. shear wave thermometry. IEEE Trans. Ultrason. Ferroelectr. Freq. Control 58, 369–378.

Arvanitis, C.D., Livingstone, M.S., McDannold, N., 2013. Combined Ultrasound and MR Imaging to Guide Focused Ultrasound Therapies in the Brain. Phys. Med. Biol. 58, 4749–4761.

Atchley, A.A., Frizzell, L.A., Apfel, R.E., Holland, C.K., Madanshetty, S., Roy, R.A., 1988. Thresholds for cavitation produced in water by pulsed ultrasound. Ultrasonics 26, 280–285.

Atchley, A.A., Prosperetti, A., 1989. The crevice model of bubble nucleation. J. Acoust. Soc. Am. 86, 1065–1084.

Averkiou, M.A., 2001. Tissue harmonic ultrasonic imaging. Comptes Rendus Académie Sci. - Ser. IV - Phys. 2, 1139–1151.

Bacon, D.R., Carstensen, E.L., 1990. Increased heating by diagnostic ultrasound due to nonlinear propagation. J. Acoust. Soc. Am. 88, 26–34.

Bamber, J.C., Hill, C.R., 1979. Ultrasonic attenuation and propagation speed in mammalian tissues as a function of temperature. Ultrasound Med. Biol. 5, 149–157.

Bercoff, J., Pernot, M., Tanter, M., Fink, M., 2004. Monitoring Thermally-Induced Lesions with Supersonic Shear Imaging. Ultrason. Imaging 26, 71–84.

Bhatnagar, S., Schiffter, H., Coussios, C.-C., 2014. Exploitation of Acoustic Cavitation-Induced Microstreaming to Enhance Molecular Transport. J. Pharm. Sci. 103, 1903–1912.

Brennen, C.E., 1995. Cavitation and Bubble Dynamics. Oxford University Press.

Burns, P.N., 1996. Harmonic imaging with ultrasound contrast agents. Clin. Radiol. 51 Suppl 1, 50–55.

Capon, J., 1969. High-resolution frequency-wavenumber spectrum analysis. Proc. IEEE 57, 1408–1418.

Carlisle, R., Choi, J., Bazan-Peregrino, M., Laga, R., Subr, V., Kostka, L., Ulbrich, K., Coussios, C.-C., Seymour, L.W., 2013. Enhanced tumor uptake and penetration of virotherapy using polymer stealthing and focused ultrasound. J. Natl. Cancer Inst. 105, 1701–1710.

Carter, G., 1981. Time delay estimation for passive sonar signal processing. IEEE Trans. Acoust. Speech Signal Process. 29, 463–470.

Chan, V., Perlas, A., 2011. Basics of Ultrasound Imaging, in: Narouze, S.N. (Ed.), Atlas of Ultrasound-Guided Procedures in Interventional Pain Management. Springer New York, New York, NY, pp. 13–19.

Chapelon, J.Y., Margonari, J., Theillère, Y., Gorry, F., Vernier, F., Blanc, E., Gelet, A., 1992. Effects of high-energy focused ultrasound on kidney tissue in the rat and the dog. Eur. Urol. 22, 147–152.

Choi, J.J., Carlisle, R.C., Coviello, C., Seymour, L., Coussios, C.-C., 2014. Non-invasive and real-time passive acoustic mapping of ultrasound-mediated drug delivery. Phys. Med. Biol. 59, 4861.

Choi, J.J., Coussios, C.-C., 2012. Spatiotemporal evolution of cavitation dynamics exhibited by flowing microbubbles during ultrasound exposure. J. Acoust. Soc. Am. 132, 3538–3549.

Chua, K.C., Chandran, V., Acharya, U.R., Lim, C.M., 2010. Application of higher order statistics/spectra in biomedical signals--a review. Med. Eng. Phys. 32, 679–689.

Chung, A.H., Jolesz, F.A., Hynynen, K., 1999. Thermal dosimetry of a focused ultrasound beam in vivo by magnetic resonance imaging. Med. Phys. 26, 2017–2026.

Clarke, R.L., ter Haar, G.R., 1997. Temperature rise recorded during lesion formation by high-intensity focused ultrasound. Ultrasound Med. Biol. 23, 299–306.

Coleman, A.J., Saunders, J.E., 1993. A review of the physical properties and biological effects of the high amplitude acoustic fields used in extracorporeal lithotripsy. Ultrasonics 31, 75–89.

Collin, J.R.T., Coussios, C.C., 2011. Quantitative observations of cavitation activity in a viscoelastic medium. J. Acoust. Soc. Am. 130, 3289–3296.

Couture, O., Bannouf, S., Montaldo, G., Aubry, J.-F., Fink, M., Tanter, M., 2009. Ultrafast Imaging of Ultrasound Contrast Agents. Ultrasound Med. Biol. 35, 1908–1916.

Coviello, C., Kozick, R., Choi, J., Gyöngy, M., Jensen, C., Smith, P.P., Coussios, C.-C., 2015. Passive acoustic mapping utilizing optimal beamforming in ultrasound therapy monitoring. J. Acoust. Soc. Am. 137, 2573–2585.

Damianou, C.A., Sanghvi, N.T., Fry, F.J., Maass-Moreno, R., 1997. Dependence of ultrasonic attenuation and absorption in dog soft tissues on temperature and thermal dose. J. Acoust. Soc. Am. 102, 628–634.

Datta, S., Coussios, C.-C., McAdory, L.E., Tan, J., Porter, T., De Courten-Myers, G., Holland, C.K., 2006. CORRELATION OF CAVITATION WITH ULTRASOUND ENHANCEMENT OF THROMBOLYSIS. Ultrasound Med. Biol. 32, 1257–1267.

Eckersley, R.J., Chin, C.T., Burns, P.N., 2005. Optimising phase and amplitude modulation schemes for imaging microbubble contrast agents at low acoustic power. Ultrasound Med. Biol. 31, 213–219.

Eller, A., 1968. Force on a Bubble in a Standing Acoustic Wave. J. Acoust. Soc. Am. 43, 170–171.

Fahey, B.J., Nightingale, K.R., Stutz, D.L., Trahey, G.E., 2004. Acoustic radiation force impulse imaging of thermally- and chemically-induced lesions in soft tissues: preliminary ex vivo results. Ultrasound Med. Biol. 30, 321–328.

Farny, C.H., Holt, R.G., Roy, R.A., 2010. The Correlation Between Bubble-Enhanced HIFU Heating and Cavitation Power. IEEE Trans. Biomed. Eng. 57, 175–184.

Farny, C.H., Holt, R.G., Roy, R.A., 2009. Temporal and Spatial Detection of HIFU-Induced Inertial and Hot-Vapor Cavitation with a Diagnostic Ultrasound System. Ultrasound Med. Biol. 35, 603–615.

Flynn, H.G., 1975. Cavitation dynamics: II. Free pulsations and models for cavitation bubbles. J. Acoust. Soc. Am. 58, 1160–1170.

Fry, W.J., Fry, F.J., 1960. Fundamental neurological research and human neurosurgery using intense ultrasound. IRE Trans. Med. Electron. ME-7, 166–181.

Gateau, J., Aubry, J.F., Pernot, M., Fink, M., Tanter, M., 2011. Combined passive detection and ultrafast active imaging of cavitation events induced by short pulses of high-intensity ultrasound. IEEE Trans. Ultrason. Ferroelectr. Freq. Control 58, 517–532.

Gianfelice, D., Gupta, C., Kucharczyk, W., Bret, P., Havill, D., Clemons, M., 2008. Palliative Treatment of Painful Bone Metastases with MR Imaging–guided Focused Ultrasound. Radiology 249, 355–363.

Gianfelice, D., Khiat, A., Amara, M., Belblidia, A., Boulanger, Y., 2003. MR imaging-guided focused ultrasound surgery of breast cancer: correlation of dynamic contrast-enhanced MRI with histopathologic findings. Breast Cancer Res. Treat. 82, 93–101.

Graham, S. j., Chen, L., Leitch, M., Peters, R. d., Bronskill, M. j., Foster, F. s., Henkelman, R. m., Plewes, D. b., 1999. Quantifying tissue damage due to focused ultrasound heating observed by MRI. Magn. Reson. Med. 41, 321–328.

Greenspan, M., Tschiegg, C., 1967. Radiation-induced acoustic cavitation apparatus and some results. J Res Nat Bur Stand 71C, 299.

Gyöngy, M., 2010. Passive Cavitation Mapping for Monitoring Ultrasound Therapy. University of Oxford.

Gyongy, M., Arora, M., Noble, J.A., Coussios, C.-C., 2008. Use of passive arrays for characterization and mapping of cavitation activity during HIFU exposure. Presented at the IEEE Ultrasonics Symposium, 2008. IUS 2008, pp. 871–874.

Gyongy, M., Coussios, C.-C., 2010. Passive Spatial Mapping of Inertial Cavitation During HIFU Exposure. IEEE Trans. Biomed. Eng. 57, 48–56.

Gyöngy, M., Coussios, C.-C., 2010. Passive cavitation mapping for localization and tracking of bubble dynamics. J. Acoust. Soc. Am. 128, EL175-EL180.

Hamilton, M.F., Blackstock, D.T., 1998. Nonlinear Acoustics. Academic Press.

Harvey, E.N., Barnes, D.K., McElroy, W.D., Whiteley, A.H., Pease, D.C., Cooper, K.W., 1944. Bubble formation in animals. I. Physical factors. J. Cell. Comp. Physiol. 24, 1–22.

Hill, C.R., ter Haar, G.R., 1995. High intensity focused ultrasound—potential for cancer treatment. Br. J. Radiol. 68, 1296–1303.

Hindley, J., Gedroyc, W.M., Regan, L., Stewart, E., Tempany, C., Hynnen, K., Macdanold, N., Inbar, Y., Itzchak, Y., Rabinovici, J., Kim, K., Geschwind, J.-F., Hesley, G., Gostout, B., Ehrenstein, T., Hengst, S., Sklair-Levy, M., Shushan, A., Jolesz, F., 2004. MRI Guidance of Focused Ultrasound Therapy of Uterine Fibroids: Early Results. Am. J. Roentgenol. 183, 1713–1719.

Holt, R.G., Crum, L.A., 1992. Acoustically forced oscillations of air bubbles in water: Experimental results. J. Acoust. Soc. Am. 91, 1924–1932.

Holt, R.G., Roy, R.A., 2001. Measurements of bubble-enhanced heating from focused, mhz-frequency ultrasound in a tissue-mimicking material. Ultrasound Med. Biol. 27, 1399–1412.

Hu, H., Xu, S., Yuan, Y., Liu, R., Wang, S., Wan, M., 2015. Spatial-temporal ultrasound imaging of residual cavitation bubbles around a fluid–tissue interface in histotripsy. J. Acoust. Soc. Am. 137, 2563–2572.

Huber, P.E., Jenne, J.W., Rastert, R., Simiantonakis, I., Sinn, H.P., Strittmatter, H.J., von Fournier, D., Wannenmacher, M.F., Debus, J., 2001. A new noninvasive approach in breast cancer therapy using magnetic resonance imaging-guided focused ultrasound surgery. Cancer Res. 61, 8441–8447.

Huisman, H.J., Thijssen, J.M., 1996. Precision and accuracy of acoustospectrographic parameters. Ultrasound Med. Biol. 22, 855–871.

Hynynen, K., Clement, G.T., McDannold, N., Vykhodtseva, N., King, R., White, P.J., Vitek, S., Jolesz, F.A., 2004. 500-element ultrasound phased array system for noninvasive focal surgery of the brain: A preliminary rabbit study with ex vivo human skulls. Magn. Reson. Med. 52, 100–107.

Hynynen, K., Freund, W., Cline, H., Chung, A., Watkins, R., Vetro, J., Jolesz, F., 1996. A clinical, noninvasive, MR imaging-monitored ultrasound surgery method. RadioGraphics 16, 185–195.

Hynynen, K., McDannold, N., Sheikov, N.A., Jolesz, F.A., Vykhodtseva, N., 2005. Local and reversible blood–brain barrier disruption by noninvasive focused ultrasound at frequencies suitable for trans-skull sonications. NeuroImage 24, 12–20.

Hynynen, K., McDannold, N., Vykhodtseva, N., Jolesz, F.A., 2001a. Noninvasive MR Imaging–guided Focal Opening of the Blood-Brain Barrier in Rabbits. Radiology 220, 640–646.

Hynynen, K., Pomeroy, O., Smith, D.N., Huber, P.E., McDannold, N.J., Kettenbach, J., Baum, J., Singer, S., Jolesz, F.A., 2001b. MR Imaging-guided Focused Ultrasound Surgery of Fibroadenomas in the Breast: A Feasibility Study. Radiology 219, 176–185.

Jackson, E.J., Coussios, C.-C., Cleveland, R.O., 2014. Nonlinear acoustic properties of ex vivo bovine liver and the effects of temperature and denaturation. Phys. Med. Biol. 59, 3223.

Jenne, J.W., Preusser, T., Günther, M., 2012. High-intensity focused ultrasound: Principles, therapy guidance, simulations and applications. Z. Für Med. Phys., Schwerpunkt: Multimodale Bildgebung und Therapie 22, 311–322.

Jensen, C.R., Cleveland, R.O., Coussios, C.C., 2013. Real-time temperature estimation and monitoring of HIFU ablation through a combined modeling and passive acoustic mapping approach. Phys. Med. Biol. 58, 5833.

Jensen, C.R., Ritchie, R.W., Gyöngy, M., Collin, J.R.T., Leslie, T., Coussios, C.-C., 2012. Spatiotemporal monitoring of high-intensity focused ultrasound therapy with passive acoustic mapping. Radiology 262, 252–261.

Jespersen, S.K., Wilhjelm, J.E., Sillesen, H., 1998. Multi-Angle Compound Imaging. Ultrason. Imaging 20, 81–102.

Jones, R.M., O'Reilly, M.A., Hynynen, K., 2013. Transcranial passive acoustic mapping with hemispherical sparse arrays using CT-based skull-specific aberration corrections: a simulation study. Phys. Med. Biol. 58, 4981.

Kennedy, J.E., 2005. High-intensity focused ultrasound in the treatment of solid tumours. Nat. Rev. Cancer 5, 321–327.

Khokhlova, V.A., Bailey, M.R., Reed, J.A., Cunitz, B.W., Kaczkowski, P.J., Crum, L.A., 2006. Effects of nonlinear propagation, cavitation, and boiling in lesion formation by high intensity focused ultrasound in a gel phantom. J. Acoust. Soc. Am. 119, 1834–1848.

Khokhlova, V.A., Fowlkes, J.B., Roberts, W.W., Schade, G.R., Xu, Z., Khokhlova, T.D., Hall, T.L., Maxwell, A.D., Wang, Y.-N., Cain, C.A., 2015. Histotripsy methods in mechanical disintegration of tissue: Towards clinical applications. Int. J. Hyperthermia 31, 145–162.

Kinoshita, M., Hynynen, K., 2006. Mechanism of Porphyrin-Induced Sonodynamic Effect: Possible Role of Hyperthermia. Radiat. Res. 165, 299–306. doi:10.1667/RR3510.1

Kolb, J., Nyborg, W.L., 1956. Small-Scale Acoustic Streaming in Liquids. J. Acoust. Soc. Am. 28, 1237–1242.

Konofagou, E.E., Hynynen, K., 2003. Localized harmonic motion imaging: theory, simulations and experiments. Ultrasound Med. Biol. 29, 1405–1413.

Kremkau, F.W., 1979. Cancer therapy with ultrasound: a historical review. J. Clin. Ultrasound JCU 7, 287–300.

Kwan, J.J., Myers, R., Coviello, C.M., Graham, S.M., Shah, A.R., Stride, E., Carlisle, R.C., Coussios, C.C., 2015. Ultrasound-Propelled Nanocups for Drug Delivery. Small 11, 5305–5314.

Leighton, T.G., 1997. The Acoustic Bubble.

Leighton, T.G., 1995. Bubble population phenomena in acoustic cavitation. Ultrason. Sonochem. 2, S123–S136.

Lepock, J.R., Frey, H.E., Ritchie, K.P., 1993. Protein denaturation in intact hepatocytes and isolated cellular organelles during heat shock. J. Cell Biol. 122, 1267–1276.

Li, J., Stoica, P., Wang, Z., 2003. On robust Capon beamforming and diagonal loading. IEEE Trans. Signal Process. 51, 1702–1715.

Liang, H.-D., Tang, J., Halliwell, M., 2010. Sonoporation, drug delivery, and gene therapy. Proc. Inst. Mech. Eng. [H] 224, 343–361.

Lighthill, J., 2001. Waves in Fluids. Cambridge University Press.

Lighthill, S.J., 1978. Acoustic streaming. J. Sound Vib. 61, 391–418.

Lizzi, F.L., Muratore, R., Deng, C.X., Ketterling, J.A., Alam, S.K., Mikaelian, S., Kalisz, A., 2003. Radiation-force technique to monitor lesions during ultrasonic therapy. Ultrasound Med. Biol. 29, 1593–1605.

Madanshetty, S.I., Roy, R.A., Apfel, R.E., 1991. Acoustic microcavitation: Its active and passive acoustic detection. J. Acoust. Soc. Am. 90, 1515–1526.
Maleke, C., Konofagou, E.E., 2008. Harmonic motion imaging for focused ultrasound (HMIFU): a fully integrated technique for sonication and monitoring of thermal ablation in tissues. Phys. Med. Biol. 53, 1773.
Mast, T.D., 2007. Fresnel approximations for acoustic fields of rectangularly symmetric sources. J. Acoust. Soc. Am. 121, 3311–3322.
McDannold, N., Vykhodtseva, N., Hynynen, K., 2008. Blood-Brain Barrier Disruption Induced by Focused Ultrasound and Circulating Preformed Microbubbles Appears to Be Characterized by the Mechanical Index. Ultrasound Med. Biol. 34, 834–840.
McDannold, N., Vykhodtseva, N., Hynynen, K., 2006. Targeted disruption of the blood–brain barrier with focused ultrasound: association with cavitation activity. Phys. Med. Biol. 51, 793.
McLaughlan, J., Rivens, I., Leighton, T., ter Haar, G., 2010. A Study of Bubble Activity Generated in Ex Vivo Tissue by High Intensity Focused Ultrasound. Ultrasound Med. Biol. 36, 1327–1344.
Miller, N.R., Bamber, J.C., ter Haar, G.R., 2004. Imaging of temperature-induced echo strain: preliminary in vitro study to assess feasibility for guiding focused ultrasound surgery. Ultrasound Med. Biol. 30, 345–356.
Minnaert, M., 1933. XVI. On musical air-bubbles and the sounds of running water.
Mitragotri, S., Kost, J., 2004. Low-frequency sonophoresis: A review. Adv. Drug Deliv. Rev., Breaking the Skin Barrier 56, 589–601.
Mo, S., Coussios, C.-C., Seymour, L., Carlisle, R., 2012. Ultrasound-enhanced drug delivery for cancer. Expert Opin. Drug Deliv. 9, 1525–1538.
Montaldo, G., Tanter, M., Bercoff, J., Benech, N., Fink, M., 2009. Coherent plane-wave compounding for very high frame rate ultrasonography and transient elastography. IEEE Trans. Ultrason. Ferroelectr. Freq. Control 56, 489–506.
Muir, T.G., Carstensen, E.L., 1980. Prediction of nonlinear acoustic effects at biomedical frequencies and intensities. Ultrasound Med. Biol. 6, 345–357.
Nandlall, S.D., Arora, M., Schiffter, H.A., Coussios, C.-C., 2009. On the Applicability of the Thermal Dose Cumulative Equivalent Minutes Metric to the Denaturation of Bovine Serum Albumin in a Polyacrylamide Tissue Phantom, in: AIP Conference Proceedings. Presented at the 8TH INTERNATIONAL SYMPOSIUM ON THERAPEUTIC ULTRASOUND, AIP Publishing, pp. 205–209.
Narayana, P.A., Ophir, J., 1983. On the Frequency Dependence of Attenuation in Normal and Fatty Liver. IEEE Trans. Sonics Ultrason. 30, 379–382.
Neppiras, E.A., 1980. Acoustic cavitation. Phys. Rep. 61, 159–251.
Norton, S.J., Won, I.J., 2000. Time exposure acoustics. IEEE Trans. Geosci. Remote Sens. 38, 1337–1343.
Nyborg, W.L., 1958. Acoustic Streaming near a Boundary. J. Acoust. Soc. Am. 30, 329–339.
Okada, A., Murakami, T., Mikami, K., Onishi, H., Tanigawa, N., Marukawa, T., Nakamura, H., 2006. A case of hepatocellular carcinoma treated by MR-guided focused ultrasound ablation with respiratory gating. Magn. Reson. Med. Sci. MRMS Off. J. Jpn. Soc. Magn. Reson. Med. 5, 167–171.
O'Reilly, M.A., Jones, R.M., Hynynen, K., 2014. Three-Dimensional Transcranial Ultrasound Imaging of Microbubble Clouds Using a Sparse Hemispherical Array. IEEE Trans. Biomed. Eng. 61, 1285–1294.
Peters, R.T.D., Hinks, R.S., Henkelman, R.M., 1998. Ex vivo tissue-type independence in proton-resonance frequency shift MR thermometry. Magn. Reson. Med. 40, 454–459.
Plesset, M.S., Chapman, R.B., 1971. Collapse of an initially spherical vapour cavity in the neighbourhood of a solid boundary. J. Fluid Mech. 47, 283.
Quesson, B., de Zwart, J.A., Moonen, C.T.W., 2000. Magnetic resonance temperature imaging for guidance of thermotherapy. J. Magn. Reson. Imaging 12, 525–533.

Rabkin, B.A., Zderic, V., Crum, L.A., Vaezy, S., 2006. Biological and physical mechanisms of HIFU-induced hyperecho in ultrasound images. Ultrasound Med. Biol. 32, 1721–1729.
Rabkin, B.A., Zderic, V., Vaezy, S., 2005. Hyperecho in ultrasound images of HIFU therapy: Involvement of cavitation. Ultrasound Med. Biol. 31, 947–956.
Ribault, M., Chapelon, J.Y., Cathignol, D., Gelet, A., 1998. Differential attenuation imaging for the characterization of high intensity focused ultrasound lesions. Ultrason. Imaging 20, 160–177.
Rivens, I., Shaw, A., Civale, J., Morris, H., 2007. Treatment monitoring and thermometry for therapeutic focused ultrasound. Int. J. Hyperthermia 23, 121–139.
Roberts, W.W., Hall, T.L., Ives, K., Wolf, J.S., Fowlkes, J.B., Cain, C.A., 2006. Pulsed Cavitational Ultrasound: A Noninvasive Technology for Controlled Tissue Ablation (Histotripsy) in the Rabbit Kidney. J. Urol. 175, 734–738.
Roy, R.A., Madanshetty, S., Apfel, R.E., 1988. An active acoustic backscattering technique for detecting transient cavitation. J. Acoust. Soc. Am. 83, S108–S108.
Salgaonkar, V.A., Datta, S., Holland, C.K., Mast, T.D., 2009. Passive cavitation imaging with ultrasound arrays. J. Acoust. Soc. Am. 126, 3071–3083.
Sandrin, L., Catheline, S., Tanter, M., Hennequin, X., Fink, M., 1999. Time-Resolved Pulsed Elastography with Ultrafast Ultrasonic Imaging. Ultrason. Imaging 21, 259–272.
Sapareto, S.A., Dewey, W.C., 1984. Thermal dose determination in cancer therapy. Int. J. Radiat. Oncol. 10, 787–800.
Sapozhnikov, O.A., Khokhlova, V.A., Bailey, M.R., Jr, J.C.W., McAteer, J.A., Cleveland, R.O., Crum, L.A., 2002. Effect of overpressure and pulse repetition frequency on cavitation in shock wave lithotripsy. J. Acoust. Soc. Am. 112, 1183–1195.
Sass, W., Bräunlich, M., Dreyer, H.P., Matura, E., Folberth, W., Preismeyer, H.G., Seifert, J., 1991. The mechanisms of stone disintegration by shock waves. Ultrasound Med. Biol. 17, 239–243.
Schneider, M., 1999. SonoVue, a new ultrasound contrast agent. Eur. Radiol. 9, S347–S348.
Senneville, B.D. de, Mougenot, C., Quesson, B., Dragonu, I., Grenier, N., Moonen, C.T.W., 2007. MR thermometry for monitoring tumor ablation. Eur. Radiol. 17, 2401–2410.
Shen, C.-C., Chou, Y.-H., Li, P.-C., 2005. Pulse Inversion Techniques in Ultrasonic Nonlinear Imaging. J. Med. Ultrasound 13, 3–17.
Soltani, A., Singhal, R., Obtera, M., Roy, R.A., Clark, W.M., Hansmann, D.R., 2011. Potentiating intra-arterial sonothrombolysis for acute ischemic stroke by the addition of the ultrasound contrast agents (Optison™ & SonoVue®). J. Thromb. Thrombolysis 31, 71–84.
Stewart, E.A., Gedroyc, W.M.W., Tempany, C.M.C., Quade, B.J., Inbar, Y., Ehrenstein, T., Shushan, A., Hindley, J.T., Goldin, R.D., David, M., Sklair, M., Rabinovici, J., 2003. Focused ultrasound treatment of uterine fibroid tumors: Safety and feasibility of a noninvasive thermoablative technique. Am. J. Obstet. Gynecol. 189, 48–54.
Stoica, P., Wang, Z., Li, J., 2003. Robust Capon beamforming. IEEE Signal Process. Lett. 10, 172–175.
Stride, E.P., Coussios, C.C., 2010. Cavitation and contrast: The use of bubbles in ultrasound imaging and therapy. Proc. Inst. Mech. Eng. [H] 224, 171–191.
Szabo, T.L., 2004. Diagnostic Ultrasound Imaging: Inside Out. Academic Press.
Techavipoo, U., Varghese, T., Chen, Q., Stiles, T.A., Zagzebski, J.A., Frank, G.R., 2004. Temperature dependence of ultrasonic propagation speed and attenuation in excised canine liver tissue measured using transmitted and reflected pulses. J. Acoust. Soc. Am. 115, 2859–2865.
ter Haar, G., 2007. Therapeutic applications of ultrasound. Prog. Biophys. Mol. Biol. 93, 111–129.
ter Haar, G., Coussios, C., 2007a. High Intensity Focused Ultrasound: Past, present and future. Int. J. Hyperthermia 23, 85–87.

ter Haar, G., Coussios, C., 2007b. High intensity focused ultrasound: Physical principles and devices. Int. J. Hyperthermia 23, 89–104.
ter Haar, G.R., Clarke, R.L., Vaughan, M.G., Hill, C.R., 1991. Trackless surgery using focused ultrasound: Technique and case report. Minim. Invasive Ther. 1, 13–19.
Thomas, J.D., Rubin, D.N., 1998. Tissue harmonic imaging: Why does it work? J. Am. Soc. Echocardiogr. 11, 803–808.
Uhlendorf, V., Scholle, F.-D., Reinhardt, M., 2000. Acoustic behaviour of current ultrasound contrast agents. Ultrasonics 38, 81–86.
Unger, E.C., Matsunaga, T.O., McCreery, T., Schumann, P., Sweitzer, R., Quigley, R., 2002. Therapeutic applications of microbubbles. Eur. J. Radiol. 42, 160–168.
Van Veen, B.D., Buckley, K.M., 1988. Beamforming: a versatile approach to spatial filtering. IEEE ASSP Mag. 5, 4–24.
Wan, M., Feng, Y., Haar, G. ter (Eds.), 2015. Cavitation in Biomedicine. Springer Netherlands, Dordrecht.
Wells, P.N., 1977. Ultrasonics in medicine and biology. Phys. Med. Biol. 22, 629–669.
Wood, R.W., Loomis, A.L., 1927. The physical and biological effects of high-frequency sound-waves of great intensity. Lond. Edinb. Dublin Philos. Mag. J. Sci. 4, 417–436.
Xu, Z., Fowlkes, J.B., Rothman, E.D., Levin, A.M., Cain, C.A., 2005. Controlled ultrasound tissue erosion: The role of dynamic interaction between insonation and microbubble activity. J. Acoust. Soc. Am. 117, 424–435.
Yu, T., Xu, C., 2008. Hyperecho as the Indicator of Tissue Necrosis During Microbubble-Assisted High Intensity Focused Ultrasound: Sensitivity, Specificity and Predictive Value. Ultrasound Med. Biol. 34, 1343–1347.

CHAPTER

2

OPTIMAL PASSIVE BEAMFORMING USING HIGHER ORDER STATISTICS

2.1 INTRODUCTION

The different steps involved in the pipeline of PAM allow independent improvements that could potentially enhance its accuracy and reliability. The discussion regarding the choice of beamforming algorithm for PAM revealed the importance of using optimal data-dependent beamforming techniques, as a way to approach and even surpass the diffraction resolution limits of the passive array. In addition, optimal beamforming techniques can mitigate the impact of errors arising from variability in the geometric arrangement or sensitivity of the receiving array setup configuration, making natural candidates to facilitate the use of PAM in a clinical scenario.

The only algorithm currently satisfying the above criteria is RCB, but its main limitation is the assumption that the signals-of-interest follow a Gaussian distribution. This assumption arises from the fact that the weight calculation in RCB is based on the minimisation of the variance of the array output, and the solution uses the covariance

matrix of the signals recorded by the array elements. In statistical terms, in minimising the variance of a signal, only the second-order statistics of the signal are taken into consideration: it is therefore, assumed that the higher-order statistics of the signals are zero, which may not always be valid for signals passively received during ultrasound therapy.

There has already been considerable research in biomedical signal processing based on the higher order statistics of the signals (Chua et al., 2010). In this chapter, a beamforming algorithm is proposed in the context of PAM that exploits the mean and variance of the array output, as well as its higher-order-statistics, in the calculation of the weights, to exploit as much information hidden in the recorded signals as possible. The performance of the beamformer is evaluated through simulations and *in vitro* experimentation in terms of source energy estimation and resolvability, in order to ultimately assess its contribution in the improvement of the spatial resolution of PAM.

2.2 HIGHER-ORDER-STATISTICS-BASED BEAMFORMING

2.2.1 INTRODUCTION TO HIGHER-ORDER-STATISTICS (HOS)

In signal processing, and even more specifically in beamforming theory, power spectra and the autocorrelation functions are some of the main tools used for data analysis, parameter estimation and signal reconstruction. However, the information contained in these tools is only sufficient for the description of a Gaussian process of known mean and variance. The arithmetic mean and variance belong to the low-order statistics, and more specifically they are known as first- and second-order measures. Their natural extension is the HOS, i.e. measures of order higher than 2, and in practice the n^{th}-order moment and n^{th}-order cumulant are used to describe the HOS in either the time or frequency domain (Bronzino, 2000; Chua et al., 2010, 2010; Mendel, 1991). Simultaneously, the extension of the power spectrum is the higher-order spectra (polyspectra) defined by the multi-dimensional Fourier transform of the higher order cumulants (Bronzino, 2000; Tong and Thakor, 2009).

HOS have a long history of application in a wide variety of fields related to signal processing, such as blind source separation and blind array beamforming (Cardoso, 1989; Cardoso and Souloumiac, 1993; Nandi, 2013; Thi and Jutten, 1995), and have also found application in biomedical signal processing, such as in array signal processing for medical imaging and processing of physiological signals (Abeyratne et al., 1995; Khadra et al., 2005; Muthuswamy et al., 1999). The motivation behind the use of HOS is based on the fact that higher-order spectra provide information related to amplitude and phase of non-Gaussian processes. This can enable separation of additive

mixtures of non-Gaussian signals of interest from background noise or interfering signals that follow a Gaussian distribution.

Several beamformers based on HOS have been proposed in the optimum array processing literature. Adaptive beamforming based on HOS has been attempted in the field of far-field speech recognition using kurtosis (the fourth-order moment) or negentropy maximisation achieving efficient noise and reverberation suppression (Kumatani et al., 2013, 2010, 2008). A polyspectra approach has also been proposed for source detection and parameter estimation of wideband sources demonstrating optimal performance for non-Gaussian signals in the presence of additive Gaussian noise (Shamsunder and Giannakis, 1991). Additionally, a linearly-constraint minimum variance beamformer re-formulated for non-Gaussian probability density distributions has been proposed for brain activity localisation from magnetoencephalographic (MEG) data. However, it requires a priori knowledge or accurate estimation of the probability density function of the signals.

2.2.2 ROBUST BEAMFORMING BY LINEAR PROGRAMMING (RLPB)

In the context of PAM, the only optimal beamforming algorithm previously proposed is RCB, which assumes a Gaussian distribution of the mixture of signals received at the array. However, the robustness of RCB in steering vector mismatches is a desirable feature in array beamforming that allows flexibility in the conditions under which the signals are recorded. These include accounting for mismatches between actual and nominal values of array element positions, sensitivity and speed of sound. If it is combined with a minimisation process that uses the HOS of the received signals, there is an opportunity for an optimal beamforming technique that can potentially

exploit the full information hidden in signals with non-Gaussian distribution and provide higher signal-to-noise ratios by more efficiently separating the signal-of-interest from Gaussian background noise.

The beamforming technique with the features described above, and presented in this thesis, is Robust Beamforming by Linear Programming (RLPB)(Jiang et al., 2014). Considering an array of *M* sensors, the vector of the array output is

$$\boldsymbol{x}(n) = [x_1(n), \dots, x_M(n)\,]^T \tag{2.1}$$

and the beamformer output for a vector of *M* weights is

$$\boldsymbol{y}(n) = \boldsymbol{w}^H \boldsymbol{x}(n) \Leftrightarrow \boldsymbol{Y} = \boldsymbol{X}^H \boldsymbol{w} \tag{2.2}$$

Instead of minimising the variance of the beamformer output, the proposed beamformer minimises the l_∞-norm of the beamformer output:

$$\min_{\boldsymbol{w}} \|\boldsymbol{X}^T \boldsymbol{w}\|_\infty \qquad s.t. \quad |(\boldsymbol{a}+\boldsymbol{e})^T \boldsymbol{w}|_\infty \geq 1 \; for\; all\; \boldsymbol{e} \in \mathcal{E} \tag{2.3}$$

where $\boldsymbol{w}, \boldsymbol{a}, \boldsymbol{e} \in \mathbb{R}^M$ and $\boldsymbol{X} \in \mathbb{R}^{M \times N}$. The constraint imposed in the minimisation problem in (2.3) allows the steering vector $\boldsymbol{a}$ to vary by a steering vector error $\boldsymbol{e}$**.** This creates an uncertainty region, similar to that of RCB, that will account for steering vector mismatches in order to ensure that the magnitude response of the beamformer for the signal-of-interest is not attenuated. The uncertainty region is modelled as a rhombus $\mathcal{E} = \{\boldsymbol{e} | \|\boldsymbol{e}\|_1 \leq \varepsilon_1\}$, in which ε_1 defines the size of the uncertainty region.

At this point the general definition of the l_∞-norm of a complex vector $\boldsymbol{z}$ needs to be introduced, and it is defined according to the following equations (Jiang et al., 2014):

$\boldsymbol{l_p}$-modulus of a complex number $\boldsymbol{v}$	$$\lvert \boldsymbol{v} \rvert_{\boldsymbol{p}} = (\lvert \boldsymbol{v_R} \rvert^{\boldsymbol{p}} + \lvert \boldsymbol{v_I} \rvert^{\boldsymbol{p}})^{\boldsymbol{1/p}}$$	(2.4)
$\boldsymbol{l_p}$-norm of $\boldsymbol{z}$	$$\lVert \boldsymbol{z} \rVert_p = \left(\sum_{i=1}^{M} \lvert z_i \rvert_p^p \right)^{1/p} = \left(\sum_{i=1}^{M} \lvert \Re(z_i) \rvert^p + \lvert \Im(z_i) \rvert^p \right)^{1/p}$$	(2.5)
$\boldsymbol{l_\infty}$-norm of $\boldsymbol{z}$	$$\lVert \boldsymbol{z} \rVert_\infty = \lim_{p \to \infty} \lVert \boldsymbol{z} \rVert_p = \max_{1 \le i \le M} \lvert z_i \rvert_\infty = \max_{1 \le i \le M} \left(\max(\lvert \Re(z_i) \rvert, \lvert \Im(z_i) \rvert) \right)$$	(2.6)

The main limitation in solving efficiently the problem in (2.3) is the infinite number of constraints, and therefore, the problem is reformulated (Jiang et al., 2014):

$$\min_{\boldsymbol{w}} \lVert \boldsymbol{X}^T \boldsymbol{w} \rVert_\infty \qquad s.t. \qquad \boldsymbol{a}^T \boldsymbol{w} - \varepsilon_1 \lVert \boldsymbol{w} \rVert_\infty \geq 1 \; for \; all \; \boldsymbol{e} \in \mathcal{E} \tag{2.7}$$

The new formulation contains only a single constraint and it can be converted in a linear programming problem using two extra variables $u, r \in \mathbb{R}$:

$$\min_{\boldsymbol{w},u,r} u \qquad s.t. \qquad \begin{cases} -u\mathbf{1}_N \leq \boldsymbol{X}^H \boldsymbol{w} \leq u\mathbf{1}_N \\ \boldsymbol{a}^T \boldsymbol{w} \geq 1 + \varepsilon_1 r \\ -r\mathbf{1}_M \leq \boldsymbol{w} \leq r\mathbf{1}_M \end{cases} \tag{2.8}$$

Linear programming problems can be solved using either the simplex method or the interior points method and its variants (Nocedal and Wright, 2006). In the present work, the linear programming problem is solved using the MATLAB embedded function *linprog*. This function implements the primal-dual infeasible-interior-point algorithm specifically designed for large-scale linear programming problems (Zhang, 1995).

As it is also the case for RCB, the value of ε_1, the uncertainty parameter, significantly affects the performance of the beamformer, and the selection of the appropriate value depends on a combination of factors. More specifically, assuming no *a priori* knowledge on the setup configuration, a characterisation of ε_1 needs to be performed in order to find the best compromise between interference suppression and tolerance in steering vector mismatches. As the value of ε_1 increases, the uncertainty region expands allowing more flexibility to the steering vector and therefore, calibration errors and deviations from the actual speed of sound in the propagation medium can be addressed more efficiently. On the other hand, interfering signals from regions close to the uncertainty region will not be as efficiently suppressed as they would be in the case of a smaller ε_1, resulting in errors in the source energy estimation and spatial resolution of the beamformer. In (Jiang et al., 2014) a coarse upper limit of ε_1 is defined, $\varepsilon_1 \leq \|\boldsymbol{a}\|_1$, that ensures the minimisation problem is feasible. It is also suggested that *a priori* information on the causes of steering vector mismatches can be exploited to acquire a more optimal value for ε_1.

Minimisation of the l_∞-norm of the array output in RLPB is suggested as a beamforming approach that exploits the HOS of the recorded signal. However, the link between the l_∞-norm and the HOS is not intuitive, and statistical analysis of the definition of the RLPB minimisation problem can provide a useful explanation (Jiang et al., 2014). Assuming the beamformer output is defined as:

$$\boldsymbol{y}(n) = \boldsymbol{g}^T \boldsymbol{b} = \sum_{\boldsymbol{i=1}}^{\boldsymbol{L}} g_i b_i(n) \tag{2.9}$$

in which $\boldsymbol{g} \epsilon \mathbb{R}^{\boldsymbol{L}}$ represents the combined array and beamformer response, $\boldsymbol{b} \epsilon \mathbb{R}^{\boldsymbol{L}}$ consists of all the signals recorded (including the signal-of-interest, any interfering signals and

background noise), and $L = I + 2$ is the total number of signal components for I interfering signals.

Minimisation of the l_∞-norm of the beamformer output is equivalent to the minimisation of the following objective function, by replacing the expectation with the sample mean and allowing p to reach infinity:

$$f_p(\boldsymbol{b}) = E\{|y(n)|_p^p\} = \frac{1}{N}\sum_{n=1}^{N}|y(n)|_p^p = \frac{1}{N}\left(\|\boldsymbol{y}\|_p\right)^p$$

$$\lim_{p\to\infty} f_p(\boldsymbol{b}) = \lim_{p\to\infty}\frac{1}{N}\left(\|\boldsymbol{y}\|_p\right)^p = \frac{1}{N}\left(\lim_{p\to\infty}\|\boldsymbol{y}\|_p\right)^p \tag{2.10}$$

$$\min\left(\lim_{p\to\infty} f_p(\boldsymbol{b})\right) = \min\left(\frac{1}{N}\left(\lim_{p\to\infty}\|\boldsymbol{y}\|_p\right)^p\right) = \min(\|\boldsymbol{y}\|_\infty)$$

Since $\boldsymbol{y}\epsilon\mathbb{R}^{\boldsymbol{L}}$, and according to the l_p-modulus definition for a vector $\boldsymbol{z}$, $|\boldsymbol{z}|_p = (|z_R|^p + |z_I|^p)^{1/p}$, the objective function is now:

$$f_p(\boldsymbol{b}) = E\{|y(n)|_p^p\} = E\{|y(n)|^p\} = E\left\{\left|\sum_{i=1}^{L} g_i b_i(n)\right|^p\right\} = E\left\{f_R^{(p)}(\boldsymbol{b})\right\} \tag{2.11}$$

By applying Taylor series expansion, approximation of $f_R^{(p)}(\boldsymbol{b})$ can be obtained and, overall, the l_∞-norm of the beamformer output can be expressed as:

$$\|\boldsymbol{y}\|_\infty = E\left\{f_R^{(\infty)}(\boldsymbol{b})\right\} = \lim_{p\to\infty}\left(\sum_{k=1}^{\infty}\frac{1}{k!}\sum_{i_1=1}^{L}\dots\sum_{i_k=1}^{L}\left.\frac{\partial^k f_R^{(p)}}{\partial b_{i1}\dots\partial b_{ik}}\right|_{\boldsymbol{b}=\boldsymbol{0}} E\{b_{i1}\dots b_{ik}\}\right) \tag{2.12}$$

where k is the approximation order of the Taylor series.

In the above equation, $E\{b_{i1} \dots b_{ik}\}$ has a different value for different combinations of $\{i_1, \dots, i_k\}$. Defining the k[th]-order moment of b_i as $E\{b_i^k\}$ for $1 \leq k \leq \infty$, and considering all the elements in $\boldsymbol{b}$ independent with each other, the HOS of the recorded signals are represented by the various moments of b_i:

$$E\{b_{i1} \dots b_{ik}\} = \begin{cases} E\{b_i^k\} \quad if\ i_1 = \cdots = i_k = i \\ E\{b_{i_1}^2\}E\{b_{i_3}^2\} \dots E\{b_{i_{k-1}}^2\} \quad if\ i_1 = i_2, i_3 = i_4, \dots, i_{k-1} = i_k \\ E\{b_{i_1}^4\}E\{b_{i_5}^4\} \dots E\{b_{i_{k-3}}^4\} \quad if\ i_1 = \cdots = i_4, \dots, i_{k-3} = \cdots = i_k \\ \vdots \\ 0 \end{cases} \tag{2.13}$$

In the context of PAM, RLPB can be combined with the set of steps of PAM presented in Chapter 1 to provide the calculation of weights $\boldsymbol{w}$ from the pre-steered and amplitude-compensated signals recorded by the elements of the array. In order to provide a physical meaning of the optimisation attempted in this algorithm, it would be useful to consider, first, the optimisation problem in RCB. Minimisation of the variance of the array output, as already discussed in Chapter 1, aims at minimising the power of the signals originating from locations other than the location of interest (i.e. interferences), while preserving the power of the desired signals. Considering the problem from a statistical point of view, it is attempted to decrease the variance of the Gaussian distribution of the array output, interpreted as more signal samples approaching the mean (assuming a zero mean). However, when the distribution of the array output deviates from the Gaussian, then such an optimisation is expected to not be sufficient for interfering signals suppression. Therefore, minimisation of the variance along with all the other higher order statistics (e.g. skewness, kurtosis etc) of the recorded signals is proposed to address this problem.

As far as the weights calculated via the optimisation problem are concerned, it is important to point out that they are defined in the original papers as complex numbers. For reasons of simplicity and compliance with RCB, it has been chosen to represent $\boldsymbol{w}$ as a vector of real numbers that allows adjustments only on the amplitude of the signals from each element of the array as part of the beamforming process. Additionally, the weights are restricted to be positive in order to avoid 180^o shift in signal phase due to negative weights. The advantages and disadvantages related to the choice of real instead of complex weights, as well as the potential extension of PAM based on RLPB using complex weights will be discussed in detail further below.

2.3 NUMERICAL SIMULATIONS

As an initial evaluation of the newly proposed beamformer in the context of PAM it is important to assess the ability of the beamformer in estimating the source energy from a single source, in this case a gas bubble. In addition, the spatial resolution of PAM in conjunction with RLPB beamformer will be evaluated in comparison to the previously introduced TEA and RCB beamformers. For this purpose, a model of the emissions from a single spherical gas bubble due to large-amplitude oscillations is adopted that allows calculation of the bubble wall motion, and consecutively, the pressure wave radiated by the bubble, and its total energy. The emissions generated by one (in the case of source energy estimation) or two (in the case of spatial resolution evaluation) gas bubbles propagate spherically, they are recorded by either a spherical array that surrounds the sources, or a linear array, which is essentially a small portion of the spherical array, and they are processed with either of the three beamformers (TEA,

RCB, RLPB) in order to compare PAM performance in the context of the beamforming technique applied.

Keller-Miksis model of emissions from a single bubble

The Keller-Miksis model (Keller and Miksis, 1980) of large-amplitude radial oscillations from a single gas bubble in an infinite medium of compressible fluid has been chosen to describe the acoustic dynamics of the bubble in the presence of an incident acoustic field:

$$\left(1-\frac{\dot{R}}{c}\right)R\ddot{R}+\frac{3}{2}\left(1-\frac{\dot{R}}{3c}\right)\dot{R}^2=\left(1+\frac{\dot{R}}{c}\right)\frac{P_R-P_\infty}{\rho}+\frac{R}{\rho c}\frac{d}{dt}[P_R-P_\infty] \tag{2.14}$$

where R is the bubble radius, c the speed of sound in the medium, ρ the density of the medium, and P_R-P_∞ the difference between the static pressure in the medium and the pressure at the bubble wall defined as follows:

$$P_R-P_\infty=P_g+P_v-P_\infty-\frac{2\sigma}{R}+3\int_R^\infty\frac{\tau_{rr}}{r}dr+P_A \tag{2.15}$$

Assuming that the bubble contains a mixture of gas and vapor, the pressure of the gas part $P_g=KR^{-3\kappa}$ is defined at any point with respect to constants K and κ. The polytropic index κ is set to 1.4, and K is defined at the bubble equilibrium according to the relationship between all pressures experienced by the bubble in the absence of an acoustic field (Collin and Coussios, 2011):

$$K=\left(P_\infty-P_v+\frac{2\sigma}{R_0}\right){R_0}^{3\kappa} \tag{2.16}$$

in which R_0 is the bubble radius at the equilibrium.

The acoustic pressure is defined as $P_A = -P_0 \sin(2\pi f_A t)$, where P_0 is the absolute maximum amplitude of the acoustic wave and f_A its frequency. The ambient pressure P_∞ is set to 101kPa (Kwan et al., 2015). The surface tension of the water-air interface, the viscosity, the density and speed of sound of the medium, as well as the pressure of the vapour part of the bubble are parameters dependent on temperature, and their values are calculated at 20^{o}C according to the relationships provided in (Webb et al., 2011). Finally, considering the medium that surrounds the bubble as purely viscous, the shear stress integral that describes the effect of viscosity in the pressure gradient on the bubble wall is described by the following equation (Webb et al., 2011):

$$3\int_R^\infty \frac{\tau_{rr}}{r}\,dr = -\frac{4\mu\dot{R}}{R} \tag{2.17}$$

The solution of the Keller-Miksis equation provides a bubble radius over time relationship (R-t curve), and in the present work it has been obtained using the ode15s solver of MATLAB with an absolute tolerance of 1e-12.

Assuming that the array responsible for detecting the acoustic emissions originating from the oscillating and collapsing bubble is located at a distance greater than the bubble radius, the pressure detected from one sensor at distance r from the source can be approximated by the following equation (Yoshizawa et al., 2001):

$$P(r) = \frac{\rho R}{r}\left(2\dot{R}^2 + R\ddot{R}\right) \tag{2.18}$$

For the purposes of the first part of the simulations, the energy of the bubble needs to be calculated in order to compare it with the source energy estimated by PAM

using the three different beamformers. The bubble energy can be calculated from the following equation (Vogel et al., 1989):

$$E = \frac{4\pi r^2}{\rho c} \int p^2 dt \tag{2.19}$$

in which r denotes the distance between the centre of the bubble and the point where acoustic pressure p is evaluated, ρ and c are the density and speed of sound of the medium respectively.

Part I: Source energy estimation

In the first part of the simulations presented in this chapter, the overall aim is to evaluate the ability of the three different beamformers (TEA, RCB, and RLPB) to provide an accurate estimation of the source energy for the simple case of a single inertially cavitating bubble. Comparison of the three PAM beamformers in this context may potentially reveal limitations of the PAM method related to the choice of the beamforming algorithm.

The signal pathway, simulated using a combination of the Keller-Miksis model (Keller and Miksis, 1980; Collin and Coussios, 2011) and the PAM algorithm, is schematically presented in Fig. 2.1. The pressure waves generated due to the single bubble oscillations and inertial collapses propagate spherically and they are recorded by the elements of either a spherical array surrounding the single source, or a linear array that essentially corresponds to only a small portion of the spherical array. The two array configurations allow comparison of the source energy estimation performance using PAM depending on the set of angles by which signals that are reconstructed in PAM are recorded. Depending on the frequency response of the individual elements of the array,

the signals recorded are bandlimited according to the receive bandwidth of the elements. The case of infinite bandwidth, which is not achievable in reality, allows the pressure-to-voltage signal relationship to be equal to 1 for all frequencies. However, in the case of a limited bandwidth, the signals are band-passed, leading to significant signal loss due to removal of frequency components outside the bandwidth of the array elements.

The effect of the array frequency response, i.e. the array receive bandwidth, on the source energy estimation using PAM is also investigated in this section. As the voltage signal propagates through the electronics of the data acquisition system, electronic noise is added on top of the signal corresponding to the acoustic emissions. This signal is modelled in these simulations as white Gaussian noise, and its level is chosen to match the level of electronic noise as recorded from the Verasonics Vantage Research Ultrasound System (Verasonics, Inc., Redmont, WA). Considering, now, that an accurate calibration of all the array elements is available, reconstruction of the original signal can be achieved by de-convolving each array element signal with the array frequency response. Application of the PAM algorithm should then result in better recovery of the total source energy.

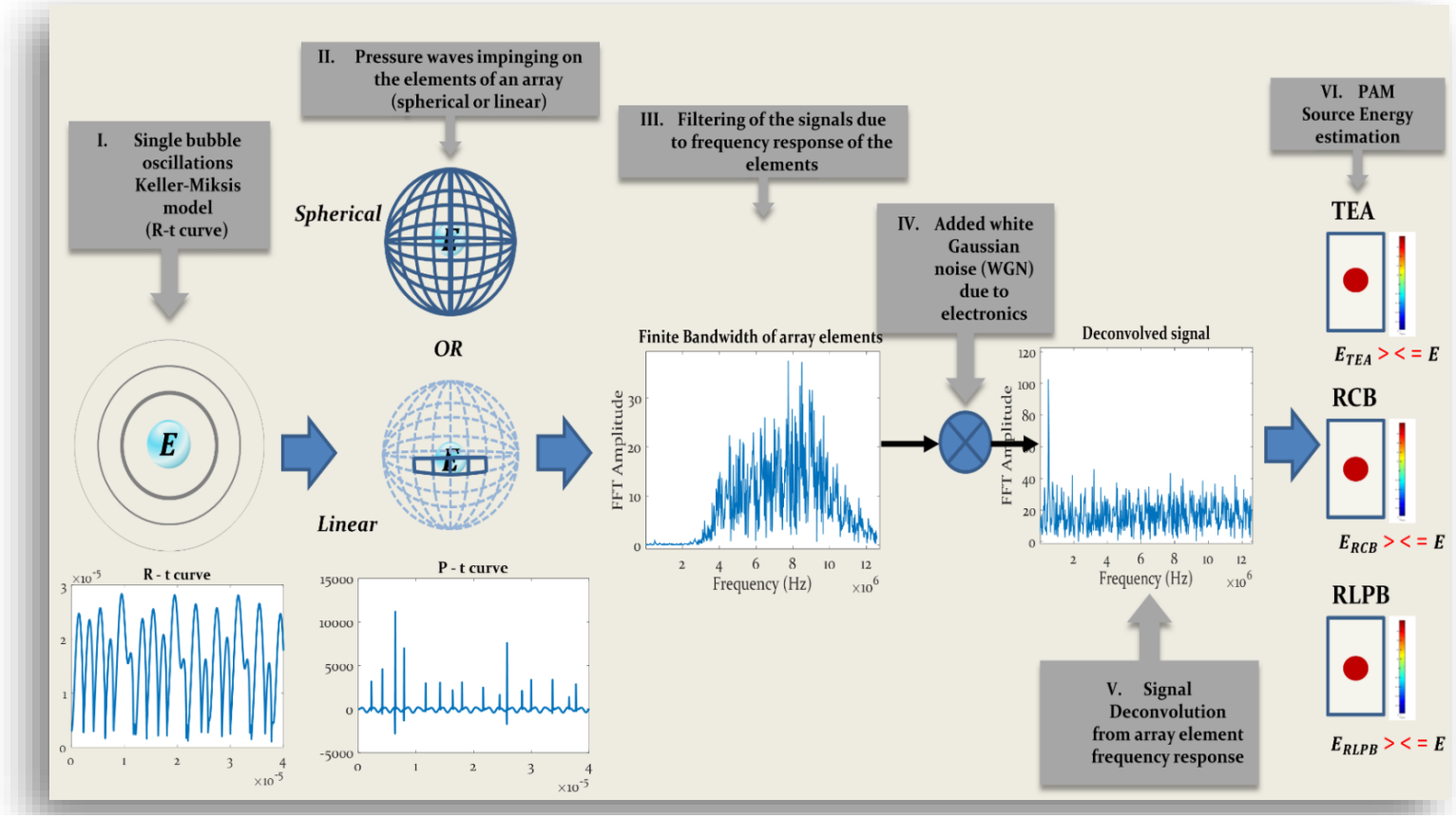


Figure 2.1 Schematic representation of the acoustic signal pathway modelled in the simulations for source energy estimation using PAM and evaluation of the PAM spatial resolution. The steps involved are: 1) acoustic emissions generation from a single bubble based on the Keller-Miksis model, 2) pressure signal recording by two array geometries, i.e. a spherical array surrounding the bubble, or a linear array that could be a considered as a portion of the spherical array, 3) filtering of the recording signals according to the frequency response of the individual elements of the array, 4) addition of white Gaussian noise in the signals of each element due to the electronics of the system, 5) array frequency response signal deconvolution for signal recovery, and 6) source energy estimation using PAM based on either TEA, RCB, or RLPB for a set of values for parameter ε.

The parameters chosen for the Keller-Miksis model and the PAM algorithm in this part of the simulations are summarised in Table 2.1.

Table 2.1 Keller-Miksis model and PAM algorithm parameters for simulation performed to evaluate the source energy estimation of a single bubble.

Keller-Miksis model parameters	PAM parameters
$\boldsymbol{R_0 = 3\mu m}$	$F_s = 25MHz$
$\boldsymbol{f_0 = 0.5MHz}$	$c = 1482m/s$
$\boldsymbol{P_0 = 1MPa}$	$\#\ array\ elements$: $Spherical = 121, Linear = 128$
$\boldsymbol{Number\ of\ cycles = 20}$	$\varepsilon = [5\ 10\ 15\ 20]$
$\boldsymbol{Distance\ from\ array = 75mm}$	

The signal pathway comprises multiple steps, presented in Fig. 2.1 and Fig. 2.2 and the potential impact of each step on the ability of PAM in estimating the source energy is investigated here. The results for the different combinations of components in the signal pathway are demonstrated in Fig. 2.2. In this figure, the maximum PAM energy in the PAM maps normalised with respect to the actual source energy is presented for the three beamformers, namely TEA, RCB and RLPB. For the last two data-adaptive beamformers, four different values of the parameter ε are evaluated.

Assessing first the impact of the array geometry, it is concluded that PAM is able to recover the total source energy from a single bubble regardless of the angles that the acoustic emissions are “listened” from, as it is able to compensate perfectly for the

spherical spreading of the acoustic waves. Additionally, the beamforming algorithms and the choice of the ε parameter do not affect the performance of the PAM algorithm.

The frequency response of each element of the array will result, as already briefly discussed, in a portion of the signal that is outside the bandwidth of the array elements being removed. In these simulations, the bandlimited frequency response is modelled on the actual frequency response of a Verasonics L11-4v linear array transducer (central frequency 6.25 MHz, 128 elements, pitch 0.298-0.302mm, sensitivity −64.5 to −59.5 dB, elevation focus 15-25 mm, Verasonics, Inc., Redmond, WA). It is expected that reconstruction of this band-passed signal will result in source energy underestimation by PAM, and this is confirmed by the subfigure in the last row of Fig. 2.2. It is, however, observed that the performance of PAM does not depend on the beamforming algorithm, since all three competing beamformers provide equal estimates of the source energy. In order for PAM to be able to recover the pressure signals impinging on the array, signal deconvolution with the impulse response of the array elements is required. Mapping of the de-convolved signals results in correct source energy estimation regardless of the beamforming technique, as demonstrated in the third row of Fig. 2.2. Finally, the last parameter investigated in this part of the simulations is the effect of added white Gaussian noise from the electronics of the data acquisition system. It is observed that this low-level broadband signal does not interfere destructively with the signal-of-interest, and the performance of all PAM beamforming algorithms remains stable.

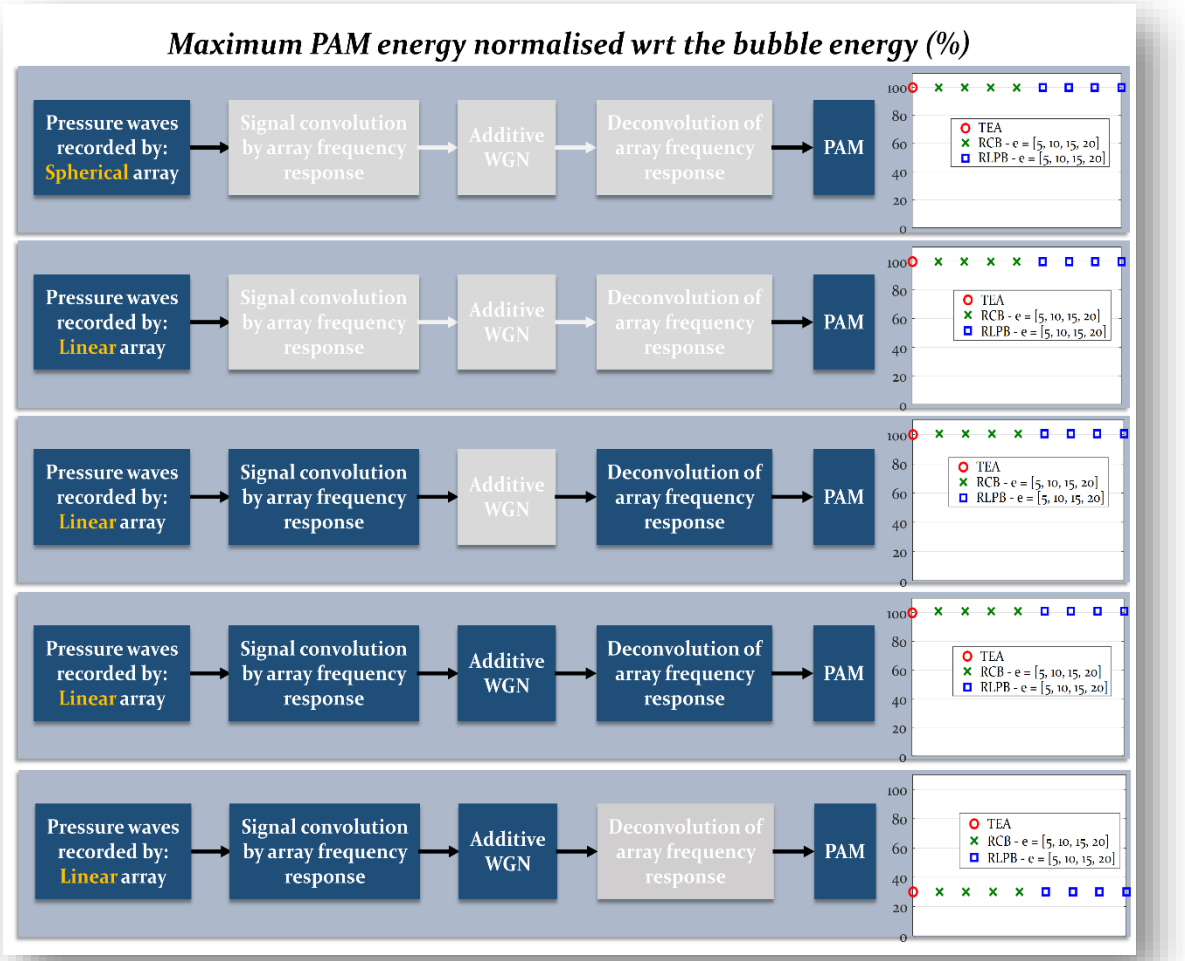


Figure 2.2 Source energy estimation in the case of a single bubble for the three beamforming algorithms, namely TEA, RCB, and RLPB, for different combinations of the signal pathway components presented in each row (Blue rectangles represent components that are included in the process, and grey rectangles the components that have been omitted). In the case of the adaptive beamformers, namely RCB and RLPB, four different values of the ε parameter (ε = 5, 10, 15, 20) have been examined, and they are represented with the same colour-symbol combination for each beamformer (green cross for RCB and blue square for RLPB).

Part II: Source resolvability- Spatial resolution

In the first part of the simulations it has been established that PAM using either of the three contending beamforming techniques is able to accurately and equally recover the source energy of a single bubble, assuming a signal pathway that involves recording acoustic signals from a linear array of limited bandwidth elements, in the

presence of additive noise due to electronics, and deconvolution of the signals with the element impulse response as a processing step prior to PAM.

The next challenge is to investigate the spatial resolution of PAM depending on the choice of the beamforming algorithm. Although the source energy estimated at the location of the source on the PAM map is correct, the energy estimated in adjacent regions, i.e. the blurring of the source, will determine the spatial resolution of the PAM technique. Considering, now, two sources at a certain distance from an array of detectors, the blurring appearing on the PAM maps will determine how close these two sources could be brought but still be resolvable, i.e. the spatial resolution of PAM.

In this second part of the simulations, two single bubbles placed at a fixed distance from a linear array of sensors are gradually brought closer, and the acoustic emissions recorded by the array elements are mapped using PAM based on all three beamformers, i.e. TEA, RCB and RLPB. It is assumed that the linear array elements have limited bandwidth, modelled as in the previous part of simulations, and white Gaussian noise due to the receiving electronics is added to the signal sensed by each element of the array. Deconvolution of the array frequency response is not conducted for a combination of reasons. First of all, in most experimental situations, the exact calibration of each element of the array is not available, and deconvolution is not performed. Secondly, the bandwidth of the array (i.e. 4MHz to 11MHz) specifically excludes the fundamental frequency and the harmonics of the excitation frequency to not cause increased coherence between the emissions of the bubbles, which, apart from the broadband component, contain also the driving frequency. As previously demonstrated (Michalet and Weiss, 2006), source coherence results in degradation of the spatial resolution of PAM, and in this case it has been avoided for the comparison of the spatial resolution provided by each beamforming algorithm. Additionally, in order

to ensure source incoherence, the radius of the second bubble is slightly different compared to the first, making sure, at the same time, that both sources provide comparable levels of acoustic emissions and energy in order to avoid shadowing during PAM. Finally, in this part of the simulation the effect of the ε parameter in the spatial resolution for the two optimal beamformers is evaluated.

The parameters chosen in this part of the simulations for the Keller-Miksis model and the PAM algorithm are summarised in Table 2.2.

Table 2.2 Keller-Miksis model and PAM algorithm parameters for simulation performed to evaluate the spatial resolution of PAM combined with each of the three beamforming algorithms (TEA, RCB, RLPB).

Keller-Miksis model parameters	PAM parameters
$\boldsymbol{R_0 = 3\mu m}$ $\boldsymbol{R_1 = 2.9\mu m}$	$F_s = 25MHz$
$\boldsymbol{f_0 = 0.5MHz}$	$c = 1482m/s$
$\boldsymbol{P_0 = 1MPa}$	$\#\ array\ sensors:\ Linear = 128$
$\boldsymbol{Number\ of\ cycles = 20}$	$\varepsilon = [5\ 10\ 15\ 20]$
$\boldsymbol{Distance\ from\ array = 75mm}$	

According to the theoretical limits of PAM resolution presented in section 1.4.1, for a linear array of aperture approximately 38.4mm, central frequency 6.25MHz, and speed of sound of the medium 1480m/s, the minimum resolvable distance between the two sources is 0.4mm transversely and 6.3mm axially. Therefore, the distances chosen for the assessment of the spatial resolution for all beamformers are 0.2mm, 0.1mm, and

0.08mm for the transverse resolution, and 6mm, 4mm, and 2mm for the axial resolution. The transverse and axial PAM energy profiles respectively for all three beamforming techniques at each distance between the two sources mentioned above are presented in Fig. 2.3.

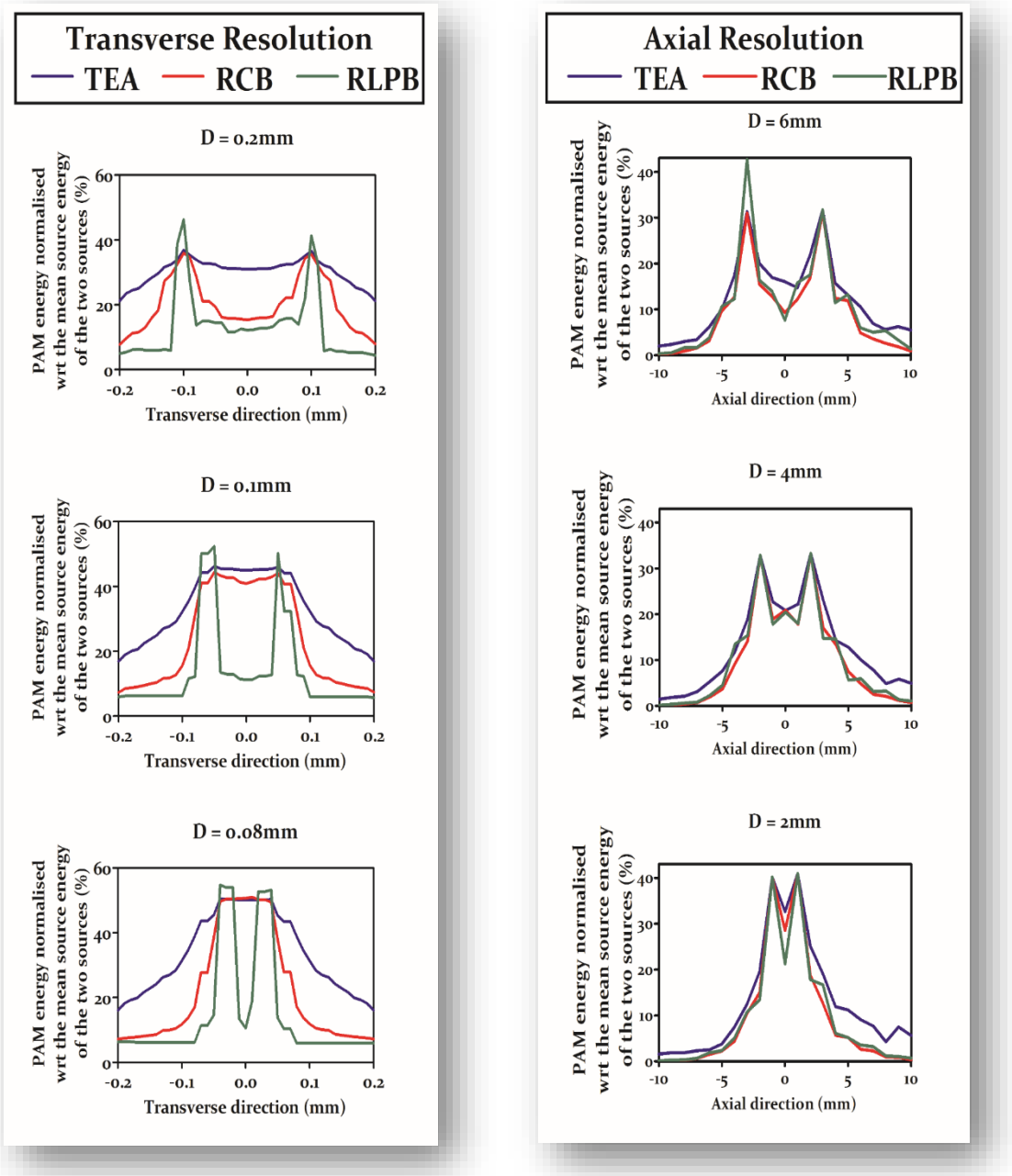


Figure 2.3 Simulation results of the transverse and axial resolution of PAM for the three beamforming algorithms (TEA, RCB, RLPB) for a fixed distance between the sources and the array of elements, as the distance between the two single sources decreases with respect to the theoretical value.

For a source separation distance slightly smaller than the theoretical limit (D=0.2 mm), all three beamformers perform well transversely. Axially, TEA fails to resolve the two sources clearly, whilst RCB and RLPB perform similarly well.

As the axial distance between the two sources decreases, all beamformers seem to be able to resolve the two sources even for the smallest axial distance (2mm) considered, with only marginal improvements for the more advanced beamformers. An explanation for this observation could be the simplicity of the bubble model, which does not account for bubble shielding or multi-bubbles interference. Such interaction would lead to attenuation of the signal originating from the source lying furthest away with respect to the array, and therefore PAM performance degradation.

However, as the transverse distance between the two sources decreases, the spatial resolution achieved by TEA and RCB degrades, with RCB performing better compared to TEA. On the other hand, RLPB outperforms the aforementioned beamforming techniques by consistently providing higher ratio of PAM energy at the source locations relative to the energy reported at the mid-point between the sources, being the only beamformer that enables a clear distinction between two sources 0.08mm apart.

As far as the effect of the ε parameter in the PAM spatial resolution is concerned, there is a need for compromise between the ability to correct for array steering vector mismatches and to suppress interference efficiently. In these simulations, the array element positions are perfectly known, and the performance of the two optimal beamformers that depend on ε should improve as the value of the parameter decreases to achieve higher levels of interference suppression. Fig. 2.4 presents for both axial and transverse direction, the PAM energy profiles of RCB and

RLPB considering different values of ε, namely ε = 5, 10, 15, and 20, at different distances D between the two sources.

It is highly informative to investigate the effect of varying the value of the parameter ε (between 0 and 20) on the mapping of the region between the two sources where interference is greatest. For RCB, as the value of ε increases, the PAM energy in the middle of the two sources increases as well, degrading the spatial resolution of PAM, and this is most obvious in the case of transverse resolution. On the other hand, RLPB is able to maintain a reasonably consistent performance for the range of ε values assessed in this simulation in the axial direction, and offers significant improvements in the transverse direction. This observation suggests that in cases where a large value of ε is required to account for steering vector mismatches, the interference suppression capability of RLPB-PAM will not degrade as much as for RCB-PAM, resulting in improved spatial resolution. In other words, RLPB is considerably more robust to operator and setup errors.

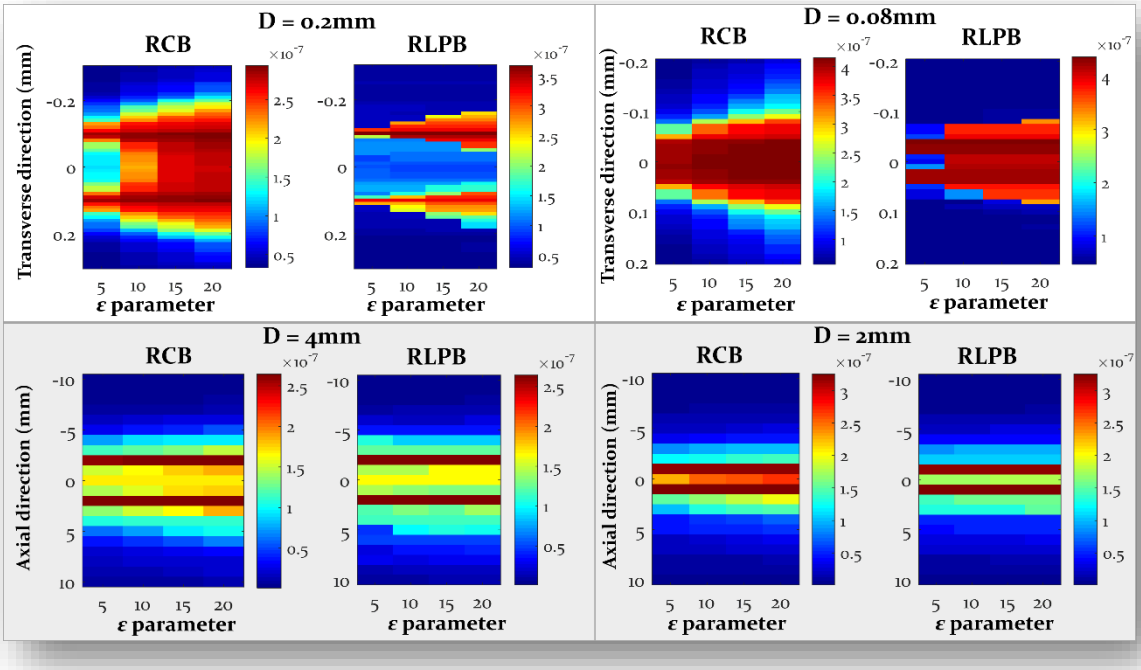


Figure 2.4 Effect of the parameter ε on the axial and transverse PAM resolution in the case of two single sources separated by distance *D*.

The above simulation results suggest that taking into account the HOS of the recorded signals results in improved source resolvability and robustness of PAM with respect to array calibration errors and interfering signals. However, there are several important aspects of spatio-temporal monitoring of acoustic emissions during ultrasound therapies that have not been incorporated in the simulations. First, the interaction occurring between the emissions of the two acoustic sources due to multi-path propagation, especially when the sources are aligned in the axial direction with respect to the array, is expected to alter the profile of the emissions as these propagate towards the array, and has not been modelled in the simulations. Additionally, in experimentally and clinically relevant scenarios, resolvability of two regions of acoustic cavitation is more crucial compared to resolvability of two single sources. A characteristic example could be cavitation-enhanced drug delivery, in which regions of

cavitation activity could be associated with increased drug delivery. Therefore, the ability of PAM to accurately distinguish between regions of acoustic activity originating from multiple sources is of great importance. Finally, the presence of interfaces, and generally, medium variability is expected to impose another challenge on PAM. Speed of sound variations due to changes in the medium through which acoustic waves propagate will deteriorate the time-delaying process, and therefore the time alignment of the recorded signals becomes challenging. Such a situation is expected to be handled more efficiently by adaptive beamforming approaches, which, apart from the adaptive weight calculation, involve also the parameter ε that could account for speed of sound variabilities. To investigate the performance of the two competing beamforming algorithms under such a challenging situation, the *in vitro* experiment described in section 2.4 has been designed and implemented to provide additional insight on the PAM spatial resolution with respect to the beamforming algorithm chosen.

2.4 EXPERIMENTAL METHODS

2.4.1 EXPERIMENTAL RATIONALE

The experimental setup presented in Fig. 2.5 aims to experimentally verify the improvement of the spatial resolution of PAM that was observed in the simulations presented in section 2.3, when the RCB beamforming algorithm is replaced by RLPB. As already mentioned, a two-bubble model is a good starting point in studying the spatial resolution of the proposed system, but it does not capture phenomena that are encountered in clinically relevant conditions. More specifically, it is expected that cavitation shielding, or varying attenuation of the signal-of-interest depending on the relative distance between the sources and the distance from the detectors might occur that could potentially affect the performance of the beamforming technique.

Additionally, acoustic activity due to individual bubbles versus clouds of bubbles modifies the problem significantly. Multi-bubble interactions within a cloud of bubbles affecting their activity, as well as multiple-path propagation and interaction between the emissions of the individually collapsing bubbles is expected to alter significantly the profile of the recorded by the array acoustic emissions, and it may potentially influence the spatial resolution of each of the contending beamforming techniques. The experimental setup presented here attempts to incorporate the above considerations in order to compare the two optimal beamforming algorithms in the context of PAM spatial resolution.

2.4.2 EXPERIMENTAL APPARATUS

A 0.5MHz spherically focused, single-element ultrasound transducer (H107 SN27; Sonic Concepts, Bothell, WA) with active diameter 64mm, focal length 62.4mm, and a central rectangular cut-out of dimensions 13x45mm^2 is placed in a large water tank of degassed, filtered water. The transducer is connected through a matching network to a function generator (33250A 30 MHz function/arbitrary waveform generator, Agilent Technologies, Santa Clara, CA), and it is driven on burst mode (2000-cycles sinusoid signal of burst period 200ms), at its fundamental frequency at 1.3MPa, after amplification by a 55dB power amplifier (E&I A300; Rochester NY).

A Verasonics L11-4v linear array transducer (central frequency 6.25 MHz, 128 elements, pitch 0.298-0.302mm, sensitivity −64.5 to −59.5 dB, elevation focus 15-25 mm, Verasonics, Inc., Redmond, WA) is placed perpendicular to the HIFU transducer and co-aligned with the focus of the HIFU transducer. The multi-element array transducer is connected to the Verasonics Vantage Research Ultrasound System

(Verasonics, Inc., Redmont, WA) that allows passive simultaneous recording of the acoustic signals from all elements on the array, and subsequent processing using a custom-made code to enable generation of PAM maps.

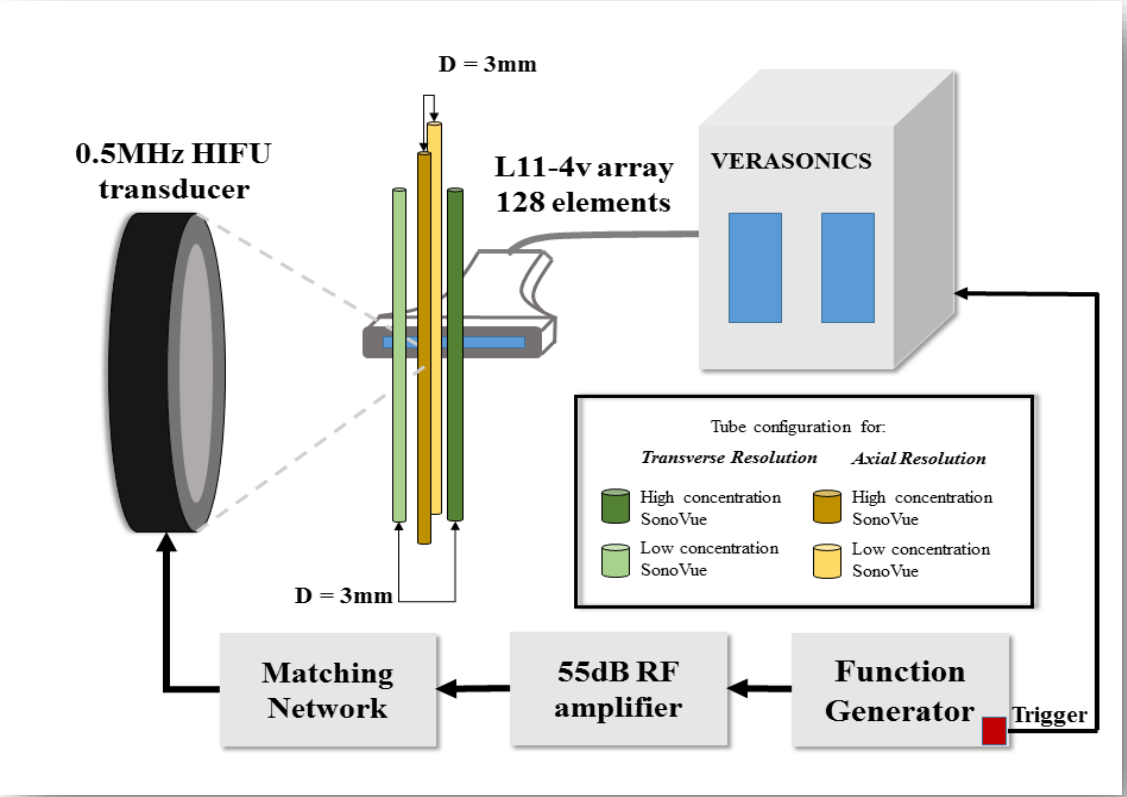


Figure 2.5 Experimental setup involving two pieces of PVC tubing with SonoVue of different concentrations in flow, placed at the focus of a HIFU transducer driven at 0.5MHz. The HIFU transducer is co-aligned with a 4–11 MHz linear array of 128 elements for passive recording of acoustic emissions. These emissions are processed using PAM combined with each of the three beamforming algorithms (TEA, RCB, RLPB) to provide maps of sources of acoustic emissions, and assess the performance of each beamforming algorithm with regards to PAM spatial resolution. The two PVC tubing pieces are placed either on the axial or the transverse direction with respect to the linear array, to assess the transverse and axial PAM resolution respectively.

Two pieces of PVC tubing (Thermo Fisher Scientific ^{TM}) of inner diameter 1mm and outer diameter 2mm are placed on a holder, and positioned at the focus of the HIFU transducer. Two configurations are used regarding the position of the tubes with respect

to the HIFU transducer and the linear array in order to test both the axial and the transverse resolution of PAM. For the axial resolution, the tubes are placed along the transverse axis of the HIFU transducer (tubes coloured with yellow shading in Fig. 2.5), and for the transverse resolution, they are placed along the axial axis of the HIFU transducer (tubes coloured with green shading in Fig. 2.5). The relative distance between the tubes, and a schematic of the cross-section of the tubes describing the expected distance between the two cavitation regions is presented in Fig. 2.6. Using a syringe pump for each tube, SonoVue microbubbles (SV; Bracco Spa, Milan, ITA) flow through the tubes at a constant rate, acting as cavitation nuclei.

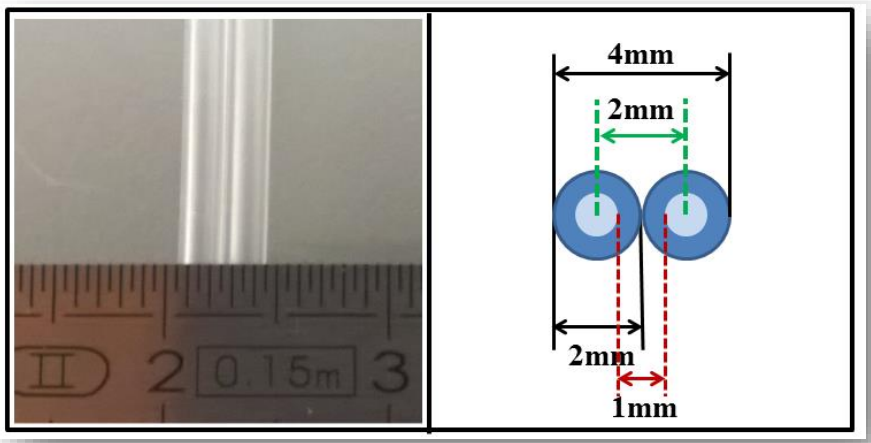


Figure 2.6 Two PVC tubing pieces configuration. On the left, a picture of the two tubing parts as they are attached on the holder is displayed, and on the right a schematic of the cross-section of the two tubing parts is presented demonstrating the tubing dimensions and the relative distances between the different parts and walls of the tubing.

Table 2.3 In-vitro experimental parameters for the assessment of PAM spatial resolution using the experimental setup from Fig. 2.5

Experimental Parameters	
Driving Frequency	0.5MHz
Pressure Amplitude	~1.3MPa (peak negative)
Pulse duration	4ms – 2000 cycles
Burst repetition period	200ms
Duty cycle	2%
SonoVue Dilution	***Axial Resolution***: Front channel* = 2ml/L Back channel* = 40ml/L ***Transverse Resolution***: Front channel** = 40ml/L Back channel** = 40ml/L
Flow rate	***Axial Resolution***: Front channel* = 0.4ml/min Back channel* = 0.2ml/min ***Transverse Resolution***: Front channel** = 0.3ml/min Back channel** = 0.4ml/min
Number of SonoVue bubbles in the focal region, in one tube	***For 2ml/L concentration:*** ~1600 ***For 40ml/L concentration:*** ~33000
Percentage of replenished SonoVue bubbles in the focal region in one tube at each burst period	***For 0.4ml/min flow rate:*** ~56% ***For 0.3ml/min flow rate:*** ~42% ***For 0.2ml/min flow rate:*** ~28%
Distance between middle of tubes and array	***Axial Resolution***: 15mm – 28mm ***Transverse Resolution***: 225mm – 300mm

*** with respect to the imaging array**

**** with respect to the HIFU transducer**

2.5 SIGNAL PROCESSING

The recording of the acoustic emissions by all the elements of the linear array is synchronised with the HIFU exposure by triggering the Verasonics Vantage data acquisition system. The sampling frequency dictated by the system was four times the central frequency of the linear array (6.25MHz), i.e. 25MHz. At a frame rate of 1Hz, the RF signals are transferred to the memory of the computer and processed using a real-time implementation of RCB-PAM based on a combination of GPU and CPU programming to provide a real-time PAM map and guide the experiment.

2.5.1 EXPERIMENTAL PROCEDURE

As discussed in section 1.4.1 the resolution of PAM is dictated by the diffraction limits of the passive array given its geometry and bandwidth. The parameter that affects the resolvability, assuming a linear array of central frequency 6.25MHz and aperture approximately 38.4mm in this case, is the distance between the sources and the array for a given array aperture. More specifically, for a fixed distance between the two sources and the linear array, there is a lower limit in the source separation below which they can no longer be distinguished. Changes in the resolution limits due to the application of different beamforming techniques in PAM could be assessed either by keeping the array-to-source distance fixed and altering the source separation, or keeping the source separation fixed and altering the array-to-source distance. The second approach has been used here as it is considerably more practical to implement experimentally.

Following alignment of all the components in the setup, the array was initially moved as close as needed to the two pieces of tubing to enable clear separation of the

two sources using the real-time implementation of the RCB beamformer. This process was repeated both for axial and transverse source separation arrangements, yielding a different initial distance for each configuration.

Adjustments to the concentration of SonoVue flowing through each of the tubes and to the flow rate in each tube were required for both axial and transverse resolution setup configurations. More specifically, in the case of the axial resolution experiments, the emissions from the tube positioned further away with respect to the linear array were highly attenuated as they propagated through the multiple tubing interfaces. Therefore, a higher concentration of SonoVue (Table 2.3) was flown through the distal tube compared to the proximal tube, in order to ensure comparable levels of acoustic emissions due to inertial cavitation being recorded by the elements of the array. Additionally, the optimal flow rate for each tube was defined dynamically to ensure that cavitation occurs simultaneously in both tubes for the majority of the pulses, and it is of comparable level. For this purpose, at the beginning of the experiment at the closest distance between the tubes and the array, real-time PAM maps using RCB were generated, and the flow rate in both tubes was adjusted dynamically.

A similar optimization procedure was followed for the case of the transverse resolution. Since the acoustic emissions originating from each tube propagate through the same layers of tubing towards the array, no adjustment in the concentration of SonoVue in each tube was necessary. There is a set of limitations associated with this configuration. First, the position of each of the tubes with respect to the focal region of the HIFU transducer might cause a small difference in focal pressure applied in each of the tubes. Such a variation was addressed by adjusting in real-time the flow rate using the feedback from the PAM-RCB maps, as described before. Adjusting the flow rate, i.e. the availability of replenished cavitation nuclei at the focal region in each tube, it is

expected to compensate for the difference in pressure amplitude between the two tubes. Secondly, a sensitivity variation among the elements of the array is expected, as one of the sides of the array is slightly closer to the tubes. Such a variation could be addressed in the future by varying the concentration of SonoVue in each tube.

As soon as the flow rates were established, data collection began. Starting from an initial position with the array closest to the tubes, the array was gradually moved further away in steps of 1mm using an automated positioning system, and data was recorded continuously.

2.5.2 PASSIVE BEAMFORMING

Post-processing of the recorded RF lines involves the generation of PAM maps for each set of data using either RCB or RLPB. Prior to beamforming, the recorded signals are time-windowed, corresponding to 80μs time of recording, and then filtered using a custom high-pass filter implemented in MATLAB with a cut-off frequency at 1.2MHz to eliminate the first two harmonics observed in the spectrum of the recorded signal. Therefore, the remaining signal consists only of broadband noise due to inertial cavitation and it is fed in the PAM algorithm.

Finally, as already discussed, the parameter that affects the performance of both optimal beamforming algorithms, RCB and RLPB, is ε. However, it is not in the scope of the present *in vitro* experiment to investigate the effect of this parameter on the performance of the two competing beamforming approaches. Instead, a value for ε, common throughout the experiment, has been selected for each beamformer based on the data collected at the optimal, i.e. smallest, distance between the sources and the array. The parameter was allowed to take values between 5 and 25 in steps of 5, and the

criteria for choosing the optimal value were, first, correct localisation of the sources, i.e. sources to be mapped inside the tubes, and secondly, estimation of the size of the cavitation regions to be as close as possible to the actual size of the region in which cavitation is expected to take place, i.e. the size of the tubes. The optimal value of ε extracted from this process for both beamforming techniques was 10.

2.6 EXPERIMENTAL RESULTS

2.6.1 AXIAL RESOLUTION

Fig. 2.7 shows the PAM maps generated using RCB and RLPB for two cavitating regions, bound by the two pieces of tubing, positioned axially at six different distances *D* from the array and at a fixed separation from each other. The distance *D* is defined as the distance between the middle point of the two maximum PAM energies calculated for the two cavitating regions and the middle element of the array. This is an approximate calculation since we are primarily interested in the relative comparison of the spatial resolution provided by the two methods, and not an accurate definition of the spatial resolution limits of the two beamforming techniques, which is expected to be highly dependent on the experimental conditions.

To quantify resolvability of the two regions of cavitation activity, a quantitative measure had to be adopted. For this purpose, Rayleigh's criterion for the diffraction limit to resolution (Lord Rayleigh F.R.S., 1879), which specifies the minimum separation angle between two light sources in order to be resolved as two distinct objects, has been used (Michalet and Weiss, 2006) and in practice it requires the level of the dip between the two source regions to be at least 26.3% with respect to the

energy at the source. In our case, since the energy in the two regions is not always equal, this criterion is defined with respect to the region that demonstrates the lowest PAM energy. Calculation of the dip for each PAM map presented in Fig. 2.7 for both beamforming algorithms is displayed on Fig. 2.8. The black lines on Fig. 2.7 represent the approximate mid-line through the cross-section of the tubes, as determined by B-mode imaging during initial alignment. An axial profile of the PAM map is traced along this line and used to determine PAM source resolvability, as represented in Fig. 2.8.

In Fig. 2.7, the PAM maps formed using either RCB and RLPB are presented for distances *D* varying between 15.5mm and 27.5mm. In the case of RCB, distinguishing the two cavitation regions becomes more challenging with increasing array-to-source distance. Beyond D = 24.5mm, the PAM energy in the region between the two sources, where cavitation is not expected, increases significantly, resulting in gradual merging of the two regions into one. On the other hand, RLPB is able to maintain resolvability of the two source regions up to D = 27.5mm.

By observing the colour maps for each distance in Fig. 2.7, it is concluded that the maximum source energy estimated through each optimisation process is comparable. More specifically, the maximum source energy estimated by RLPB is between 70% and 85% of the corresponding energy estimated by RCB for all pairs of maps in this figure. Therefore, the key difference between the two beamforming algorithms is the ability to suppress the interference between the two source regions, as discussed in section 2.3.

This observation can be further supported by observing the elongation in the axial direction of the cavitation regions in Fig. 2.7. Although the size of each cavitation region is limited to 1mm, as can be calculated from Fig. 2.6, in RCB this size seems to be exceeded compared to RLPB. This results in overlap of the two source regions and

limits resolvability. The combination of the point spread function of each beamforming algorithm, and the ability of each beamformer to deal with multi-source interference (Coviello et al., 2015) is potentially the reason behind the different elongation observed between the two beamforming algorithms.

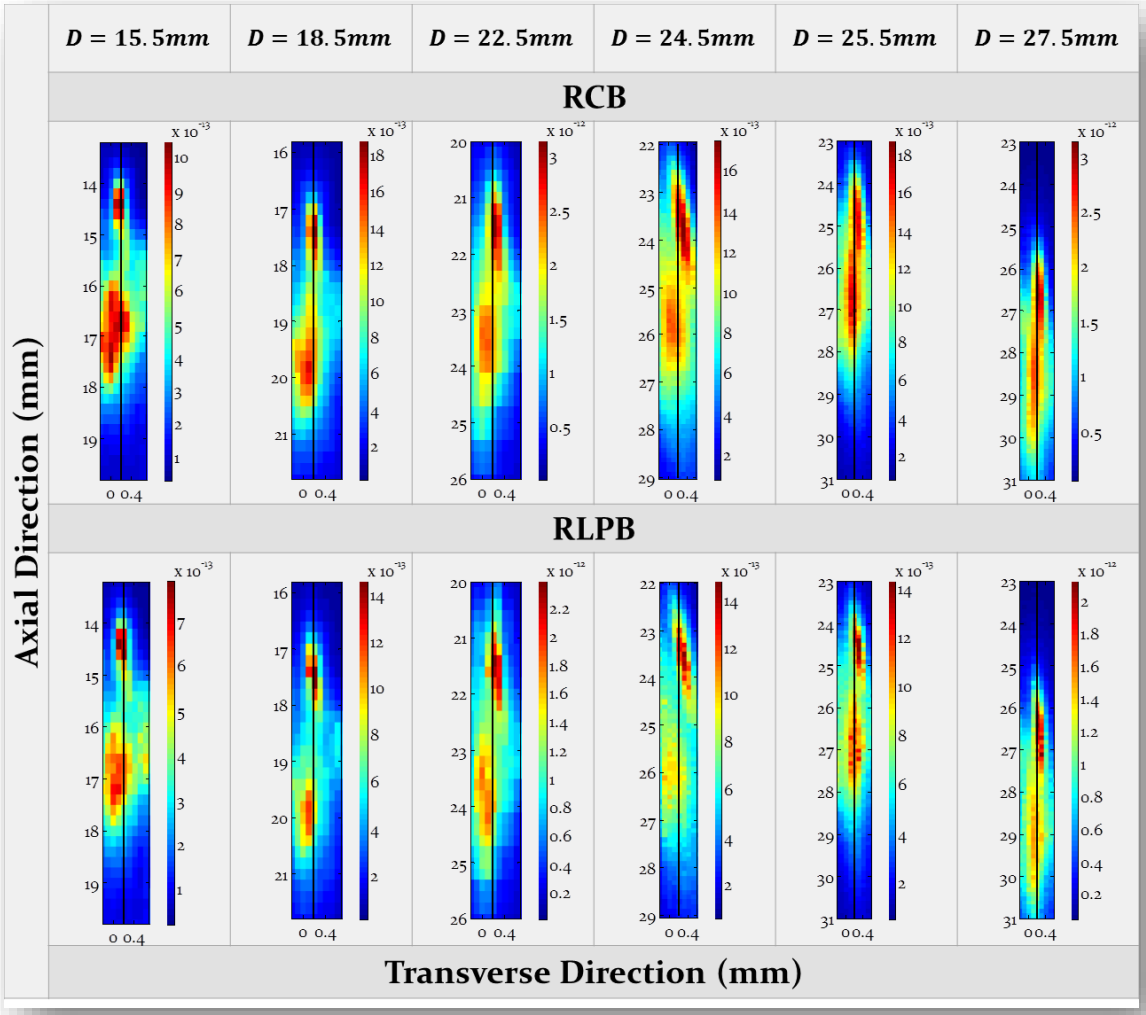


Figure 2.7 PAM maps corresponding to the two optimal beamforming algorithms, i.e. RCB and RLPB, for different distances between the two PVC tubing pieces and the linear array, varying between approximately 15.5mm and 27.5mm. The tubing parts are placed along the axial direction of the array in order to assess the axial resolution of PAM with respect to the beamforming algorithm applied.

Analysis of the axial line profiles on the PAM maps, shown in Fig. 2.8, provides an approximation of the resolution limits achieved by the beamforming algorithms. It is observed that for RCB, Rayleigh's criterion for resolvability is no longer satisfied at a distance of 22.5mm between the sources and the array. On the other hand, this limit is much higher in the case of RLPB, namely 27.5mm, constituting an increase in PAM axial resolution of approximately 22%.

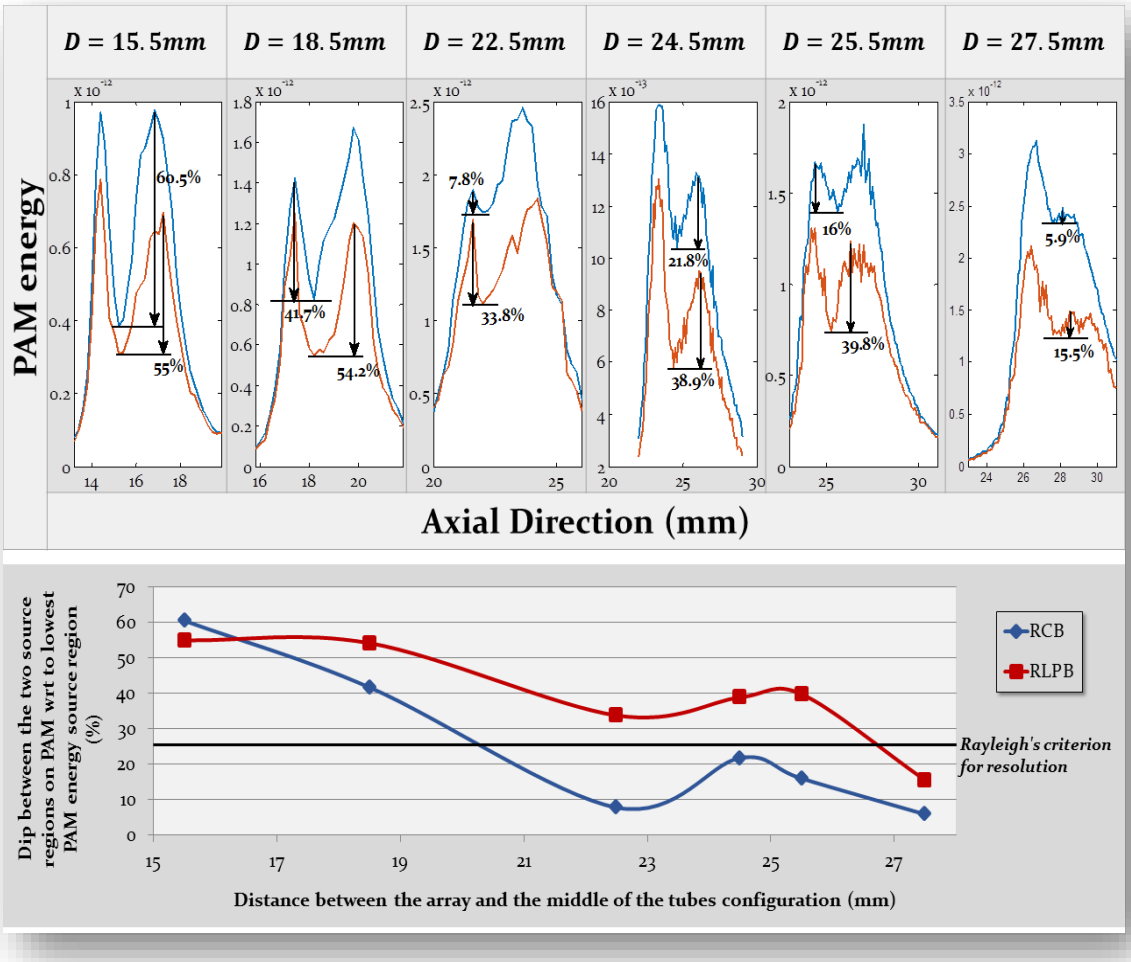


Figure 2.8 PAM source region resolvability analysis in the axial direction based on Rayleigh's criterion that requires the level of the dip between the two regions to exceed 26.3% of the level of the source region energy. The dip is calculated in each case with respect to the source region with the lowest PAM energy, and it is displayed with black arrows for both RCB (blue line) and RLPB (red line). In the lower part of the graph the dip is plotted with respect to the distance between the array and the middle of the tubing configuration. The threshold according to Rayleigh's criterion in order for the two source regions to be resolvable is displayed with a black line, and results above this line indicate successful resolvability.

2.6.2 TRANSVERSE RESOLUTION

The same approach is applied to analyse the results in the context of transverse positioning of the sources with respect to the array, with the distance *D* still representing the source-to-array distance (Fig. 2.9). Transverse profiles evidencing the percent decrease between source energy and off-target energy are further presented in Fig. 2.10.

On an observation basis (Fig. 2.9) RCB can visually separate the two cavitation regions until the distance of 245mm, while RLPB is still capable of distinguishing the two regions even at 299mm from the array. After applying Rayleigh's criterion for resolvability (Fig. 2.10), it is observed that the above limits become stricter. More specifically, RCB fails to satisfy the resolution criterion at all distances presented in the figure, while in the case of RLPB the distance at which the criterion is no longer satisfied is 259mm.

Another important observation from Fig. 2.9 is the increase of the size of the cavitation region in the axial direction as the distance from the array increases, and the difference in this elongation between RCB and RLPB. As already discussed during the analysis of the axial resolution, the difference in the elongation of the cavitation region is the reason for the decreased axial resolution of RCB compared to RLPB. The results shown in Fig. 2.9 enhance this conclusion, as they evidence the elongation of each source region even in the absence of another cavitating region in front or behind it. It is therefore the combination of the point spread function of the individual sources and the ability to resolve interactions between sources that yield the very different spatial spread observed between RCB and RLPB.

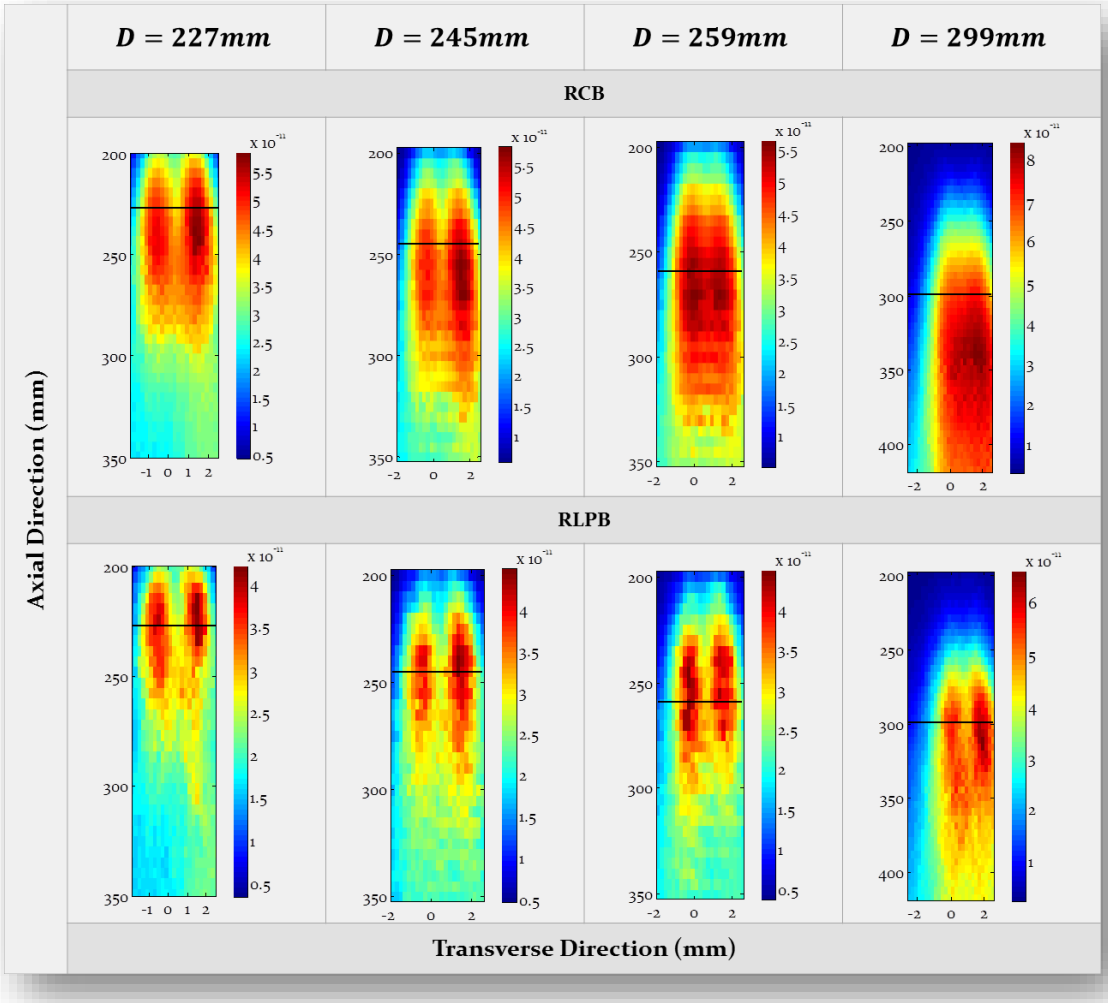


Figure 2.9 PAM maps corresponding to the two optimal beamforming algorithms, i.e. RCB and RLPB, for different distances between the two PVC tubing pieces and the linear array, varying between 227mm and 299mm. The tubing parts are placed along the transverse direction of the array in order to assess the transverse resolution of PAM with respect to the beamforming algorithm applied.

Looking more closely at the transverse line profiles in Fig. 2.10, it is once again clear that the elongation in the axial direction due to the large distance between the tubes and the array does not allow correct localisation of the tubes. The distance *D* is verified in this case by the arrival time on the array elements of the reflection of the incident wave (at the driving frequency) from the proximal to the HIFU transducer tube wall. At this point it would be interesting to point out that the location of the maximum

on the PAM maps corresponding to RLPB better estimates the tube location compared to RCB.

Analysis of the line profiles on the PAM maps, shown in Fig. 2.10, provides again an approximation of the resolution limits for the two beamforming algorithms. More precisely, it is observed that for RCB, Rayleigh's criterion for resolvability is no longer satisfied at a distance of 227mm between the sources and the array. On the other hand, this limit is much higher in the case of RLPB, namely 259mm, constituting an increase in PAM axial resolution of approximately 14%.

Considering the worst-case scenario of sources cavitating adjacent to the two proximal tubing walls, (yielding a source-to-source distance of 1mm), the maximum distance from the array for which the regions are theoretically resolvable is approximately 30mm for the axial source arrangement and 180mm for the transverse source arrangement. Therefore, the axial resolution of RLPB approaches the theoretical resolution limit, while the theoretical transverse resolution limit has been surpassed by both beamforming algorithms.

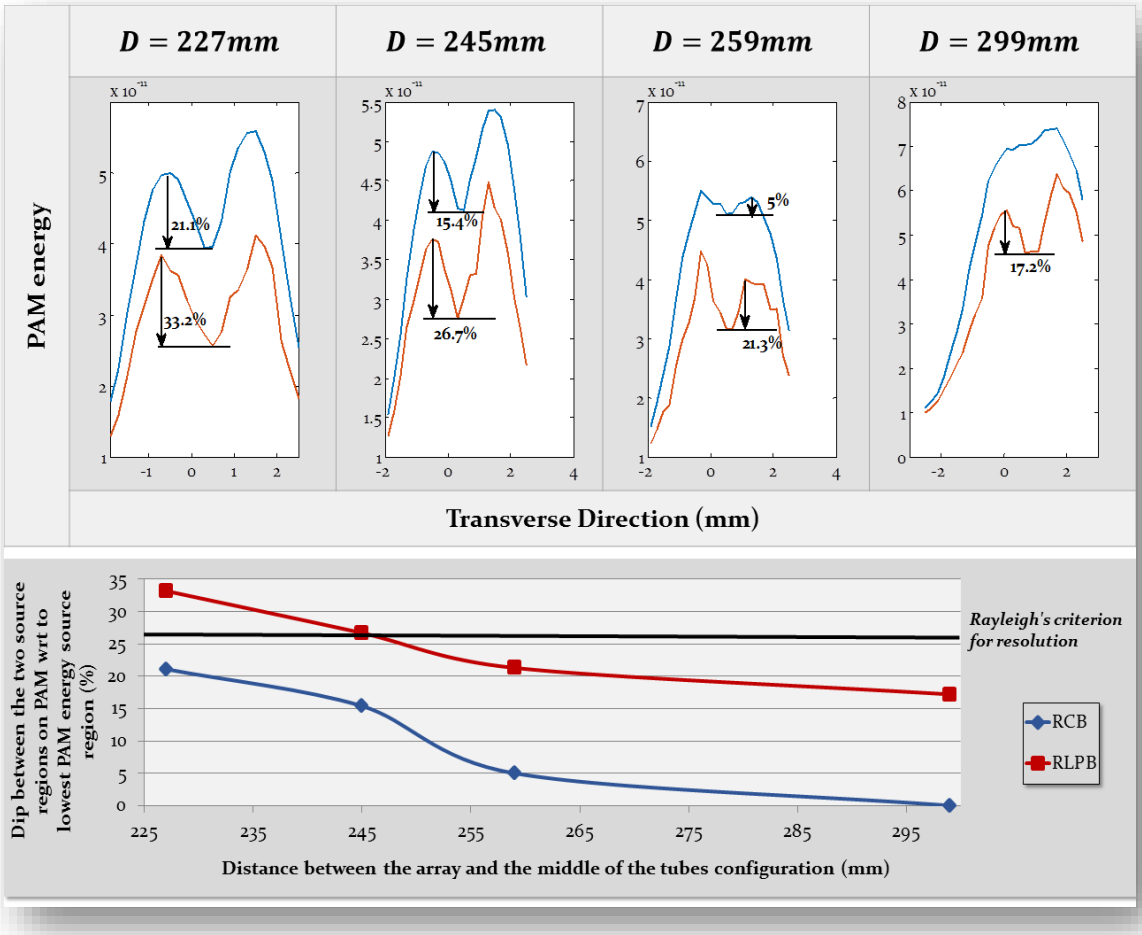


Figure 2.10 PAM source region resolvability analysis in the transverse direction based on Rayleigh's criterion that requires the level of the dip between the two regions to exceed 26.3% of the level of the source region energy. The dip is calculated in each case with respect to the source region with the lowest PAM energy, and it is displayed with black arrows for both RCB (blue line) and RLPB (red line). In the lower part of the graph the dip is plotted with respect to the distance between the array and the middle of the tubing configuration. The threshold according to Rayleigh's criterion in order for the two source regions to be resolvable is displayed with a black line, and results above this line indicate successful resolvability.

2.7 CONCLUSIONS

A novel optimal passive array beamforming algorithm has been proposed in this chapter that exploits the HOS of the acoustic signals passively received during therapy to improve the spatial resolution of the PAM method. By minimising the l_∞-norm of the array output, RLPB is able to take into account information that is hidden in the higher order moments of the array signals. Both simulations and *in vitro* experimentation demonstrated the ability of RLPB to outperform the currently available beamforming algorithms for PAM.

According to our simulations, the proposed beamforming algorithm is able to correctly estimate the source energy from a single bubble regardless of the array geometry or the presence of additive Gaussian noise from the electronics of the data acquisition system. However, the finite bandwidth of the array elements degrades the received signal, and results in a calculated source energy that is only a portion of the actual energy. In order for PAM to be able to completely recover the pressure signals impinging on the array elements, an accurate calibration of each array element is required, which is experimentally difficult to acquire. In the case of an approximate calibration being available, more sophisticated deconvolution techniques need to be applied to recover the original acoustic signals as effectively as possible.

In terms of spatial resolution, our numerical simulations demonstrated that RLPB outperforms TEA and RCB, providing significantly improved PAM transverse and axial resolution. More specifically, in the transverse direction the minimum distance between two sources in order to be resolvable by RLPB is more than half compared to RCB. In the axial direction, clear distinction of the two sources is achieved by both RCB and RLPB, with the PAM energy in the valley between the two sources in the case

of RLPB being almost half the corresponding energy for RCB. An additional advantage of the RLPB algorithm was found to be its robustness to variations in the optimization parameter ε and to errors in array positioning or sensitivity. This feature significantly enhances performance for *in vivo* applications.

In vitro experimentation subsequently enabled us to verify the relative spatial resolutions achieved using RCB and RLPB, under more clinically relevant conditions where multiple sources of cavitation are present, and regions of cavitation need to be resolved. The results acquired demonstrate improved performance of RLPB PAM compared to RCB, providing a 22% improvement in the axial, and a 14% enhancement in the transverse PAM resolution. The resolution improvement is believed to originate from the combination of narrower point spread function for a single source, as the simulation results suggest, with better suppression of interfering signals from multiple sources.

Application of the proposed method *in vivo* is expected to provide improved spatial resolution and facilitate spatial correlation between acoustic activity and anticipated bioeffects. A significant parameter that needs to be taken into consideration in the transition from *in vitro* to *in vivo* application of RLPB-PAM is the presence of multiple tissue layers in the acoustic propagation path. This would result in phase changes in the propagating signals that could be addressed by considering the weights in RLPB as complex numbers. Such a modification in the context of HOS is expected to further improve the performance, but also increase the computational complexity of the beamforming algorithm under more clinically relevant conditions.

Comparing now the computational complexity of RCB and RLPB, the most computationally expensive part in the discussed beamformers is eigen-decomposition of

the covariance matrix in RCB, and solving the linear programming problem in RLPB. As already mentioned, interior-point-method and its variations provide accurate solutions to large-scale linear programming problems, and they can run in polynomial time with respect to the number of input variables (Karmarkar, 1984). Since it is an iterative algorithm, parallelisation is not facilitated, and the same applies to eigen-decomposition. However, the use of optimised commercially available software along with parallelisation of other components in the PAM pipeline could potentially provide real-time performance in the context of PAM using either of the two beamformers.

In conclusion, it is anticipated that the proposed beamforming algorithm will significantly improve the spatial resolution of PAM, allowing statistical information in the HOS of the acoustic signals to be exploited. The demonstrated improvement in the PAM resolution brings PAM a step closer to its clinical adoption, allowing the application of the method in ultrasound therapies where the targeted region is deeper inside the body, e.g. the spine, or when regions of acoustic activity to be resolved are very close to each other, as is the case in drug delivery where cavitation outside the vasculature needs to be identified and correlated with drug extravasation.

2.8 REFERENCES

Bronzino, J.D., 2000. The Biomedical Engineering Handbook 1. Springer Science & Business Media.

Cardoso, J.F., 1989. Source separation using higher order moments, in: , 1989 International Conference on Acoustics, Speech, and Signal Processing, 1989. ICASSP-89. Presented at the , 1989 International Conference on Acoustics, Speech, and Signal Processing, 1989. ICASSP-89, pp. 2109–2112 vol.4.

Cardoso, J.F., Souloumiac, A., 1993. Blind beamforming for non-Gaussian signals. IEE Proc. F - Radar Signal Process. 140, 362–370.

Chua, K.C., Chandran, V., Acharya, U.R., Lim, C.M., 2010. Application of higher order statistics/spectra in biomedical signals--a review. Med. Eng. Phys. 32, 679–689.

Collin, J.R.T., Coussios, C.C., 2011. Quantitative observations of cavitation activity in a viscoelastic medium. J. Acoust. Soc. Am. 130, 3289–3296.

Coviello, C., Kozick, R., Choi, J., Gyöngy, M., Jensen, C., Smith, P.P., Coussios, C.-C., 2015. Passive acoustic mapping utilizing optimal beamforming in ultrasound therapy monitoring. J. Acoust. Soc. Am. 137, 2573–2585.

Jiang, X., Zeng, W.J., Yasotharan, A., So, H.C., Kirubarajan, T., 2014. Robust Beamforming by Linear Programming. IEEE Trans. Signal Process. 62, 1834–1849.

Karmarkar, N., 1984. A New Polynomial-time Algorithm for Linear Programming, in: Proceedings of the Sixteenth Annual ACM Symposium on Theory of Computing, STOC '84. ACM, New York, NY, USA, pp. 302–311.

Keller, J.B., Miksis, M., 1980. Bubble oscillations of large amplitude. J. Acoust. Soc. Am. 68, 628–633.

Kumatani, K., McDonough, J., Klakow, D., Garner, P.N., Li, W., 2008. Adaptive Beamforming with a Maximum Negentropy Criterion, in: Hands-Free Speech Communication and Microphone Arrays, 2008. HSCMA 2008. Presented at the Hands-Free Speech Communication and Microphone Arrays, 2008. HSCMA 2008, pp. 180–183.

Kumatani, K., McDonough, J., Rauch, B., Garner, P.N., Li, W., Dines, J., 2013. Maximum Kurtosis Beamforming with the Generalized Sidelobe Canceller. ResearchGate.

Kumatani, K., Rauch, B., McDonough, J., Klakow, D., 2010. Maximum negentropy beamforming using complex generalized Gaussian distribution model, in: 2010 Conference Record of the Forty Fourth Asilomar Conference on Signals, Systems and Computers. Presented at the 2010 Conference Record of the Forty Fourth Asilomar Conference on Signals, Systems and Computers, pp. 1420–1424.

Kwan, J.J., Graham, S., Myers, R., Carlisle, R., Stride, E., Coussios, C.C., 2015. Ultrasound-induced inertial cavitation from gas-stabilizing nanoparticles. Phys. Rev. E 92, 23019.

Lord Rayleigh F.R.S., 1879. XXXI. Investigations in optics, with special reference to the spectroscope. Philos. Mag. Ser. 5 8, 261–274.

Mendel, J.M., 1991. Tutorial on higher-order statistics (spectra) in signal processing and system theory: theoretical results and some applications. Proc. IEEE 79, 278–305.

Michalet, X., Weiss, S., 2006. Using photon statistics to boost microscopy resolution. Proc. Natl. Acad. Sci. U. S. A. 103, 4797–4798.

Nandi, A., 2013. Blind Estimation Using Higher-Order Statistics. Springer Science & Business Media.

Nocedal, J., Wright, S., 2006. Numerical Optimization. Springer Science & Business Media.

Shamsunder, S., Giannakis, G.B., 1991. Wideband source modeling and localization: a HOS-based approach. Presented at the 1991 Conference Record of the Twenty-Fifth Asilomar Conference on Signals, Systems and Computers, 1991, pp. 383–387 vol.1.

Thi, H.-L.N., Jutten, C., 1995. Blind source separation for convolutive mixtures. Signal Process. 45, 209–229.

Tong, S., Thakor, N.V., 2009. Quantitative EEG Analysis Methods and Clinical Applications. Artech House.

Vogel, A., Lauterborn, W., Timm, R., 1989. Optical and acoustic investigations of the dynamics of laser-produced cavitation bubbles near a solid boundary. J. Fluid Mech. 206, 299–338.

Webb, I.R., Payne, S.J., Coussios, C.-C., 2011. The effect of temperature and viscoelasticity on cavitation dynamics during ultrasonic ablation. J. Acoust. Soc. Am. 130, 3458–3466.

Yoshizawa, S., Sugiyama, K., Matsumoto, Y., 2001. Acoustic Emission from Micro Bubbles in Ultrasound Field.

Zhang, Y., 1995. Solving large-scale linear programs by interior-point methods under the Matlab Environment: Optimization Methods and Software: Vol 10, No 1 (No. TR96-01). Department of Mathematics and Statistics, University of Maryland, Baltimore County, Baltimore, MD.

CHAPTER

3

SUM-OF-HARMONICS METHOD FOR IMPROVED NARROWBAND AND BROADBAND SIGNAL QUANTIFICATION DURING PASSIVE MONITORING OF ULTRASOUND THERAPIES

3.1 INTRODUCTION

One of the main challenges of passive acoustic mapping is the accurate separation of the signal of interest from interfering signals that are simultaneously recorded by each element of the array. Clinically available ultrasound transmitters and receivers may have overlapping bandwidths, allowing the simultaneous recording of broadband, as well as narrowband emissions that are harmonics, sub- or super-harmonics of the driving frequency of the therapeutic pulse. These broadband and narrowband emissions are associated with different types of acoustic sources. Narrowband emissions are due to nonlinear propagation and scattering of the incident field, non-inertial cavitation, or scattering of the incident field from boiling bubbles. On the other hand, inertial cavitation gives rise to broadband emissions. The results

presented in this chapter have been presented at the 169th meeting of the Acoustical Society of America (Lyka et al., 2015) and published in the Journal of the Acoustical Society of America (Lyka et al., 2016).

Depending on the application, the signal of interest may either be the narrowband or the broadband component, and its magnitude relative to the interfering component may be significantly greater or smaller. In some cases it is also important to separately map the evolution of sources of narrowband and broadband emissions over the course of the treatment in order to identify the progression and impact of different physical phenomena on the progress of the treatment (Jensen et al., 2012). Therefore, it is of great importance to robustly distinguish broadband and narrowband emissions and accurately quantify the energy in each of these bands.

An important aspect of the problem is that the relative magnitude of narrowband to broadband emissions varies significantly depending on conditions such as the amplitude of the transmitted signal, the degree of tissue nonlinearity, the distance travelled by the transmitted acoustic wave until it is recorded, and the bandwidth of the receiver relative to the frequency of the transmitter. Therefore, an adaptive filtering method is required to accurately distinguish the frequency band of interest regardless of the relative magnitude of the simultaneously recorded interfering signal. The most common experimentally used method is filtering in the frequency domain using a pre-defined comb filter (Choi and Coussios, 2012). However, the accuracy of this technique cannot be guaranteed due to the fixed characteristics (i.e., order, bandwidth, dB rejection, window function) of the comb filter. As the amplitude of the narrowband components of the signal that the comb filter aims to reject varies over time and across applications, the comb filter is unable to perform an equal rejection rate in the cases of lower and higher amplitude. More precisely, as the amplitude of a narrowband signal

increases, a spreading of its energy is observed in the signal spectrum. Therefore, application of the same comb filter in different amplitude narrowband signals will result in partial removal of the energy of the narrowband signal, and thus distortion of the broadband component and misinterpretation of the broadband energy. The importance of acoustic signal filtration for the accurate quantification of the signal-of-interest has recently motivated several research groups. Two methods reported in the literature and demonstrating promising results are singular value decomposition (SVD) (Chitnis et al., 2015) and the discrete wavelet transform (Haqshenas and Saffari, 2015). The first one is based on the spectral signature of the eigenvectors calculated from the SVD analysis of beamformed radio frequency (RF) data, while the second one decomposes the signal in its frequency components by applying a series of filters with different cut-off frequencies at different scales. An alternative method is proposed in this chapter which is based on a time-domain data-adaptive parametric model for estimation of the narrowband component in a recorded signal, in the presence of interference and noise. The broadband component can be subsequently estimated by coherently subtracting the previously estimated narrowband signal from the recorded signal. This method allows estimation of all the components of the received signal, in contrast to comb filtering, which rejects the narrowband components to estimate the broadband one. A similar method has been used in modelling electrocardiograms as time-varying harmonic signals allowing the recovery of surface electromyographic signals (Zivanovic and Gonzalez-Izal, 2012).

3.2 THEORY

3.2.1 INITIAL SUM-OF-HARMONICS (SOH) MODEL

As already mentioned, the channel data, i.e. the signals recorded passively by one or multiple sensors on an ultrasound array, are filtered as an initial signal processing step in order to distinguish the broadband and narrowband components. Assuming that the signal recorded by one sensor is *y*, it could be expressed as the sum of a broadband signal *b* and a harmonic (narrowband) signal *h* at each time sample *n*:

$$y[n] = h[n] + b[n] \Leftrightarrow Y = H + B \tag{3.1}$$

The vectors $\boldsymbol{Y}$, $\boldsymbol{H}$, and $\boldsymbol{B}$ contain the set of samples in a block of data with *N* samples.

Estimation of the harmonic component *h* will enable the estimation of the corresponding broadband component by coherently subtracting the harmonic component from the recorded signal.

$$b[n] = y[n] - h[n] \tag{3.2}$$

The broadband component is assumed to be white Gaussian noise, and the harmonic component is given by a deterministic parametric model. Assuming stationarity, the harmonic component is modeled as a periodic signal consisting of a number *q* of sinusoidal harmonics (Whipps, 2003):

$$h[n] = \sum_{k=1}^{q} a_k \cos(k\omega_0 n + \varphi_k) = \sum_{k=1}^{q} u_k \cos(k\omega_0 n) + v_k \sin(k\omega_0 n) \Leftrightarrow$$
$$\Leftrightarrow \boldsymbol{H} = \boldsymbol{C}_q(\omega_0)\boldsymbol{u} + \boldsymbol{S}_q(\omega_0)\boldsymbol{v} \Leftrightarrow \boldsymbol{H} = \boldsymbol{W}_q(\omega_0)\boldsymbol{x} \tag{3.3}$$

where $\omega_0=2\pi f_0 T$ is the driving frequency of the system and therefore the fundamental frequency of the narrowband component of the recorded signal, T is the sampling period, n represents the time sample of the signal, a_i and φ_i are the amplitude and phase of the ith harmonic, and u_i and v_i are the corresponding Cartesian amplitudes. The variable k that varies between 1 and q represents the number of narrowband components present in the received signal to be estimated by the model. In the case where only the harmonics of the driving frequency are to be estimated, k varies between 1 and q with an integer step equal to 1. However, fractional steps can also be used to estimate sub- and ultra-harmonics of the driving frequency. The second line in (3.3) is a matrix-vector formulation that is equivalent to the first line for a finite block of data with N samples, and the vector $\boldsymbol{x}$ is a concatenation of the vectors $\boldsymbol{u}$ and $\boldsymbol{v}$. The matrix $\boldsymbol{W}_q(\omega_0)$ is a concatenation of the matrices $\boldsymbol{C}_q(\omega_0)$ and $\boldsymbol{S}_q(\omega_0)$, where each of these matrices has dimension N x q, with (n, k) elements $\cos(k\omega_0 n)$ and $\sin(k\omega_0 n)$, respectively. The notation emphasizes that these matrices depend on the fundamental frequency ω_0 and the number of harmonics q.

The harmonic signal parameters that must be estimated from measured data are collected in a parameter vector $\boldsymbol{P}$:

$$\boldsymbol{P} = \left[\omega_0, u_1, u_2, \dots, u_q, v_1, v_2, \dots, v_q\right]^T = [\omega_0, \boldsymbol{x}]^T \tag{3.4}$$

Estimation of the parameters of the SOH signal is achieved using the Maximum Likelihood Estimation (MLE) method combined with a model order selection method (Lake, 1999; Myung, 2003). Assume for now that the fundamental frequency ω_0 and number of harmonics q are fixed. Then the observed signal $\boldsymbol{Y}$ is a linear model with respect to parameter vector $\boldsymbol{x}$ from (3.1) and (3.3). Since the broadband component $\boldsymbol{B}$ is

modeled as white Gaussian noise distributed as $N(0, \sigma^2\mathbf{I})$, the probability density or likelihood function is

$$\mathrm{p}(\mathbf{Y} \mid \omega_0, \boldsymbol{x}, \sigma^2)=\frac{1}{(2\pi\sigma^2)^{N/2}} \exp\left[\frac{-1}{2\sigma^2}\left(\boldsymbol{Y} - \boldsymbol{W}_q(\omega_0)\boldsymbol{x}\right)^{\mathrm{T}}\left(\boldsymbol{Y} - \boldsymbol{W}_q(\omega_0)\boldsymbol{x}\right)\right] \quad (3.5)$$

The negative log-likelihood function $J_q(\omega_0, \boldsymbol{x}, \sigma^2) = -ln\big(p(\boldsymbol{Y} \mid \omega_0, \boldsymbol{x}, \sigma^2)\big)$ has the following form after dropping terms that are independent of the parameters,

$$\begin{gathered} J_q(\omega_0, \boldsymbol{x}, \sigma^2) = \left(\frac{N}{2}\right) ln(\sigma^2) + \frac{1}{2\sigma^2} L_q(\omega_0, \boldsymbol{x}) \\ L_q(\omega_0, \boldsymbol{x}) = \left\|\boldsymbol{Y} - \boldsymbol{W}_q(\omega_0)\boldsymbol{x}\right\|^2 \end{gathered} \quad (3.6)$$

The maximum likelihood (ML) parameter estimates are the values that maximize the likelihood function for an observed signal $\boldsymbol{Y}$, or equivalently minimize $J_q(\omega_0, \boldsymbol{x}, \sigma^2)$. The noise variance σ^2 is an unknown parameter, so its ML estimate $\widehat{\sigma^2} = (1/N)L_q(\omega_0, \boldsymbol{x})$ may be inserted into (3.6) to obtain the negative log-likelihood that is concentrated with respect to the estimate of σ^2, yielding $J_q\big(\omega_0, \boldsymbol{x}, \widehat{\sigma^2}\big) = \left(\frac{N}{2}\right) ln\left(L_q(\omega_0, \boldsymbol{x})\right)$, where terms independent of the parameters are dropped. For fixed ω_0 and q, the ML estimate of the parameter vector $\boldsymbol{x}$ is as follows, along with the negative log-likelihood function that is further concentrated with respect to the estimate of $\boldsymbol{x}$:

$$\begin{gathered} \hat{\boldsymbol{x}} = \left(\boldsymbol{W}_q(\omega_0)^T \boldsymbol{W}_q(\omega_0)\right)^{-1} \boldsymbol{W}_q(\omega_0)^T \boldsymbol{Y} = \boldsymbol{W}_q(\omega_0)^{+} \boldsymbol{Y} \\ J_q\big(\omega_0, \hat{\boldsymbol{x}}, \widehat{\sigma^2}\big) = \left(\frac{N}{2}\right) ln\left(L_q(\omega_0, \hat{\boldsymbol{x}})\right) = \left(\frac{N}{2}\right) ln\big(\boldsymbol{Y}^T \boldsymbol{\Pi}_q^{\perp}(\omega_0)\boldsymbol{Y}\big) \end{gathered} \quad (3.7)$$

where $\boldsymbol{W}_q(\omega_0)^+$ is the pseudoinverse of $\boldsymbol{W}_q(\omega_0)$, $\boldsymbol{\Pi}_q(\omega_0) = \boldsymbol{W}_q(\omega_0)\boldsymbol{W}_q(\omega_0)^+$ is the orthogonal projection matrix onto the column space of $\boldsymbol{W}_q(\omega_0)$, and $\boldsymbol{\Pi}_q^{\perp}(\omega_0) = \boldsymbol{I} - \boldsymbol{\Pi}_q(\omega_0)$ is the projection onto the orthogonal complement of the column space. The MLE of the fundamental frequency for a fixed number of harmonics q is then the value of ω_0 that minimizes the nonlinear least-squares cost function $\boldsymbol{Y}^T\boldsymbol{\Pi}_q^{\perp}(\omega_0)\boldsymbol{Y}$. However, since q is not known, the number of harmonics and fundamental frequency are estimated jointly by minimizing the Minimum Description Length (MDL) criterion, which has the general structure $J + \left(\frac{r}{2}\right)\ln(N)$, where J is the negative log-likelihood and r is the number of parameters in the model. The number of SOH parameters is $2q$+1 from (3.4), and using the negative log-likelihood in (3.7), the MDL criterion is (dropping terms that are independent of q and ω_0)

$$\{\widehat{\omega_0}, \hat{q}\} = arg \min_{\{\omega_0, q\}} \left\{ \left(\frac{N}{2}\right) ln\left(\boldsymbol{Y}^T\boldsymbol{\Pi}_q^{\perp}(\omega_0)\boldsymbol{Y}\right) + q\, ln\, N \right\} \tag{3.8}$$

Then these values are used to obtain the estimate of $\boldsymbol{x}$ as $\hat{\boldsymbol{x}} = \boldsymbol{W}_{\hat{q}}(\widehat{\omega_0})^+\boldsymbol{Y}$, and then the SOH component of the data is estimated as $\widehat{\boldsymbol{H}} = \boldsymbol{\Pi}_{\hat{q}}(\widehat{\omega_0})\boldsymbol{Y}$ and the broadband component is estimated as $\widehat{\boldsymbol{B}} = \boldsymbol{Y} - \widehat{\boldsymbol{H}} = \boldsymbol{\Pi}_{\hat{q}}^{\perp}(\widehat{\omega_0})\boldsymbol{Y}$. Note that the estimated SOH and broadband components are orthogonal.

Further details on the SOH modelling and estimation approach are available in (Whipps, 2003), including computationally efficient methods for performing the joint minimization in (3.8).

3.2.2 MODIFIED SUM-OF-HARMONICS (SOH) MODEL

The initial SOH model is able to estimate constant amplitude for the i[th] harmonic signal of frequency $i\omega_0$. In order to estimate a time-varying amplitude harmonic signal, the representation of the harmonic signal in (3.3) is modified:

$$h[n] = \sum_{k=1}^{q} u_k[n]\, cos(k\omega_0 n) + v_k[n]\, sin(k\omega_0 n) \tag{3.9}$$

As is observed from (3.9), the Cartesian amplitudes are functions of the sample index. The relationship between the Cartesian amplitudes, $\boldsymbol{u}$ and $\boldsymbol{v}$, and the amplitudes and phases, $\boldsymbol{a}$ and $\boldsymbol{\phi}$, of each harmonic signal present in the recorded signal is:

$$\begin{aligned} u_k[n] &= -a_k[n]\, sin\, \varphi_k[n] \\ v_k[n] &= a_k[n]\, cos\, \varphi_k[n] \end{aligned} \tag{3.10}$$

Now, by assuming that the amplitude parameters follow an m[th] order polynomial function:

$$\begin{aligned} u_k[n] &= u_0^k + u_1^k n + u_2^k n^2 + \ldots + u_m^k n^m \\ v_k[n] &= v_0^k + v_1^k n + v_2^k n^2 + \cdots + v_m^k n^m \end{aligned} \tag{3.11}$$

the harmonic signal is written as:

$$\begin{aligned} h[n] = \sum_{k=1}^{q} &\left(u_0^k + u_1^k n + u_2^k n^2 + \cdots + u_m^k n^m\right) cos(k\omega_0 n) \\ &+ \left(v_0^k + v_1^k n + v_2^k n^2 + \cdots + v_m^k n^m\right) sin(k\omega_0 n) \end{aligned} \tag{3.12}$$

The parameters to be estimated are, now:

$$\boldsymbol{P} = \left[\omega_0, u_i^1, u_i^2, \dots, u_i^q, v_i^1, v_i^2, \dots, v_i^q\right]^T \; for \; i = 0{:}\, m \tag{3.13}$$

Equation (3.1) can be now written as:

$\boldsymbol{Y} = \boldsymbol{W_q x} + \boldsymbol{B}$ where $\boldsymbol{Y}$ is a (Nx1) vector of the recorded signal

$\boldsymbol{x} = \left[x_1, x_2, \dots, x_q\right]^T$ is a ((*2*m*q*) x *1*) vector

$x_k = [u_0^k, u_1^k, u_2^k, \dots, u_m^k, v_0^k, v_1^k, v_2^k, \dots, v_m^k]^T$ is a *2*(m+1)* x *1* vector

$\boldsymbol{W_q} = \left[W_c^1\ W_s^1\ W_c^2\ W_s^2\ \dots\ W_c^q\ W_s^q\right]$ is a *N* x *2*(m+1)*q* matrix

$$W_c^k =$$

$$\begin{bmatrix} cos(k\omega_0 n_1) & n_1\, cos(k\omega_0 n_1) & {n_1}^2\, cos(k\omega_0 n_1) & \dots & {n_1}^m\, cos(k\omega_0 n_1) \\ \dots & \dots & \dots & \dots & \dots \\ cos(k\omega_0 N) & N\, cos(k\omega_0 N) & N^2\, cos(k\omega_0 N) & \dots & N^m\, cos(k\omega_0 N) \end{bmatrix} \text{ is} \tag{3.14}$$

a *N* x *2*(m+1)* matrix

$$W_s^k =$$

$$\begin{bmatrix} sin(k\omega_0 n_1) & n_1\, sin(k\omega_0 n_1) & {n_1}^2\, sin(k\omega_0 n_1) & \dots & {n_1}^m\, sin(k\omega_0 n_1) \\ \dots & \dots & \dots & \dots & \dots \\ sin(k\omega_0 N) & N\, sin(k\omega_0 N) & N^2\, sin(k\omega_0 N) & \dots & N^m\, sin(k\omega_0 N) \end{bmatrix} \text{ is a}$$

N x *2*(m+1)* matrix

Following the steps of the Maximum Likelihood Estimation method combined with the MDL model order selection method described in part A of section II, and using the new expression for the matrix $\boldsymbol{W_q}$, estimates of both ω_0 and q are obtained. The only difference in this case is that the number of parameters *r* in the model is now 2*q(m+1)*+1

from (3.13), and using the negative log-likelihood function in (3.7), the MDL criterion is (dropping terms that are independent of q and ω_0)

$$\{\widehat{\omega_0}, \hat{q}\} = arg \min_{\{\omega_0, q\}} \left\{ \left(\frac{N}{2}\right) ln\left(\boldsymbol{Y}^T \boldsymbol{\Pi}_q^{\perp}(\omega_0)\boldsymbol{Y}\right) + q(m+1)\, ln\, N \right\} \tag{3.15}$$

As soon as ω_0 and q are defined, the estimate of $\boldsymbol{x}$ can be obtained by $\hat{\boldsymbol{x}} = \boldsymbol{W}_{\hat{q}}(\widehat{\omega_0})^{+}\boldsymbol{Y}$, and then the SOH component of the data is estimated as $\widehat{\boldsymbol{H}} = \boldsymbol{\Pi}_{\hat{q}}(\widehat{\omega_0})\boldsymbol{Y}$ and the broadband component is estimated as $\widehat{\boldsymbol{B}} = \boldsymbol{Y} - \widehat{\boldsymbol{H}} = \boldsymbol{\Pi}_{\hat{q}}^{\perp}(\widehat{\omega_0})\boldsymbol{Y}$ **,** as already presented in Section 3.2.1.

Furthermore, it is expected that the estimation accuracy of random and varying-level fluctuations in the amplitude of each narrowband component of a signal using a polynomial function will decrease as the number of cycles in the signal increases. Therefore, it is proposed that the signal is segmented into several cycle parts and that the proposed method is applied independently on each part.

3.3 NUMERICAL SIMULATIONS

An initial computational investigation was carried out in order to enable understanding of the relationship between the parameters of the model including the sampling frequency of the signal, the narrowband (harmonic)-to-broadband signal ratio, the number of cycles per segment, and the order of polynomial used to approximate the signal amplitude changes.

The input signal to these simulations comprises a fixed sum-of-harmonics signal and white Gaussian noise with variance σ^2 that is chosen to set the harmonic to

broadband ratio. The SOH signal *h(t)* consists of the first three harmonics of a sinusoid signal at f = 2MHz, described by the following equation

$$h(t) = (100 + A_1)\,sin(2\pi f t) + (40 + A_2)\,sin(2\pi(2f)t) + (20 + A_3)\,sin(2\pi(3f)t) \quad (3.16)$$

$where\ A_i$ is a time-varying amplitude distortion added to the fixed amplitude of each cycle for each frequency component of the sum-of-harmonics signal. This distortion is generated by normally distributed random samples (one for every cycle of the sum-of-harmonics signal) filtered with a narrowband bandpass filter, and it is amplified to be 12dB lower than the initial amplitude of each component.

The second component, $b(t)$, of the input signal is the broadband component generated as white Gaussian noise, and its variance σ^2 is chosen to provide a range of narrowband-to-broadband ratios (NBR) between 10 and 50dB. NBR is computed according to the following equation:

$$NBR = 20\log_{10}(\max(h)\,/\max(b)) \quad (3.17)$$

The broadband component is meant to represent the emissions generated by inertially collapsing bubbles. These emissions are dependent on the second derivative of the volumetric change in the bubble, and inertial collapse will therefore invariably lead to a spectral signature that will appear as broadband over the bandwidth of the detecting transducer. For single bubbles, the broadband response can be periodic, typically at subharmonics of the main excitation frequency, due to arrested collapses that result in period doubling and period tripling depending on the bubble size as dictated by the bifurcation diagram. However, in situations involving multiple (rather than single) bubbles and where the bubble size can be tightly controlled, the acoustic emissions

arising from inertial collapses can be readily modelled as white Gaussian noise. Recent work enabling tight control of the initial bubble size to be sub-resonant and monodisperse, evidenced experimentally that inertial cavitation has an exclusively broadband signature modulated by the frequency response of the receiving transducer (J. J. Kwan et al., 2015). These broadband acoustic emissions can be faithfully modelled as white Gaussian noise following de-convolution of the frequency response of the transducer.

The range of values for each of the parameters investigated in these simulations is summarized in Table 3.1:

Table 3.1.Range of values of the set of parameters tested in the simulations.

Parameter	Value range
Sampling Frequency	30 – 120MHz
Narrowband-to-Broadband ratio (NBR)	10 – 50dB
Number of cycles per segment	4 – 40
Order of polynomial	0 – 5

Fig. 3.1 demonstrates the effect that each of the parameters investigated has on the performance of the model. The mean-square-error (MSE) between the input SOH signal and the estimate using the SOH model is used as a performance metric for the different parameter sets, and decrease in the MSE signifies performance improvement for the SOH model. MSE is computed according to the following equation:

$$MSE = \frac{1}{N}\sum_{n}\big(s(n) - h(n)\big)^2 \quad in\ V^2 \tag{3.18}$$

where n represents the sample number of the harmonic signal h and the estimated harmonic signal s, and N is the total number of samples in the harmonic signal.

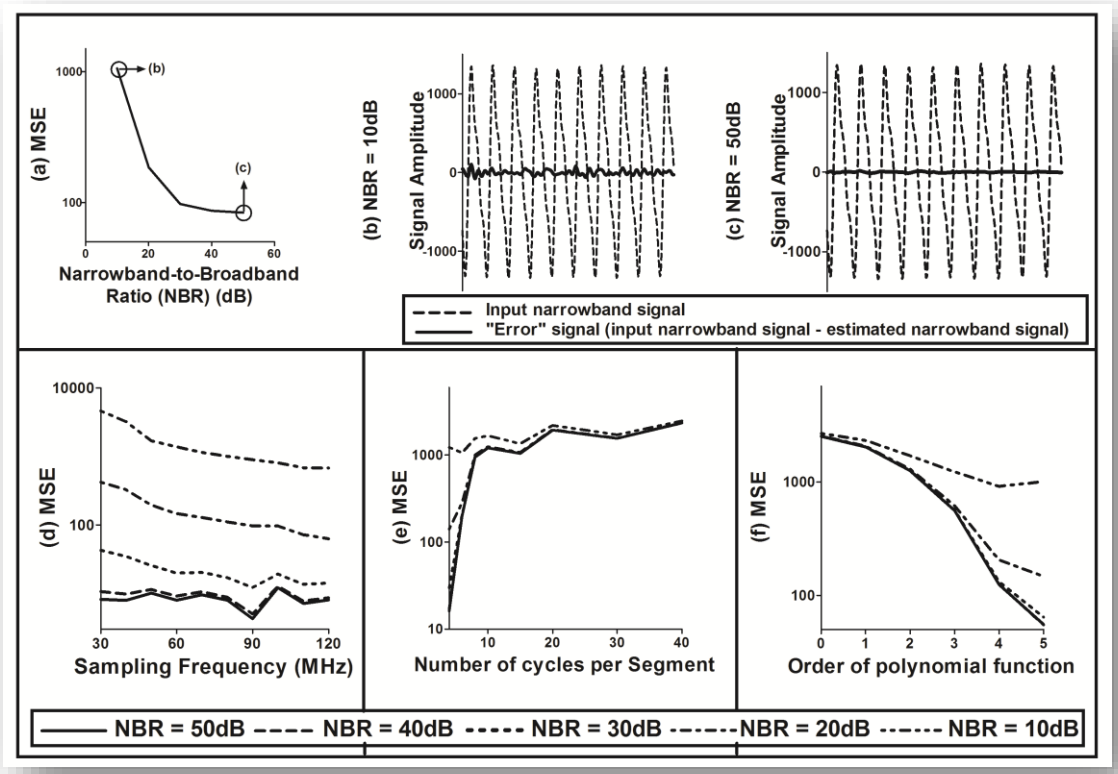


Figure 3.1 Simulation results for determining the effect of the parameters of the SOH model in its performance using mean-square-error (MSE) as a performance measure. The parameters evaluated are: (a) Narrowband-to-Broadband ratio (NBR) for sampling frequency = 82MHz, number of cycles per segment = 5, and order of polynomial = 2 (subfigures (b) and (c) demonstrate in the time domain a part of the input narrowband signal (dashed line), and the corresponding "error" signal (solid line) resulting from the subtraction of the estimated narrowband signal using the SOH model from the input narrowband signal), (d) Sampling frequency over a range of NBR (number of cycles per segment = 5, and order of polynomial = 2), (e) Number of cycles per segment over a range of NBR (sampling frequency = 82MHz, and order of polynomial = 2), and (f) Order of polynomial function over a range of NBR (sampling frequency = 82MHz, and number of cycles per segment = 5).

A significant improvement in the performance of the model is observed as the narrowband-to-broadband signal ratio (NBR) increases. This implies that estimation of a narrowband signal in the presence of a broadband component acting either as signal-of-interest or interference, and subsequent estimation of the broadband component through coherent subtraction, are more accurate as the level of the narrowband

component increases with respect to the level of the broadband signal. A small part of the generated narrowband signal is displayed in Fig. 3.1b and 3.1c, along with the error signal between the generated and the estimated with the SOH model narrowband signal, for two NBR, demonstrating the level of the error in estimation in these two cases. With regards to the effect of the sampling frequency on the performance of the SOH model, it is observed that increase of the sampling frequency does not cause subsequent substantial decrease in the MSE. As far as the number of cycles per segment is concerned, it is observed that as this parameter decreases, better estimation of the narrowband component is achieved in the cases of high NBR. This could be explained by considering that when smaller signal segments are processed by the model, estimation of the signal amplitude fluctuations using a polynomial function is more accurate. However, when NBR is low, the performance of the model is decreased and the number of cycles per segment does not affect it substantially. Finally, evaluation of the effect of the order of the polynomial function chosen to represent changes in the amplitude of the narrowband signal has been performed. It is observed that in the cases of high NBR, as the polynomial order increases, the amplitude fluctuations are better fitted leading to decrease in the MSE.

3.4 EXPERIMENTAL RESULTS

3.4.1 EXPERIMENTAL SETUP

The experimental setup shown in Fig. 3.2 aims to mimic clinical conditions that involve simultaneous generation of both narrowband (in this particular case harmonic) and broadband acoustic emissions. The goal is to evaluate the performance of the SOH model in classifying and quantifying broadband and narrowband components, when compared to conventional comb filters.

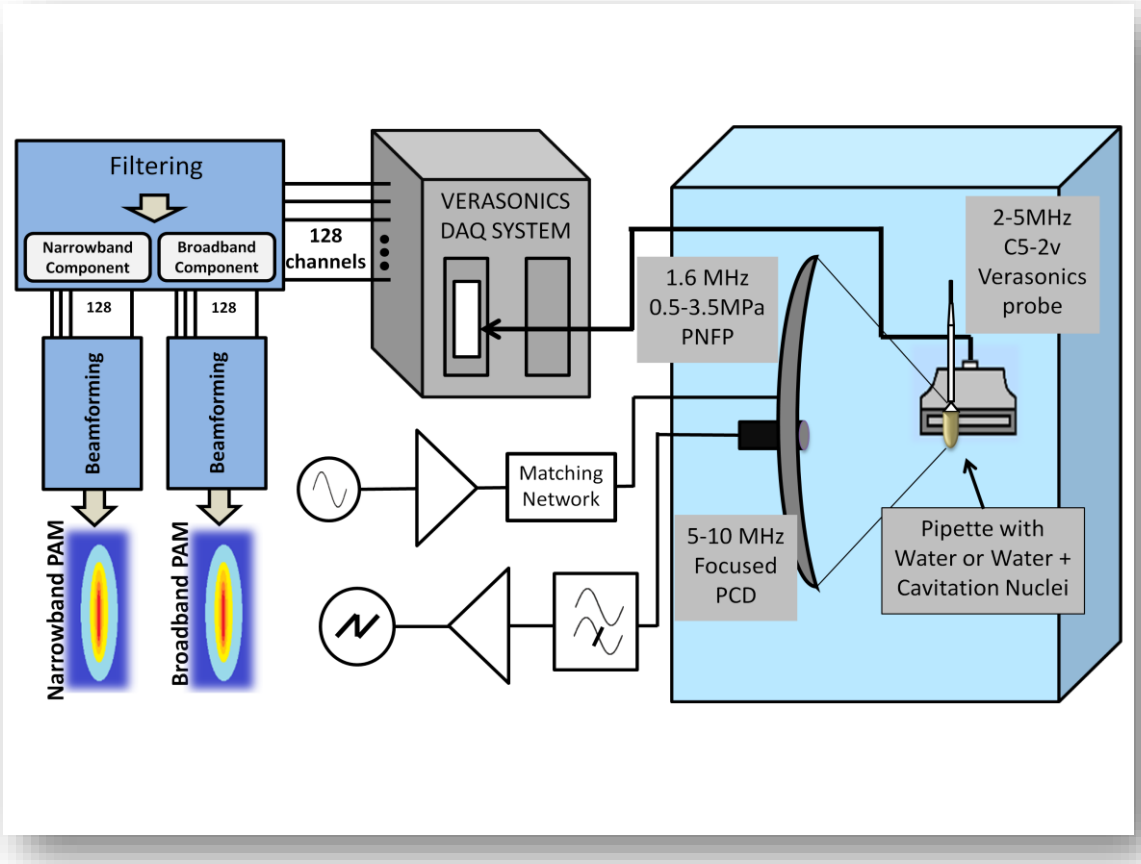


Figure 3.2 Experimental setup involving a pasteur pipette filled with either water or cavitation nuclei is placed at the focus of a HIFU transducer driven at 1.6MHz. The HIFU transducer is co-aligned with a 5-10MHz PCD and a 2-5MHz array for B-mode imaging and passive recording of acoustic emissions. These emissions are filtered, separating the harmonic and broadband component, which are then independently processed using PAM to provide separate maps of sources of harmonic and broadband emissions.

A 0.5MHz spherically focused, single-element ultrasound transducer (H-107D SN12; Sonic Concepts, Bothell, Washington, USA), with active diameter 64mm, focal length 62.6 mm, and a central, circular cut-out of diameter 22.6mm is placed in a large water tank of degassed, filtered water. It is co-aligned with a single-element spherically focused 7.5MHz transducer (aperture 12.5mm, focal length 75mm, Panametrics, Waltham, MA, USA), used as a passive cavitation detector (PCD), responsible for detecting the occurrence of inertial cavitation at the focal region. The HIFU transducer is connected to a function generator (33250A 30MHz function/arbitrary waveform generator, Agilent Technologies 2015), and it is driven at the 3rd harmonic (1.682MHz) transmitting a 1000-cycles sinusoid signal of increasing amplitude (0.5 – 3.5MPa), amplified by a 55dB power amplifier (1140LA, E&I, Rochester, NY, USA).

A Verasonics C5-2v convex array transducer (central frequency 3.5MHz, 128 elements, pitch 0.508mm, sensitivity -55.5 to -50.5dB, elevation focus 60mm, Verasonics, Inc. Redmond, WA) is placed perpendicular to the HIFU transducer with a plane of view that contains the focus of the HIFU transducer. The probe is connected to the Verasonics Vantage Research Ultrasound System (Verasonics, Inc. Redmont, WA), which is capable of simultaneously recording the signals received on each of the 128 channels of the array in order to enable generation of PAM maps.

A pasteur pipette is placed at the focus of the HIFU transducer and it is filled with either deionized water or a suspension of nanoparticles that act as cavitation nuclei; these nanoparticles are designed to lower the cavitation threshold of pure water to less than 2.5MPa at 1.682 MHz and enable sustained inertial cavitation activity within the sample volume (James J. Kwan et al., 2015; J. J. Kwan et al., 2015). The signal generated by the HIFU transducer propagates nonlinearly through the medium and it is reflected by the walls of the pipette. At the same time, inertial cavitation is

expected to take place within the pipette above a certain amplitude threshold that depends primarily on the content of the pipette. Therefore, harmonic acoustic emissions due to nonlinear propagation and scattering, and broadband acoustic emissions due to inertial cavitation are simultaneously generated and passively recorded by the imaging probe.

3.4.2 SIGNAL FILTERING

The goal of this experiment is to process the recorded signals with either the proposed SOH model or a fixed comb filter, and quantify and compare the recovery of the two signal components for the two methods. Because either method of filtration should be implementable as part of a system for real-time monitoring of ultrasound therapies, only causal methods of filtration are used to benchmark the performance of the SOH model.

In the case of comb filtering, filters have been designed using the DSP toolbox of MATLAB. They are meant to attenuate the frequencies that are multiples of the driving frequency of the HIFU transducer. More specifically, they are IIR Butterworth filters of order 11, sampling frequency equal to 17.8MHz, they comprise of 6 notches in the frequency range of 0 to 8.1MHz, and their bandwidth is 0.5MHz, 1MHz, and 1.5MHz respectively. The selection of the order of the comb filters has been based on two factors: the ability of the filter to remove the narrowband (harmonic) components effectively without affecting the broadband component, and the time required for filtering, since the goal is to implement a real-time system for passive acoustic mapping.

Regarding the SOH model, the recorded signal has been segmented into 8 cycles, and a 3rd order polynomial function has been chosen to represent the variations

in the amplitude of the narrowband signal. The selection of the above parameters has been based on our simulation results, providing us with a satisfying filter performance and the ability to be performed in real-time.

No cavitation nuclei

At this stage of the experiment, no inertial cavitation is expected to take place in the pipette for the range of pressures induced at the HIFU focus. This hypothesis is supported by analyzing the signal from the middle channel of the array, and observing no change in its variance with increasing peak rarefactional pressure amplitude.

Based on this assumption, the broadband component of the recorded signal in each channel of the array should correspond to the baseline noise of the system, i.e. the electrical noise of the system, at each pressure. The baseline noise of the system is measured at each pressure using the setup in Fig. 3.2, when there is no pipette placed at the focal region. It is expected that the power of the baseline noise remains constant as pressure increases. However, as observed in Fig. 3.3 and Fig. 3.4, in which baseline noise power is represented with a solid black line, there is an increase as pressure increases. Such an observation implies that there are some harmonic components in the recorded signals, potentially due to reflections or direct propagation of the incident wave towards the elements of the array. Since the baseline noise is not filtered, this could, therefore, explain the increase in power due to pressure increase. From this point on, the power of the baseline noise will be used for comparison with the power of the broadband component, as this is estimated after filtering of the recorded signals, in the case where a pipette filled with water is placed at the HIFU focal region.

Focusing now on the signals recorded by the array elements when pipette filled with water is placed at the HIFU focus, by removing the harmonic components from the signal recorded from the middle (64^{th}) channel of the array using either the proposed SOH model or a comb filter, the power of the remaining signal, i.e. the power of the broadband component, should be very close to the power of the baseline noise at each pressure, since no cavitation is expected.

Prior to comparison of the proposed SOH model with conventional comb filtering, the optimal parameters for the comb filters need to be chosen. For this purpose, the power of the broadband component, after harmonic components have been removed from the recorded signals using four different comb filters of the same bandwidth (1.5MHz) and different order is calculated. The calculated power is compared with the power of the baseline noise and presented in Fig. 3.3 for the range of pressures tried in the experiment. It is expected that as the filter order increases, the peaks of the filter become sharper, providing at the same time higher narrowband signal rejection, as observed by the magnitude response of the filters. This means conceptually that the harmonics are more effectively attenuated, but the frequency range surrounding the harmonics becomes more readily attenuated too. Therefore, depending on the order selected there is a trade-off between harmonic rejection efficiency and unwanted broadband signal rejection (signal-of-interest remaining unaffected). In Fig. 3.3 it is demonstrated that as the order of the filter increases the calculated broadband power decreases, but after a certain point it reaches a plateau. At the same time, as the pressure increases the broadband power for all the comb filters still increases, signifying that there is still some harmonic energy remaining after filtering, and the decrease in the power for increasing filter order could not only be due to better harmonic rejection but also due to part of the broadband energy being erroneously filtered out. It is therefore,

believed that comb filter of order 11 performs adequately, as the broadband power calculated is close to the baseline noise, providing a satisfying compromise between harmonic rejection and preservation of the signal-of-interest. Furthermore, increase of the order of the filter has a significant impact on the computational cost of filtering. Since the goal is to enable real-time PAM, an 11th order filter was thus chosen as it enables generation of passive acoustic maps at a frame rate comparable to SOH, namely approximately 3Hz (main computer specifications: Intel Xeon CPU E2-2650 v2, 32GB RAM, NVIDIA GeForce GTX TITAN Black GPU).

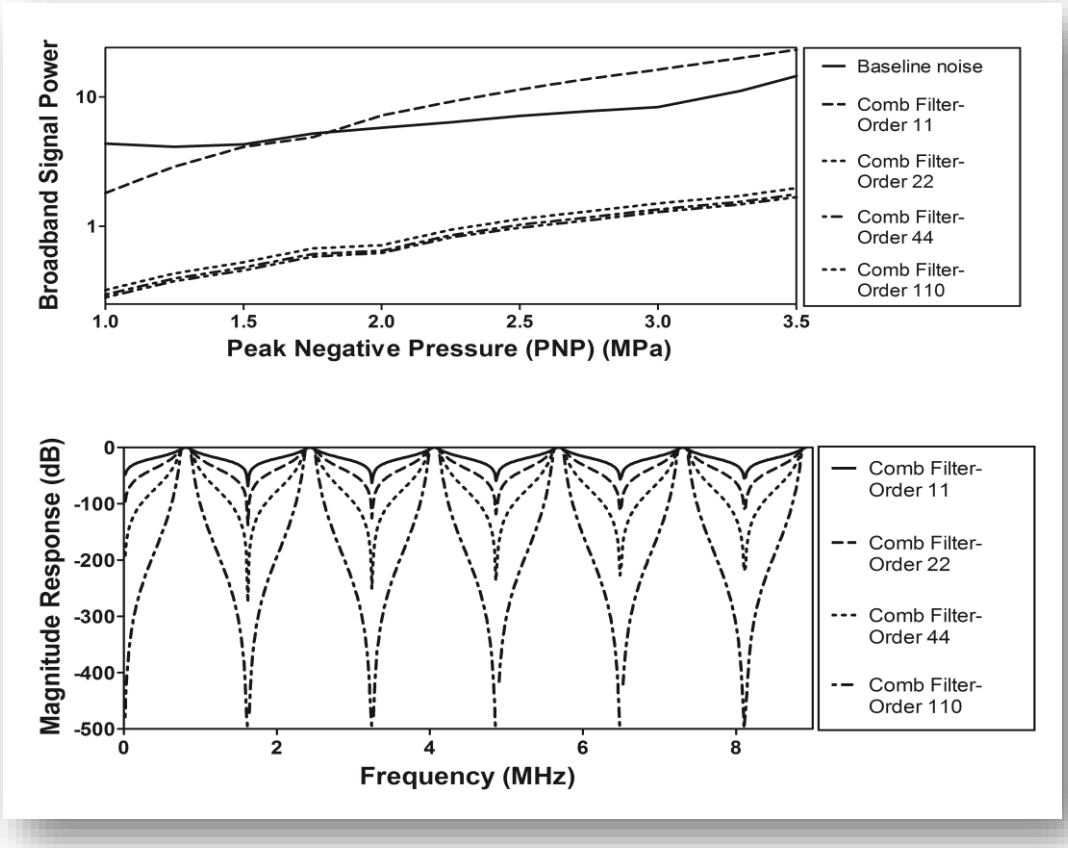


Figure 3.3 Power of the broadband component of the signal recorded at the 64th channel of the array, when water is placed in the pipette, for the range of peak negative pressures tested in the experiment, when the harmonic components are filtered out using a comb filter of 1.5MHz bandwidth and order equal to 11, 22, 44 or 110. The power of the baseline noise corresponds to the recorded signal when nothing is placed at the focus. The magnitude response of the different comb filters with respect to frequency is displayed in the lower part of the figure.

By selecting the order of the three comb filters to be equal to 11, the only parameter allowed to vary amongst them is the bandwidth. In Fig. 3.4 the power of the broadband component corresponding to the 64^{th} channel (central element) of the array is presented after filtering of the narrowband components using either the SOH model or one of the fixed-order (11^{th} order), varying bandwidth (0.5MHz, 1MHz and 1.5MHz) comb filters. It is observed that as the bandwidth of the comb filter increases, its performance is improved, and the power of the broadband component approaches the power of the baseline noise. For the ideal filter, the broadband power should remain constant across all ultrasound pressure amplitudes in the absence of cavitation. The broadband power should thus remain unaffected by changes in the narrowband-to-broadband ratio, whilst at the same time being no greater than the baseline noise power. The only filter that satisfies these criteria is the SOH model, which can therefore be deemed to outperform the chosen comb filters. On the contrary, when the signal is filtered using a comb filter, an increase in the power of the broadband component is observed as pressure increases. By studying the spectra of the recorded signal at different pressures, a leakage of harmonic energy is observed at a wider frequency band. As a consequence, application of the same fixed comb filter at a signal of increasing pressure will result in increased harmonic power not being efficiently filtered out. This power will be misinterpreted as broadband power, and as is expected, it increases as the pressures increases. At the same time, as the bandwidth of the filter widens, the filter is also attenuating part of the broadband component. The above two observations combined could potentially explain the lower power, compared to baseline broadband power, obtained for weak excitation pressures in the case of the wide comb filter. More specifically, at low pressures the narrowband components are more effectively filtered out, but at the same time part of the broadband component is also

filtered out, leading to decreased estimated broadband power. As the pressure increases, filtering of part of the broadband signal still takes place, but the leakage of harmonic energy from the filter increases. The harmonic components remaining in the signal as pressure increases are higher compared to the broadband component falsely filtered out, and, as a consequence, the estimated broadband power increases.

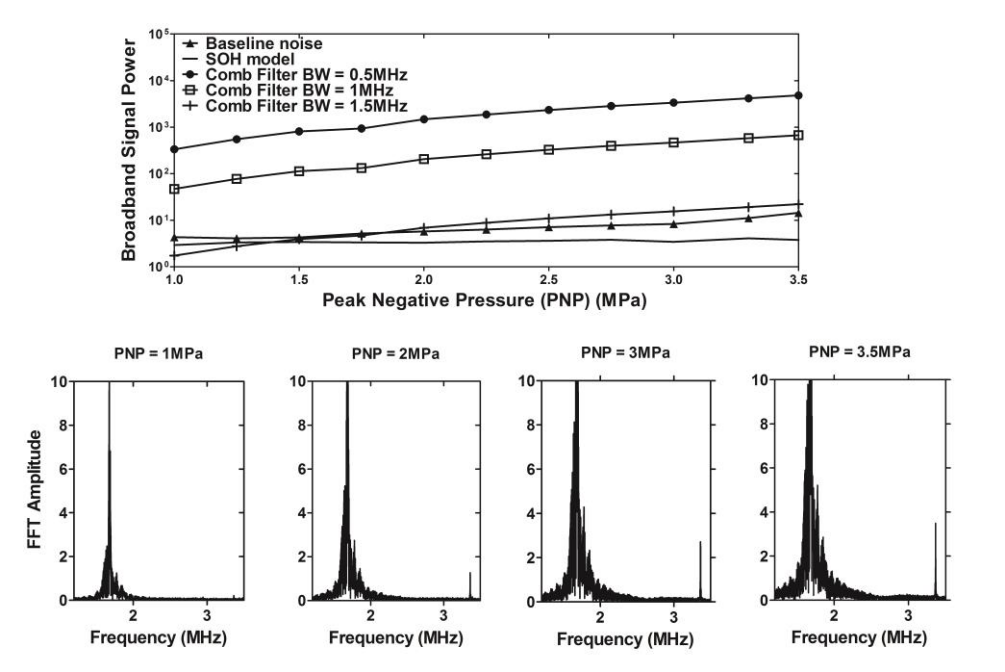


Figure 3.4 Power of the broadband component of the signal recorded at the 64th channel of the array, when water is placed in the pipette, for the range of peak negative pressures tested in the experiment, when the harmonic components are filtered out using either one of the chosen comb filters or the SOH model. The power of the baseline noise corresponds to the recorded signal when nothing is placed at the focus. The spectrum of the totally recorded signal from the 64th channel of the array is displayed in the lower part of the figure at four different pressures (1, 2, 3, and 3.5MPa) that cover the whole range of pressures evaluated.

With cavitation nuclei

By replacing the water-filled pipette with a pipette containing a suspension of cavitation nuclei it is expected that above a certain pressure threshold, inertial cavitation will occur. In Fig. 3.5 the spectrum of the PCD data, as well as the spectrum of the signal recorded by the 64th channel of the array, is displayed over the range of pressures tested in the experiment. In both sets of figures, it is observed that there is a significant increase in the level of broadband noise between 2 and 3MPa, indicating that the inertial cavitation threshold of the cavitation nuclei used in this experiment at 1.6MHz is between 2MPa and 3MPa.

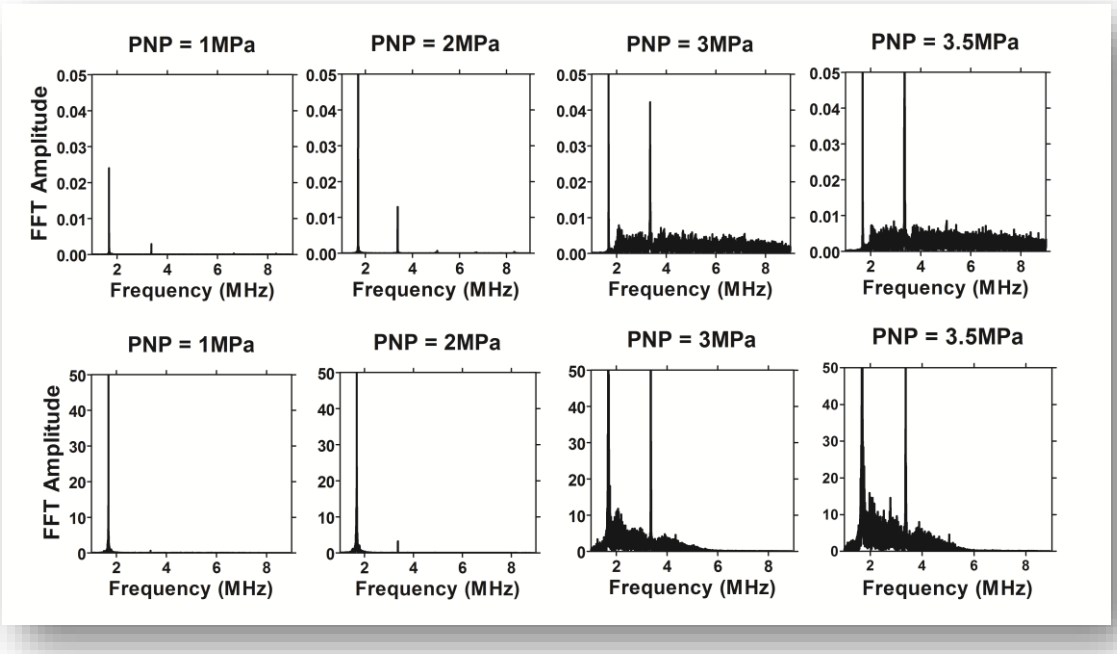


Figure 3.5 The spectrum of the PCD data (top) and the signal recorded at the middle (64th) channel of the array (bottom) is displayed, for four different pressures (1, 2, 3, and 3.5MPa) covering the range of pressures tested in the experiment, when cavitation nuclei are placed in the pipette.

To further establish the conclusions from Fig. 3.4 regarding the efficiency of the SOH model in rejecting the narrowband component while preserving the broadband component, Fig. 3.6 is introduced. In this figure the spectrum of the signal recorded from the middle (64^{th}) element of the array, and the spectra of the broadband component of the recorded signal after being filtered with either the SOH model, the wide or the narrow comb filter are presented. The SOH model is able to remove the narrowband signal component effectively with minimal impact on the broadband signal component. By contrast, the narrow comb filter fails to remove all of the narrowband peak, and the wide comb filter removes much of the broadband signal surrounding the peak, resulting in misclassification of part of the broadband energy as narrowband.

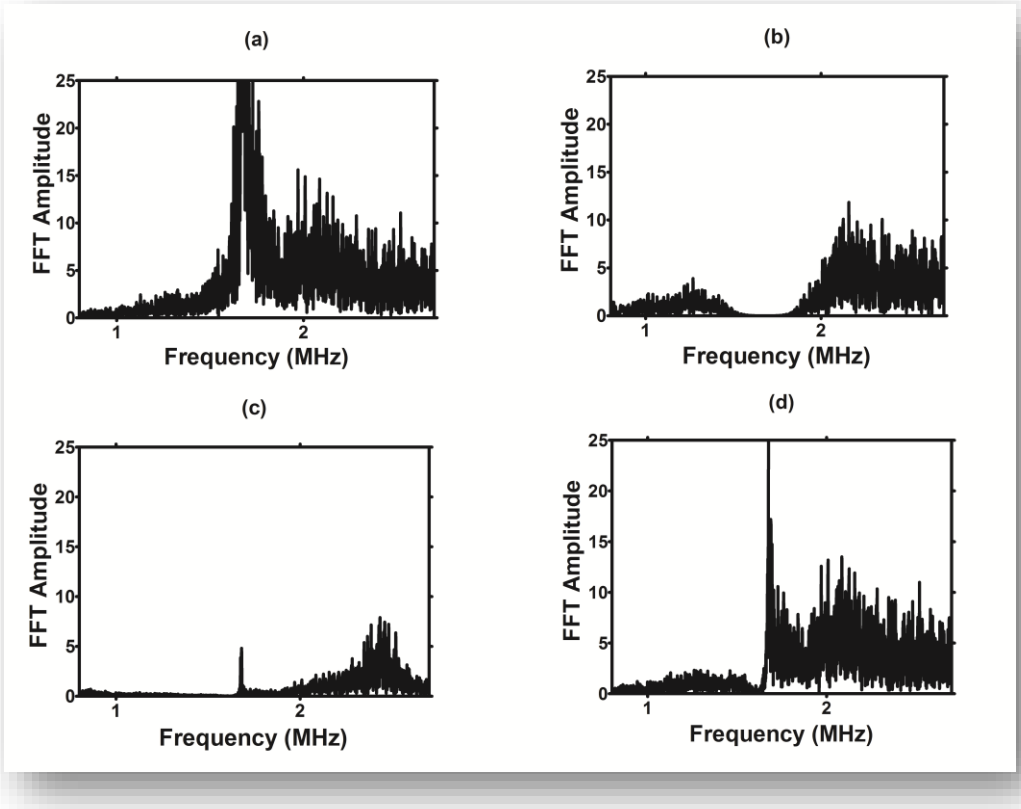


Figure 3.6 Frequency spectrum of (a) the recorded unfiltered signal from the middle (64^{th}) channel of the array at 3.5MPa in the presence of cavitation nuclei, filtered with (b) the SOH model, (c) a wide bandwidth comb filter (order = 11, sampling frequency = 17.8MHz, bandwidth = 1.5MHz), and (d) a narrow bandwidth comb filter (order = 11, sampling frequency = 17.8MHz, bandwidth = 0.5MHz).

3.4.3 PASSIVE ACOUSTIC MAPPING

The second aim of the experiment is to evaluate the effect of the filtering method on the spatial accuracy of PAM maps. Particular attention is placed on the capability of each method to remove interference from strong harmonic reflections from the pipette walls. Passive acoustic maps of inertial cavitation are generated for the broadband component of data filtered using either the SOH or comb-filter method and applying the RCB beamforming algorithm, with the factor ε being equal to 6. The optimal value of epsilon is data-dependent, and the selection of this value is based on a trade-off between optimal interference suppression and optimal energy estimation (Coviello et al., 2015). During the experiments presented in this section, the same data sets have been processed with either the SOH model or the comb filters, and in both cases the same value of epsilon has been used to generate PAM maps. Therefore, the comparison of the filtering techniques in the context of PAM is not affected by the selection of the value of epsilon.

No cavitation nuclei

Since no inertial cavitation takes place in the pipette, the generated maps should display no activity. In Fig. 3.7 the maps corresponding to all filtering techniques are displayed, using the same linear color scale, at three different pressures (1MPa, 2.5MPa, and 3.5MPa). Since in this part of the experiment there are no sources of inertial cavitation to be mapped using PAM, no variation is expected as pressure increases. The use of a common color scale among all filtering methods and pressures allows comparison of the potential changes observed in the maps. Additionally, it provides a direct comparison of the level of the source energy mapped with each

filtering approach, to further validate the conclusions made from Fig. 3.4. The white areas displayed on the PAM maps signify the locations of the walls of the pipette, as these appear on the B-mode images recorded, after a -6dB power threshold is applied. The minimum and maximum value in the colormap is the minimum and maximum PAM power respectively calculated in the case of the SOH model for all excitation pressure amplitudes tested in this part of the experiment.

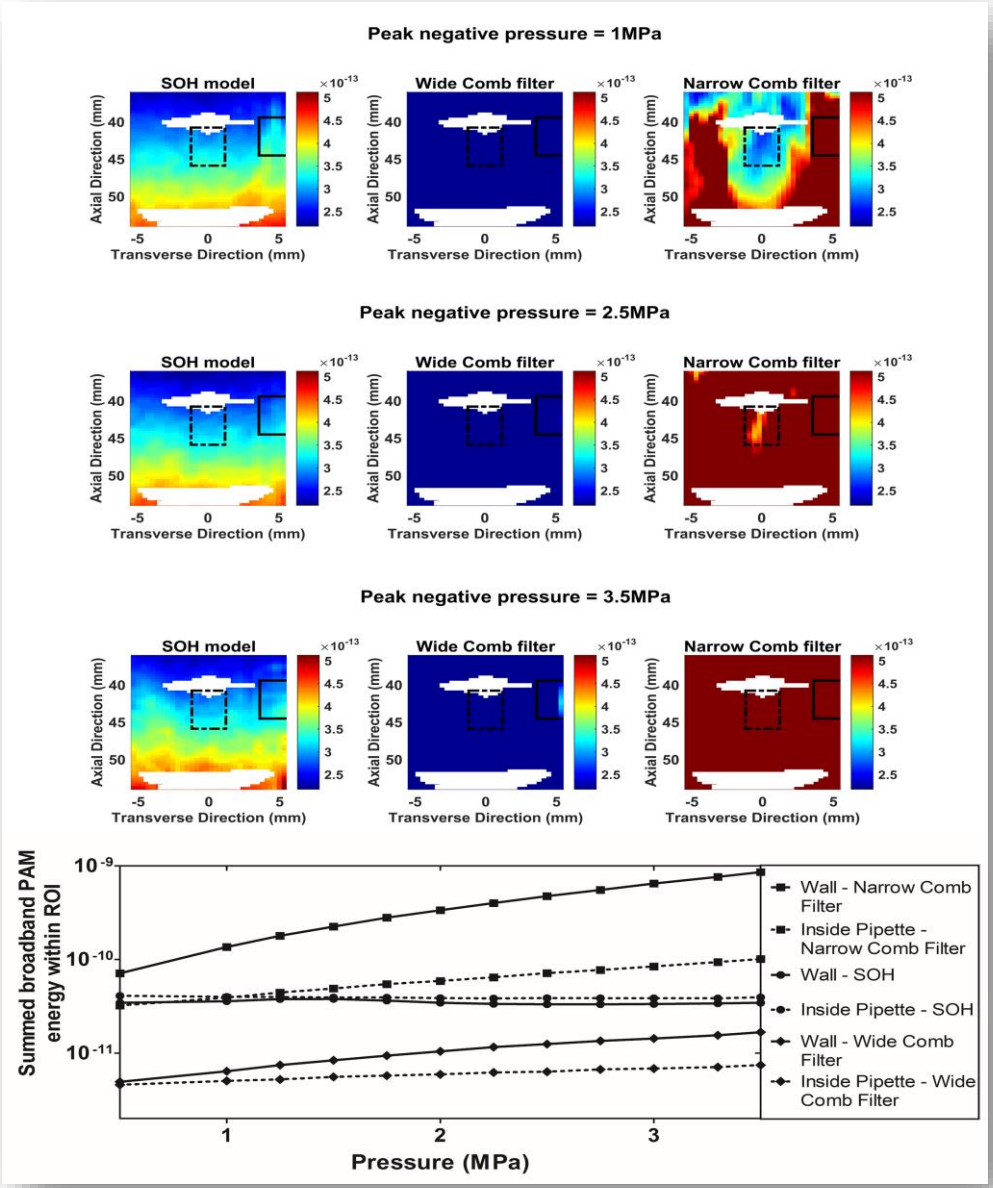


Figure 3.7 PAM maps of sources of broadband acoustic emissions, when water is placed in the pipette, are displayed at three different pressures: 1MPa, 2.5MPa, and 3.5MPa. The white areas displayed signify the reflections from the two walls of the pipette, as they appear on B-mode images after a -6dB power threshold is applied. The broadband component is determined by filtering the received acoustic emissions with either the SOH model (left maps), a wide bandwidth (order = 11, sampling frequency = 17.8MHz, bandwidth = 1.5MHz) (middle maps) or a narrower bandwidth (order = 11, sampling frequency = 17.8MHz, bandwidth = 0.5MHz) (right maps) comb filter. The colormap used for all the subfigures is defined by the minimum and maximum PAM power calculated in the case of the SOH model among all pressures tested in the experiment. Two ROI have been defined in the PAM maps, one on the vertical walls of the pipette with respect to the array, and one in the middle of the pipette. The summed PAM power in each of these regions is displayed in the lower part of the figure for the case of the SOH model and the two comb filters over the range of pressures tested in the experiment.

As the pressure increases, the maps corresponding to the SOH model remain unchanged and no activity is observed, as is expected. However, in the cases of the narrow comb filter significant activity is observed in the maps, even at the lowest pressure, falsely indicating that inertial cavitation takes place. Therefore, it is safe to conclude that the mapped activity corresponds to harmonic energy that is not properly filtered out. In the case of the wide bandwidth comb filter, which according to our previous results performs better than the other comb filters, it is observed that some activity is mapped at the regions where the vertical (with respect to the array) boundaries of the pipette exist. Since strong harmonic reflections of the incident wave are expected by these interfaces, this enhances the previous conclusion regarding high-level harmonic emissions not efficiently being filtered out and therefore, misinterpreted as broadband. At this point it is important to explain the increase in PAM power with respect to depth observed in the case of the SOH model for all pressures. The signal mapped in these figures is the electrical background noise of the system, since no cavitation takes place. As part of the PAM algorithm, signal amplitude compensation for spherical spreading of the recorded acoustic emissions takes place. But since noise is independent of distance from the array, spherical spreading compensation of the noise signal will result in the increase of the noise contribution with respect to distance. This phenomenon is not observed in the PAM maps corresponding to the two comb filters due to the use of the same colormap for all filters, although the signal amplitudes mapped are considerably different.

The above conclusions could be further enhanced by selecting regions of interest (ROI) in the PAM maps and comparing the summed PAM power within these regions. Two regions have been selected in our case, one at the vertical (with respect to the array) boundaries of the pipette, and one in the middle of the pipette, as demonstrated in

Fig. 3.7. Regarding the SOH model, the summed power in both regions is fairly equal, as is expected, since in this case the broadband component mapped corresponds only to the background noise of the system. It also remains stable regardless of the increase in the pressure, indicating that all the harmonic components have been efficiently removed at all pressures. On the other hand, in the case of the comb filters, the summed power from both regions increases as the pressure increases, indicating that part of the harmonic component has not been filtered out. This effect is mainly apparent in the region near the walls of the pipette, but it is also observable in the region in the middle of the pipette mainly due to a combination of the point-spread function of the PAM method and reflections from the horizontal boundaries of the pipette.

With cavitation nuclei

The goal of this part of the experiment is to evaluate the spatial accuracy of mapping inertial cavitation using the SOH model as a filtering technique compared to comb filtering. Similar to the previous stage of the experiment, PAM maps are generated using the broadband component of the recorded signals from the array, and displayed in Fig. 3.8 for three different pressures (1MPa, 2.5MPa, and 3.5MPa) with the same linear color scale. The colormap in the sub-figures of Fig. 3.8 is defined according to the minimum and maximum value of PAM power calculated for the case of the SOH model among all pressures tried in this part of the experiment. The white areas displayed on the PAM maps signify the locations of the walls of the pipette, as these appear on the B-mode images recorded, after a -6dB power threshold is applied.

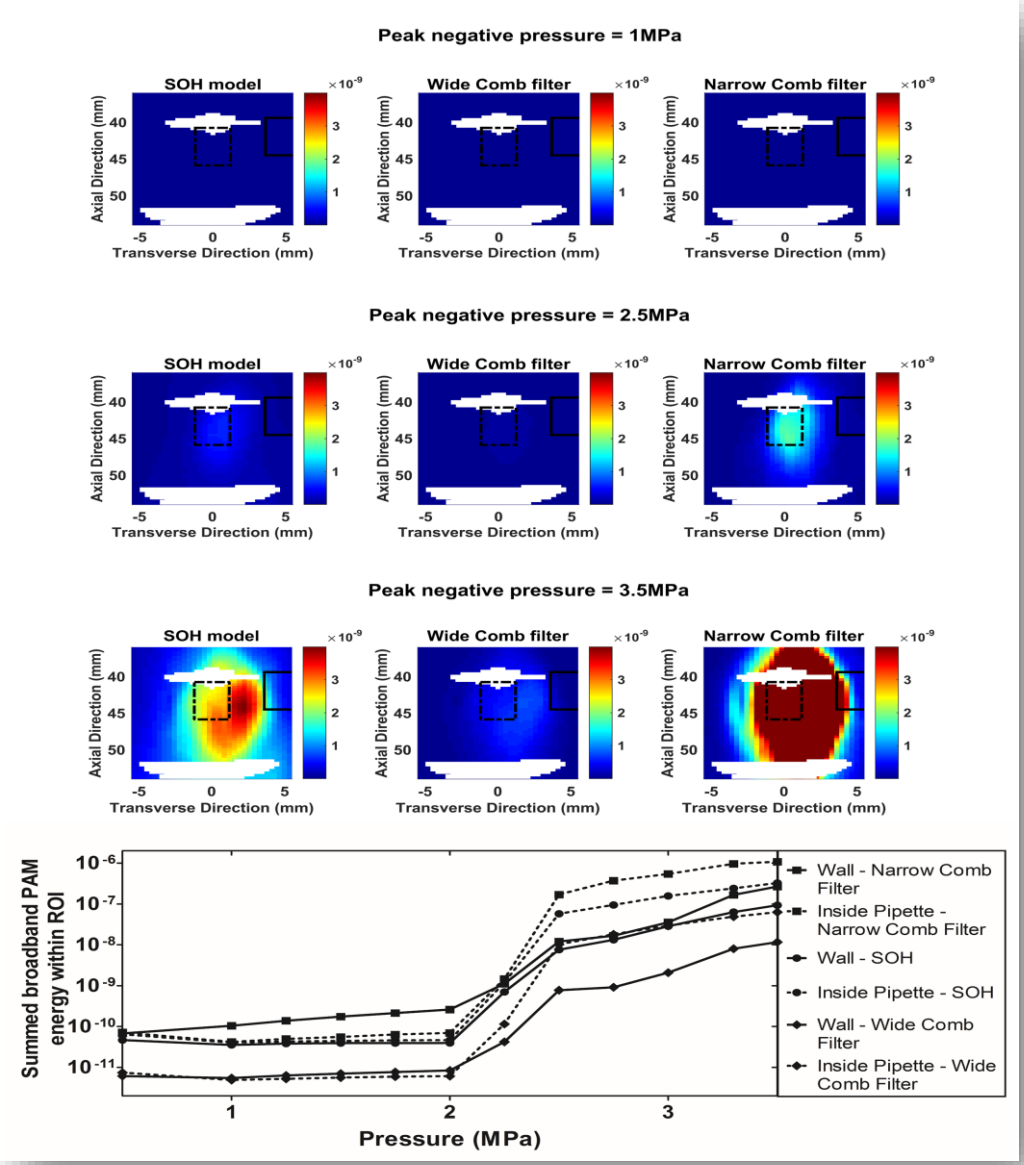


Figure 3.8 PAM maps of sources of broadband acoustic emissions, when cavitation nuclei are placed in the pipette, are displayed at three different pressures: 1MPa, 2.5MPa, and 3.5MPa. The white areas displayed signify the reflections from the two walls of the pipette, as they appear on B-mode images after a -6dB power threshold is applied. The broadband component is determined by filtering the received acoustic emissions with either the SOH model (left maps), a wide bandwidth (order = 11, sampling frequency = 17.8MHz, bandwidth = 1.5MHz) (middle maps) or a narrower bandwidth (order = 11, sampling frequency = 17.8MHz, bandwidth = 0.5MHz) (right maps) comb filter. The colormap used for all the subfigures is defined by the minimum and maximum PAM power calculated in the case of the SOH model among all pressures tested in the experiment. Two ROI have been defined in the PAM maps, one on the vertical walls of the pipette with respect to the array, and one in the middle of the pipette. The summed PAM power in each of these regions is displayed in the lower part of the figure for the case of the SOH model and the two comb filters over the range of pressures tested in the experiment.

At the lowest pressure displayed, which is below the cavitation threshold identified, no inertial cavitation is observed. As the pressure increases and exceeds the cavitation threshold, inertial cavitation activity is more apparent in the case of the SOH model and the narrow comb filter, being significantly more extensive in the case of the narrow comb filter. This observation is consistent with the previously shown results, since overestimation of inertial cavitation is expected due to a significant part of the harmonic signal not being efficiently removed. In the case of the wide comb filter, inertial cavitation activity at the cavitation threshold is barely observable. Finally, at the highest pressure tested significant inertial cavitation activity is observed in all three cases, and in the case of the SOH model this activity is mapped within the expected physical area defined by the boundaries of the pipette, compared to the case of the narrow comb filter, where inertial cavitation seems to happen outside the walls of the pipette, which is not physically possible in the context of the present experimental setup. As far as the wide comb filter is concerned, although inertial cavitation is mapped within the expected physical boundaries, its intensity is lower than that of the SOH model. This could be explained by considering the effect that the wide comb filter has on the recorded signal in the case where inertial cavitation takes place. Due to its wide bandwidth, it removes a significant part, but not the whole, of the harmonic energy, as was already demonstrated, and simultaneously a part of the broadband energy (Fig. 3.6). Therefore, it could lead to underestimation of the intensity and extent of inertial cavitation and potentially cause the onset of inertial cavitation activity to be missed, as was observed in the PAM maps in Fig. 3.8 at 2.5MPa. Finally, by studying the same ROI as in the case where no cavitation nuclei are in the pipette, the same conclusions as above could be drawn. More specifically, the summed PAM power in the ROI at the middle of the pipette is suddenly increasing for all the filters between 2

and 3MPa, where the cavitation threshold is expected. The main difference lies on the fact that before this threshold is exceeded only the SOH model is able to completely remove the narrowband components, indicated by the constant power calculated, while for the comb filters PAM power increases with pressure, as has already been discussed. Regarding the ROI on the wall of the pipette, it is interesting to point out the increase in the summed PAM power for both the SOH model and the comb filters as soon as the cavitation threshold is exceeded. This could be justified by considering the combination of the following two parameters: inertial cavitation taking place near or at the wall of the pipette, and the effect of the point-spread function of the PAM method.

3.5 CONCLUSIONS

A data-adaptive method has been proposed in this chapter for the estimation of the narrowband component in a narrowband-plus-broadband signal. The SOH model has been proven to be effective in estimating the parameters required to define a narrowband signal using an optimization method. Coherently subtracting the estimated narrowband signal from the recorded signal provides an accurate estimate of its broadband component. All analysis in the present work was performed using time-domain filters, however it is possible that notch filters in the frequency domain could minimize inappropriate inclusion or rejection of spectral leakage (O'Reilly and Hynynen 2012, Salgaonkar et al 2009). However, such frequency-domain filters would need to be adjusted based on the pulse duration and windowing applied, whereas the sum-of-harmonics model automatically accounts for pulse duration and windowing effects irrespective of the amplitude of the original signal.

According to our simulations, the proposed method is able to provide an accurate estimation of the narrowband signal component, especially in cases of high NBR. This is a significant advance in the context of clinical applications, where weak broadband signals arising from inertial cavitation need to be distinguished from elevated harmonic signals arising from strongly reflecting structures such as bone.

Splitting the received signal into sub-parts including a small number of cycles prior to processing has been shown to yield further improvements in narrowband signal estimation. A first level of parallelization of the method could be implemented at this point, since estimation of the necessary parameters in each signal part is independent, moving the method one step closer to real-time execution. It is also worth mentioning that the computational complexity of our method is on the order of $O(N^3)$, while the computational complexity of the comb filtering method is lower, on the order of $O(N\ log(N))$, where N is the data size. However, the selection of the appropriate hardware, along with a multiple-level parallelized implementation of the model on the cores of a GPU is expected to achieve real-time performance of the algorithm. Finally, it is important to point out that the selection of the order of the polynomial function used to approximate the changes in signal amplitude plays a significant role in the performance of the model. However, increased accuracy comes at the expense of increased computation.

Our *in vitro* experiments allowed us to investigate the impact of improved filtration on the spatial accuracy of PAM. More specifically, the SOH model enabled accurate estimation of the amplitude of time-varying narrowband components, recovering, therefore, a weak broadband signal. Furthermore, it enables the generation of PAM maps of inertial cavitation activity that spatially coincide with the physical area within which cavitation nuclei can exist. By contrast, PAM maps obtained using

conventional comb filtration could erroneously indicate the occurrence of inertial cavitation activity several mm beyond the physical boundaries within which cavitation can exist (narrowband comb filters), or significantly underestimate the intensity and extent of inertial cavitation activity leading to misinterpretation of the onset of inertial cavitation (wideband comb filters). We can therefore speculate that PAM maps generated using the SOH model are more likely to accurately describe the location, intensity and extent of the different ultrasound bio-effects associated with narrowband or broadband acoustic sources, such as opening of the blood brain barrier or drug release.

In conclusion, the proposed SOH method is expected to enable significant improvements in the spatial accuracy of PAM as a tool for real-time monitoring of ultrasound therapies. The proposed method could also find application in conventional active ultrasound imaging or other acoustic signal processing requiring separation of a low-amplitude broadband signal from a high-amplitude narrowband component, or vice versa.

3.6 REFERENCES

Chitnis, P.V., Farny, C., Roy, R.A., 2015. Singular value decomposition: A better way to analyze cavitation-noise data. J. Acoust. Soc. Am. 137, 2253–2253.

Choi, J.J., Coussios, C.-C., 2012. Spatiotemporal evolution of cavitation dynamics exhibited by flowing microbubbles during ultrasound exposure. J. Acoust. Soc. Am. 132, 3538–3549.

Coviello, C., Kozick, R., Choi, J., Gyöngy, M., Jensen, C., Smith, P.P., Coussios, C.-C., 2015. Passive acoustic mapping utilizing optimal beamforming in ultrasound therapy monitoring. J. Acoust. Soc. Am. 137, 2573–2585.

Haqshenas, S.R., Saffari, N., 2015. Multi-resolution analysis of passive cavitation detector signals. J. Phys. Conf. Ser. 581.

Jensen, C.R., Ritchie, R.W., Gyöngy, M., Collin, J.R.T., Leslie, T., Coussios, C.-C., 2012. Spatiotemporal monitoring of high-intensity focused ultrasound therapy with passive acoustic mapping. Radiology 262, 252–261.

Kwan, J.J., Graham, S., Myers, R., Carlisle, R., Stride, E., Coussios, C.C., 2015. Ultrasound-induced inertial cavitation from gas-stabilizing nanoparticles. Phys. Rev. E 92, 23019.

Kwan, J.J., Myers, R., Coviello, C.M., Graham, S.M., Shah, A.R., Stride, E., Carlisle, R.C., Coussios, C.C., 2015. Ultrasound-Propelled Nanocups for Drug Delivery. Small 11, 5305–5314.

Lake, D., 1999. Efficient Maximum Likelihood Estimation for Multiple and Coupled Harmonics. ARL-TR-2014.

Myung, I.J., 2003. Tutorial on maximum likelihood estimation. J. Math. Psychol. 47, 90–100.

Whipps, G., 2003. Coupled harmonics : estimation and detection. The Ohio State University.

Zivanovic, M., Gonzalez-Izal, M., 2012. Nonstationary Harmonic Modeling for ECG Removal in Surface EMG Signals. IEEE Trans. Biomed. Eng. 59, 1633–1640.

CHAPTER



IMPROVED PASSIVE ACOUSTIC MAPPING OF CAVITATION FOLLOWING VASCULAR EXTRAVASATION

4.1 INTRODUCTION

The aim of the present chapter is to enable testing and quantification of the improvements in spatial resolution derived from the novel beamforming and sum-of-harmonics filtration methods presented in Chapters 2 and 3 during passive acoustic mapping of cavitation activity.

In order to achieve this, an experimental design was necessary that provided a clear ground truth as to the location and extent of cavitation activity over length scales comparable to the spatial resolution of the new RLPB beamformer. Fluorescent sub-micron cavitation nuclei were made to flow inside a pre-formed in agar 1 mm in diameter channel and exposed a first time to focussed ultrasound above their cavitation threshold, causing cavitation inside the channel and extravasation into the porous agar matrix of these nanoparticles potentially by a combination of cavitation-induced microstreaming and microjetting. Following flushing of the channel, a second focussed

ultrasound exposure was used to excite extravasated particles, whilst subsequent optical imaging made it possible to identify the location and extent of the fluorescent particles in the agar matrix. Passive Acoustic Maps (PAM) acquired during the first ultrasound exposure should describe cavitation sources bounded by the channel wall, whilst PAM during the second exposure should correlate spatially with the fluorescent regions, providing a ground truth for the location and extent of cavitation activity in both cases.

The work presented in this chapter is the result of collaboration with Catherine Paverd, a fellow DPhil student within the BUBBL group. More specifically, the *in vitro* experimental setup presented in section 4.4 was originally designed by post-doctoral researcher Dr Delphine Elbes for experimentation in spinal disc fractionation. It was subsequently modified by DPhil student Catherine Paverd in order to enable bi-static cavitation mapping during and following cavitation-mediated extravasation *in vitro*, using existing RCB post-processing algorithms with conventional band-pass filtration. The design of the experimental setup and procedure, the conduct of a number of experiments under varying ultrasound exposure conditions described in section 4.4, and all data collection was therefore performed by Catherine Paverd, whose contribution is explicitly and gratefully acknowledged. Those datasets have been subsequently re-analysed by the author of the present DPhil thesis to enable assessment and quantification of the improvements in spatial resolution afforded by the novel filtering and beamforming techniques presented in Chapters 2 and 3 of this thesis.

4.2 EXPERIMENTAL METHODS

4.2.1 FLUORESCENT SUB-MICRON CAVITATION NUCLEI

A recently developed polymeric sub-micron cavitation agent, known as a nanocup, is used in the present work to lower the cavitation threshold and enable nucleation of cavitation in an agar matrix of approximate pore size 500 nm (Narayanan et al., 2006). More specifically, this novel particle is a polymeric, biocompatible, cup-shaped nanoparticle of tunable size ranging between 100nm and 800nm, whose design has been optimised to entrap and stabilise a nano-scale bubble in a cup-shaped cavity (James J. Kwan et al., 2015; J. J. Kwan et al., 2015).

Above a cavitation threshold pressure, the bubble expands, typically detaches from the nanocup and collapses inertially, exclusively generating broadband acoustic emissions that allow their localisation via PAM (Kwan et al., 2016, 2016). Previous work has demonstrated that nanocups not only cause inertial cavitation upon ultrasound exposure, but are actively transported by the combination of microstreaming and acoustic radiation force generated by neighbouring cavitating nanocups. Furthermore, previous work has also shown that nanocups are able to sustain inertial cavitation activity for several minutes of ultrasound exposure at modest pressure amplitudes typically achievable by diagnostic ultrasound systems (James J. Kwan et al., 2015). The broadband acoustic emissions generated due to inertially cavitating nanocups inside and outside the vasculature can then be used to map the location of the nanocups using PAM.

There is a direct relationship between the size of the nanocup, the size of the bubble attached to it, and the pressure threshold for the stabilized nanobubble to inertially cavitate (Fig. 4.1) (J. J. Kwan et al., 2015). For the present work, nanocups of

mean size 400 nm were chosen, as they exhibit an inertial cavitation threshold of < 1.5 MPa at 0.5 MHz and <2 MPa at 1.6 MHz.

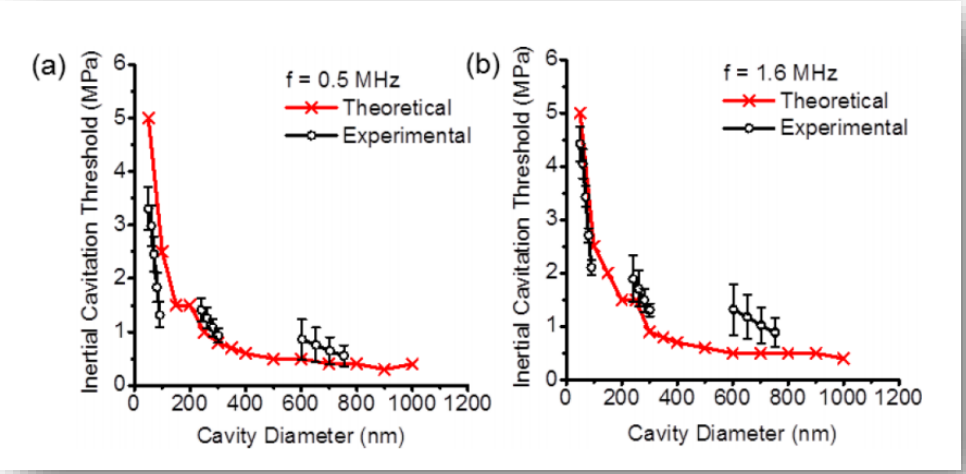


Figure 4.1 Inertial cavitation thresholds predicted numerically and determined experimentally at (a) 0.5MHz and (b) 1.6MHz. Each experimental point represents the mean and standard deviation across three measurements (Reproduced from (J. J. Kwan et al., 2015)).

4.2.2 Experimental Apparatus

As illustrated in Fig. 4.2, two 0.5MHz spherically focused, single-element ultrasound transducers (H107 SN27; Sonic Concepts, Bothell, WA, USA) with active diameter 64mm, focal length 62.6mm, and a central rectangular cut-out of dimensions 18x45mm^2 are fitted in a holder to ensure confocal alignment and placed in a large water tank of degassed, filtered water. Each transducer is connected through a matching network to a function generator (33250A 30 MHz function/arbitrary waveform generator, Agilent Technologies, Santa Clara, CA), and it is driven on burst mode (2000-cycles sinusoid signal of burst period 200ms), at either its fundamental frequency (0.5MHz) or the third harmonic (1.5MHz). Signal amplification takes place through two

55dB power amplifiers (E&I, A300, Rochester, NY, USA), each connected to one of the HIFU transducers. The HIFU transducers are driven either at their fundamental frequency, 0.5MHz, or the third harmonic, 1.5MHz. The choice between the two frequencies is based on two criteria, the likelihood of inertial cavitation and the probability of generation of harmonic components. The lowest of the two frequency favours inertial cavitation at lower pressures, while generation of harmonics due to nonlinear propagation is limited. On the other hand, a driving frequency of 1.5 MHz requires higher pressure amplitudes for cavitation to occur, and at the same time the generation of a stronger harmonic signal due to nonlinear propagation is favoured. In the cases now that increased driving frequency and pressure amplitude are combined result in increased nonlinearity. Subsequent reflections or scattering from interfaces such as channel walls of this nonlinear signal will result in harmonic components backpropagating towards the array. Additionally, the 1.5MHz driving frequency and its harmonics are closer to the bandwidth of the array, namely between 4MHz and 11MHz, and the likelihood of recording these harmonic emissions is higher compared to the case of the 0.5MHz driving frequency. The recorded harmonic components will thus enable testing of the performance of the SOH filtration method in extracting broadband signals.

Two Verasonics L11-4v linear array transducers (central frequency 6.25 MHz, 128 elements, pitch 0.298-0.302mm, sensitivity −64.5 to −59.5 dB, elevation focus 15-25 mm, Verasonics, Inc., Redmond, WA) are placed at the rectangular cut-outs of the HIFU transducers. Coaxial alignment of each array with the corresponding HIFU transducer is ensured. The multi-element array transducers are connected to the Verasonics Vantage Research Ultrasound System (Verasonics, Inc., Redmont, WA) that

allows passive simultaneous recording of the acoustic signals from all elements on the two arrays to be subsequently processed for the generation of PAM maps.

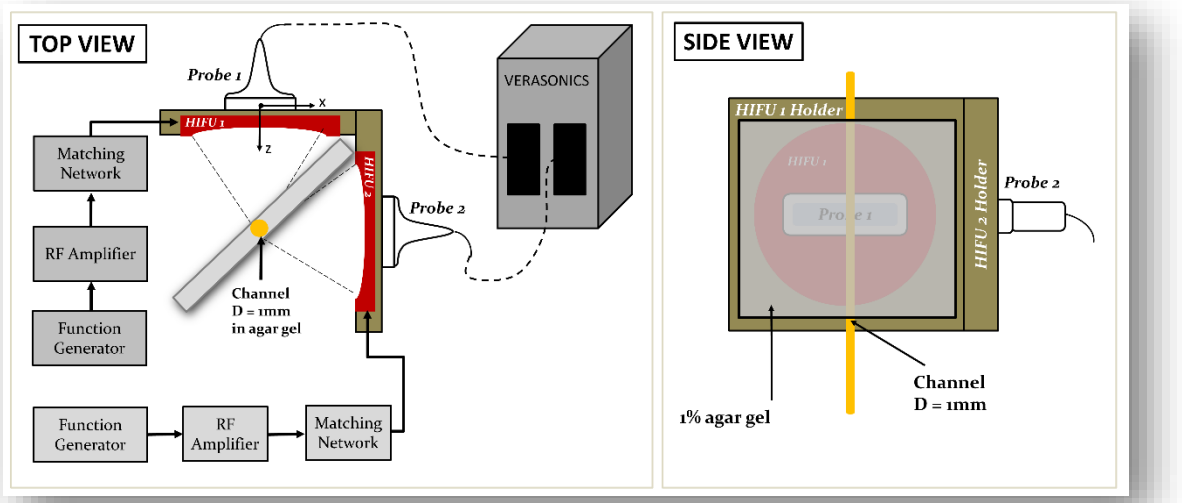


Figure 4.2 Experimental setup, top view (left figure) and side view (right figure) involving a 1% agar gel with a pre-formed channel containing flowing nanocups, placed at the focus of two confocally aligned orthogonal HIFU transducers. Each HIFU transducer is co-aligned with a 4–11 MHz linear array of 128 elements for passive recording of acoustic emissions. These emissions are filtered with either a comb filter or the SOH model, and processed using PAM combined with either RCB or RLPB as a beamforming technique to provide maps of sources of acoustic emissions.

An agar-based porous gel with a pre-formed wall-less channel is placed at the focus of the two HIFU transducers. The choice of the agar gel composition is based on the fact that it exhibits pore sizes similar to those expected in cancerous vasculature, and the size can be easily adapted by choosing the right concentration of agar in the gel. In the experiments presented here the agar gel is degassed and consists of 1% agar and results in pores in the range 500-800 nm.

4.2.3 EXPERIMENTAL PROCEDURE

The experimental procedure is presented schematically in Fig. 4.3, and is intended to enable simultaneous mapping and optical imaging of cavitation activity over well-defined spatial regions.

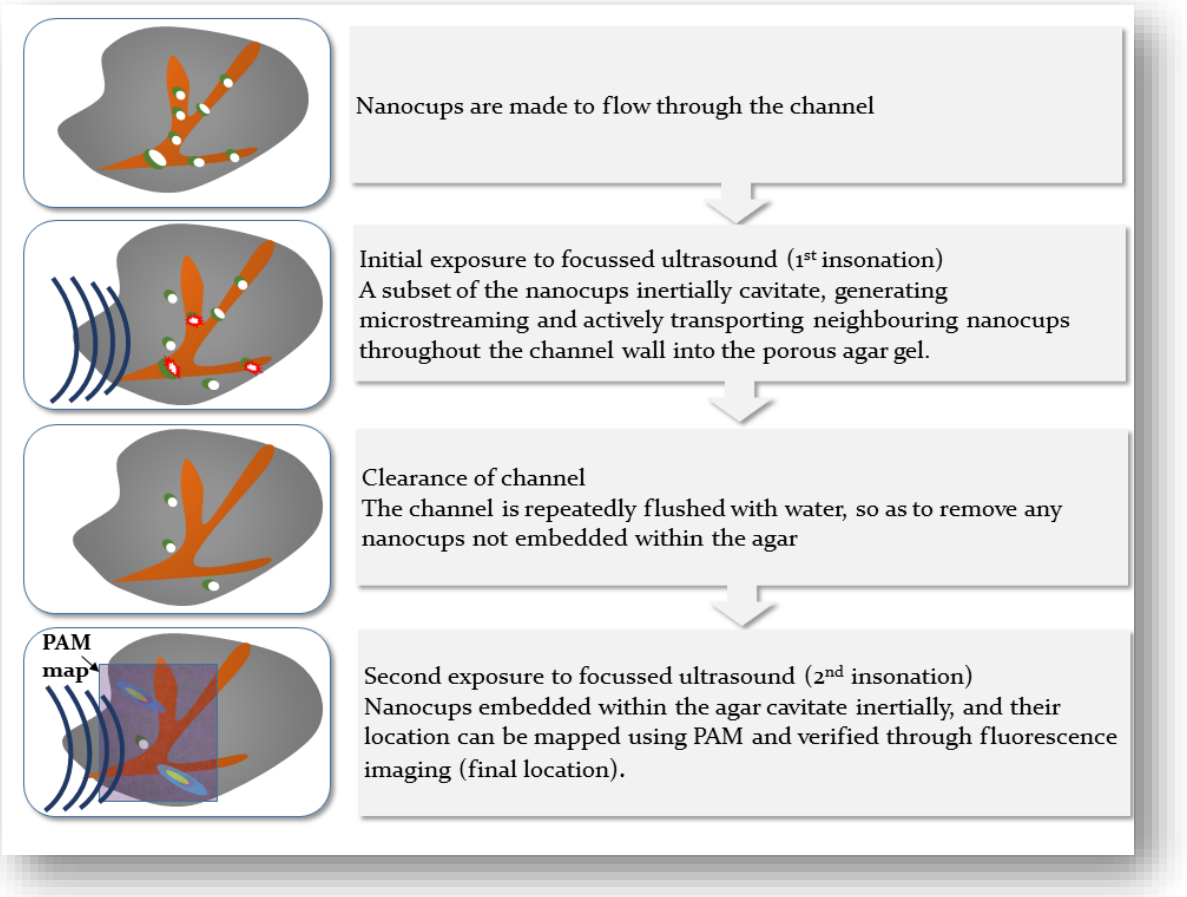


Figure 4.3 Experimental procedure used to initially cause and map inertial cavitation within the channel upon the first insonation, followed by inertial cavitation and mapping outside the channel that can be directly compared to fluorescence imaging of cavitation nuclei.

At the beginning of the experiment nanocups of mean diameter 400nm and concentration 2mg/ml are flown through this channel at 0.3ml/min flow rate, and they are exposed to ultrasound. Sources of inertial cavitation activity in the channel are

mapped using PAM. At the end of the sonication the channel is cleared by flowing degassed deionised water for 30min. Then, a second sonication takes place, and it is assumed that the nanocups that have been actively transported due to ultrasound (first sonication) from the channel into the gel are able to continue to cavitate. PAM maps of inertial cavitation, now expected to occur only outside the channel or at the boundaries of the channel assuming extravasation has occurred, are generated.

Several acoustic parameters have been investigated and are summarised in Table 4.1. The rationale behind the choice of these parameters is different between the two stages of the experimental procedure. During the first insonation the goal is to induce inertial cavitation levels that will result in maximisation of the extravasation. In the second stage of the experiment, i.e. after the channel clearance, the goal is to induce inertial cavitation of the nanocups extravasated.

Taking into consideration the cavitation threshold for inertial cavitation of nanocups at each frequency, different excitation sequences have been investigated. An estimation of the cavitation threshold of nanocups can be obtained by (J. J. Kwan et al., 2015). Additional experiments have been performed[1] to determine the cavitation threshold at each driving frequency of the nanocups participating in these experiments. At different pressures, the signal-to-noise ratio on PAM maps has been calculated by comparing the energy at a region where cavitation is expected to occur to the energy at a region of expected noise. Although cavitation might start occurring at a certain pressure, the criterion for determining the cavitation threshold was stabilisation of the signal-to-noise ratio, which occurs at higher pressures and ensures high levels of broadband emissions and high probability of sustained cavitation activity. Therefore,

[1]These experiments were designed and performed by DPhil student Catherine Paverd as part of her DPhil project.

the suggested cavitation thresholds are 1.4MPa at 0.5MHz, and 2.5MPa at 1.5MHz. It is also observed that these values are close to the values reported in (J. J. Kwan et al., 2015). Considering the above pressure thresholds for cavitation of nanocups and the pressure field of the two HIFU transducers, an estimate of the area, in the same plane as that of the imaging transducers, within which cavitation activity is expected, can be calculated and it is presented in Table 4.1. This area consists of the main focus and potentially areas at the sidelobes in which the cavitation threshold of nanocups has been exceeded. The dimensions of the main focus above the cavitation threshold are also presented in a separate column in Table 4.1. Considering the dimensions of the channel (i.e. 1mm in diameter), and assuming alignment of the HIFU focal region with the channel, there is a clear overlap of the two areas. This overlap allows both cavitation to occur inside the channel during the first insonation, and nanocups that have been extravasated in the area surrounding the channel to cavitate as well during the second insonation, at least along one of the directions of the focal region (i.e. the longest one).

The driving frequency and peak negative pressure at the focus, common for both transducers, for the first and second insonation, as well as the size of the area and the dimensions of the main focus, in which the cavitation threshold of nanocups is exceeded, for each set of parameters are summarised in Table 4.1.

As far as the cavitation thresholds of the agar gel are concerned, additional control experiments have been performed[2] using either deactivated nanocups, i.e. nanocups that have not been exposed to air and therefore, not able to cavitate, or fluorescent microspheres 300nm in size. The exposures parameters are the same as in Set 1 and Set 2, as these are presented in Table 4.1. In these experiments, no cavitation

[2]These experiments were designed and performed by DPhil student Catherine Paverd as part of her DPhil project.

has been observed on the PAM maps, both in the first and second insonation. Subsequent brightfield microscopy of the channel demonstrated no channel deformation reinforcing the conclusion that at these exposure parameters the cavitation threshold of the agar has not been exceeded. However, as far as the parameters in Set 3 are concerned, it is expected that the cavitation threshold of the agar has been approached, if not exceeded. Since no control experiments are available for these exposure conditions, it should be noted that cavitation activity observed might be a combination of cavitating nanocups and regions of the agar gel.

Table 4.1 Driving frequency and pressure amplitude during the first and second insonation for each experimental set presented in this section.

# Experiment	Parameters: Frequency Pressure (PNP)	Area (mm^2) above cavitation threshold of nanocups	Dimensions of main focal region
Set 1			
1st Insonation	0.5MHz 1.6MPa	0.75	2.2mm x 0.4mm
2nd Insonation	0.5MHz 1.6MPa	0.75	2.2mm x 0.4mm
Set 2			
1st Insonation	1.5MHz 3.5MPa	0.18	1mm x 0.3mm
2nd Insonation	0.5MHz 1.6MPa	0.75	2.2mm x 0.4mm
Set 3			
1st Insonation	0.5MHz 3.5MPa	8.22	5mm x 1.2mm
2nd Insonation	1.5MHz 6MPa	0.75	1.6mm x 0.4mm

Assessment of extravasation is performed optically using fluorescent microscopy. The nanocups are fluorescently tagged, and as soon as the experimental procedure is completed, the channel in the agar gel is cut transversely and in cross section, and is image by fluorescence microscopy (Nikon, TI Eclipse microscope, TRITC filter).

4.2.4 MAPPING OF CAVITATION ACTIVITY

At this point it is important to emphasize that the use of two confocal HIFU transducers makes it possible to limit the region over which the pressure exceeds the inertial cavitation threshold to a size comparable to the channel and the perivascular region.

Similarly, the use of two arrays at a 90^{o} angle configuration makes it possible to significantly improve the spatial, and in particular the axial resolution of PAM. By generating PAM maps from two linear arrays perpendicular to each other for mapping of acoustic activity taking place at the centre of this configuration, the axial resolution of one of the arrays coincides with the transverse resolution of the other array. Therefore, the resulting PAM resolution achieved by the combination of the two probes is expected to be significantly improved compared to the PAM maps generated using the signal recorded by a single array of detectors. However, it is apparent that this setup configuration, despite its profound advantages is not clinically applicable. Moving on to more clinically relevant conditions, a single array is expected to be used, and the main challenge associated with this transition is the poor axial resolution of PAM. As a reference point it should be noted that the theoretical limits for axial and transverse PAM resolution for the experimental setup presented in this chapter are approximately

7mm and 0.5mm respectively. The aim of the present work is to assess the improvement of PAM resolution for detection and localisation of acoustic sources due to the combination of more sophisticated filtering and beamforming approaches, during both the first and the second insonation when either the dual or single array configuration is used. Specifically for the case of a single array of detectors, the PAM maps generated using the dual array configuration, along with microscopy images, will serve as the ground truth for verification of the location of sources of inertial cavitation, and subsequent assessment of the observed changes in resolution.

4.2.5 SIGNAL PROCESSING AND BEAMFORMING

The RF data recorded by either one or both arrays is initially filtered with a high-pass filter of cut-off frequency equal to 0.1MHz to remove the DC offset. Subsequent filtering for the isolation of the signal-of-interest, in this case the broadband component, indicative of inertial cavitation, is performed using either a comb filter or the proposed SOH model. PAM maps of the filtered RF data are generated by using one of the two data-adaptive beamforming algorithms, i.e. RCB or the new proposed RLPB. The tree diagram presented in Fig. 4.4 demonstrates the steps described above, and the combination of the different filtering and beamforming methods for PAM.

Regarding filtering, a choice between a comb filter and the SOH model is made. The comb filter is implemented as a series of band-stop filters, each of them centred at one of the harmonics of the driving frequency for all the harmonic frequencies possibly present within the bandwidth of the recorded signal. The bandwidth of each filter is 0.1MHz and 0.05MHz for the bandpass and bandstop frequency zones respectively, and the attenuation in the stopband is 60dB. The criterion for the choice of the filter

bandwidth was increased harmonic signal rejection and preservation of the broadband signal of interest. For this purpose, the power spectrum of an initial frame of RF data was studied both at 0.5MHz and 1.5MHz, and the -3dB frequency band of the fundamental frequency was calculated. The bandstop frequency zone width was then defined as approximate five times the width of the -3dB frequency band, namely 0.05MHz for both driving frequencies to ensure adequate harmonic signal rejection.

As far as the SOH model is concerned, the parameters to be chosen are the number of cycles per segment and the order of the polynomial used to approximate the changes in the amplitude. As has been demonstrated in section 3.3 a combination of a second order polynomial with 8 cycles per segment provides a good compromise between signal-of-interest detection performance and real-time execution.

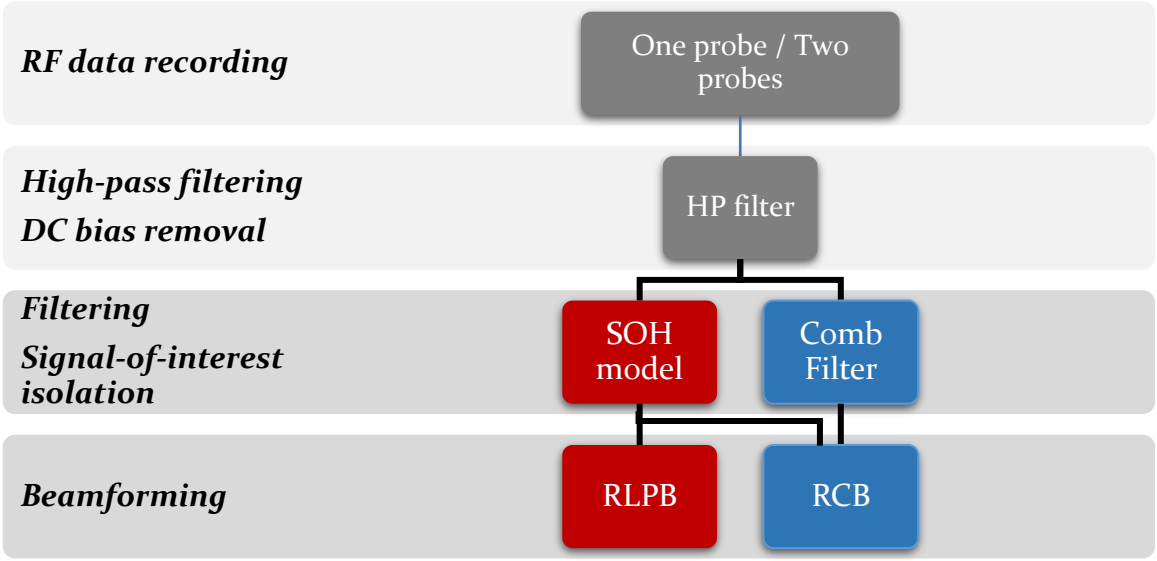


Figure 4.4 Steps of processing the passively recorded signals by the elements of the linear arrays in order to generate PAM maps of sources of acoustic emissions. The different combinations of filtering and beamforming approaches are also demonstrated. The methods enclosed in blue rectangular boxes represent the currently used approaches, while the red boxes correspond to the proposed in this thesis methods.

As far as beamforming is concerned, maps corresponding to approximately 60μsec of ultrasound exposure at a sampling frequency of 25MHz are generated. Regardless of beamforming algorithm, the array element positions need to be determined. For the two-array configuration, one of the main challenges is to define the relative positions of the elements of the first array with respect to the second. Such calibration is important since minimisation of such an error would subsequently not require a large value of ε in PAM processing to account for it, and, therefore, interference suppression would be improved.

To achieve this with the data available, B-mode images of the channel were generated by each array individually (two independent coordinate systems are considered at this point). Co-registration of the two images in the same coordinate system is then performed in order to determine the element positions, as demonstrated in Fig. 4.5. However, this is not ideal since it assumes that the two arrays are strictly orthogonal to each other, and does not account for small relative deviations in pitch and yaw. Therefore, accurate calculation of the element positions could be achieved by using multiple (at least three) fiducial markers in the registration of the B-mode images, and this will be explored in future work.

A second parameter that needs to be defined in both beamforming algorithms is the ε parameter, which allows fluctuations in the steering vector to account mainly for array calibration issues. The effect of this parameter is expected to be different in the two beamformers, and depending on its value different levels of interference suppression are achieved. Since a compromise needs to be made between interference suppression ability and array calibration issues correction, a value smaller than 20 should be used, as suggested by the results presented in Chapter 2. A coarse optimisation of the parameter ε has been performed at the beginning of each

experiment, and ε was allowed to take values equal to 5, 10, 15, and 20. The highest value of ε achieving correct localisation of acoustic activity, i.e. inside the channel, was chosen in order to allow at the same time maximum possible array element positions and calibration errors correction.

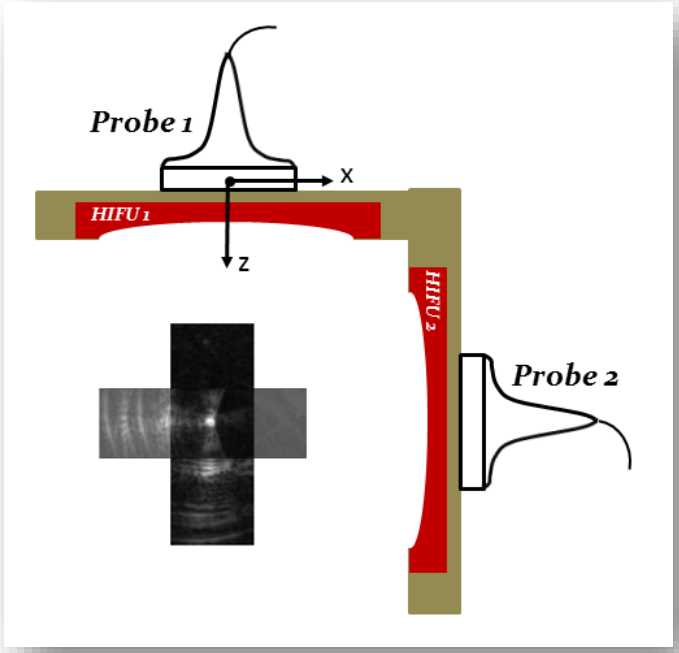


Figure 4.5 Linear arrays element positions definition in a common coordinate system by co-registration of the B-mode images of the channel, recorded by the two arrays.

4.3 EXPERIMENTAL RESULTS

The results presented in this section are organised according to the different exposure conditions summarised in Table 4.1. For each experiment PAM maps during the first (nanocups flow through the channel) and second insonation (post clearance of the channel) are generated for each array individually (probe 1 and probe 2), and for the combination of the two arrays (both probes). The PAM maps corresponding to the dual array configuration during the second insonation, where extravasation is mapped, are also overlaid with the fluorescent microscopy images to directly correlate cavitation

activity observed on PAM with extravasated fluorescent nanocups observed under the microscope. Additionally, different combinations of the PAM method components, namely filtering and beamforming methods, are also considered for each experimental set, as previously demonstrated in Fig. 4.4.

The aim of the present analysis of the RF data is dual; to assess the accuracy of PAM in localising sources of inertial cavitation initially inside and consecutively outside the channel depending on the filtering and beamforming algorithm chosen, and to evaluate the performance of PAM under more clinically relevant conditions, i.e. one array used instead of two, in estimating the location and extent of cavitation.

Set 1 (First insonation at 0.5MHz, Second insonation at 0.5MHz)

PAM analysis of selected RF data corresponding to this set of experiments for both first and second insonation is presented in Fig. 4.6 and 4.7. For the case of the first insonation it is expected that the mapped cavitation activity will be primarily contained within the boundaries of the channel, denoted by the black circle, unless extravasation has occurred.

Looking at the PAM resutls with both arrays using band-pass filtration and the RCB beamformer (Fig. 4.6 row 1, column 3), some cavitation activity takes place beyond the walls of the channel. By applying the SOH model (Fig. 4.6 row 2, column 3), no siginificant improvement is observed, suggesting that the choice of filtering approach in this particular situation does not affect the performance of PAM noticeably. This is hardly suprising: at 0.5 MHz, no significant harmonic generation is expected within the bandwidth of the PAM array (4-11 MHz), and application of a data-adaptive filtering approach is, therefore, not expected to significantly improve the performance

of PAM, as long as the energy of the first harmonic is adequately removed. In this situation, the spatial resolution of the PAM maps is primarily dictated by the point spread function of the RCB beamformer.

However, by adopting the RLPB beaformer (Fig. 4.6 row 3, column 3), cavitation activity is more concentrated inside the channel compared to RCB. This strongly suggests that the spatial resolution of the PAM maps at 0.5 MHz excitation is indeed primarily dictated by the PSF of the beamforming algorithm.

These same observations hold true for the single-array results (Fig. 4.6, column 2), within the limitations of axial resolution afforded by the use of a single array. Filtration once again makes little difference, but, unlike RCB, use of RLPB seems to better confine the cavitation activity transversely to the array within the boundaries of the channel.

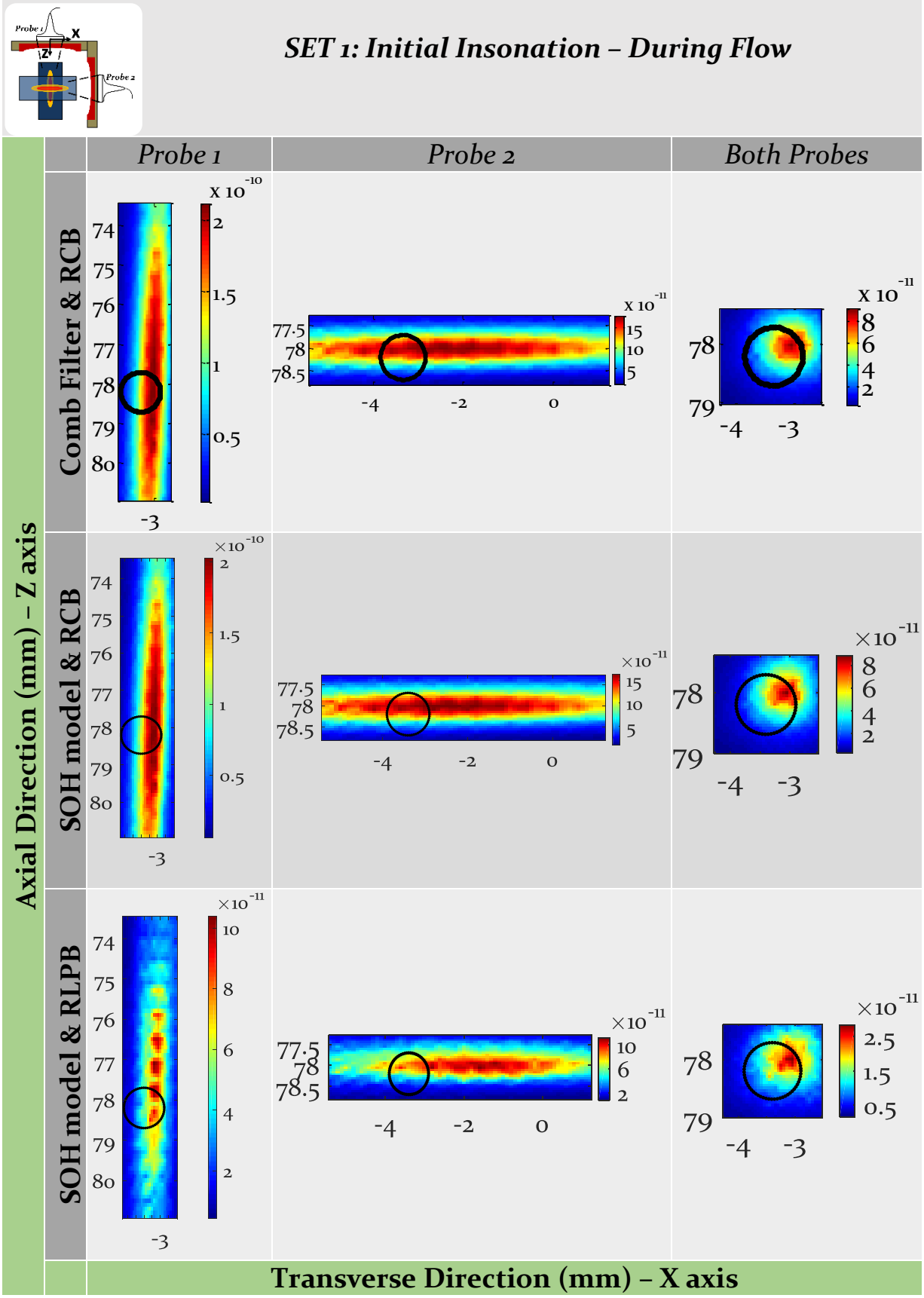


Figure 4.6 PAM maps corresponding to experimental set 1 during the first insonation (driving frequency = 0.5MHz) for single and dual array configurations and different combinations of filtering (comb filter or SOH model) and beamforming (RCB or RLPB) approaches. The location of the channel is indicated in each map with a black circle.

To further analyse the PAM maps and provide a quantitative comparison of the filtering and beamforming methods used in the signal analysis, assessment of correct localisation of sources of cavitation activity was performed based on two criteria. To achieve this, a region of interest is defined, and during the first insonation this region coincides with the channel area. First, the percentage of the PAM energy that is located inside the channel, and subsequently the complementary percentage corresponding to the energy outside the channel are calculated for each of the PAM maps in Fig. 4.6, and they are presented in the first column in Fig. 4.7. It is important to note at this point that only the energy on the PAM maps that is above 80% of the maximum energy observed, refered from now on as -1dB energy, is considered in the above calculation of the percentage. The rationale behind this choice is that maximum correlation between the energy on the PAM maps and the desired bioeffect is expected at the regions of maximum energy. In the case of the dual configuration, the combination of the SOH model and RLPB beamformer demonstrates that 100% of the -1dB energy is located inside the region of interest, outperforming the other two combinations of methods. In the single array configurations, the percentage of -1dB energy located inside the channel is significantly reduced. This result is expected due to the poor axial resolution, and the conclusions made after comparing the filtering and beamforming methods differ depending on the probe. To assess how the axial and transverse spatial resolution of the different combinations of methods affect the correct localisation of sources of cavitation, a second criterion has been employed, i.e. the area that the -1dB energy covers inside and outside the region of interest. The results that correspond to the PAM maps in Fig. 4.6 are presented in the second column of Fig. 4.7. Of special interest is the area outside the channel since it provides a measure of the false spatial extent of cavitation activity and, therefore, it is an indication of the source localisation error. In

experimental set 1, it seems that the area outside the channel with significant PAM energy is limited in the dual array configuration in all cases. However, in the single array configurations, it is clear that the SOH model along with the RLPB beamformer significantly outperform the other combinations, by covering less than 1/6 and ½ of the area that the other two combinations cover outside the channel in the case of probe 1 and probe 2 respectively.

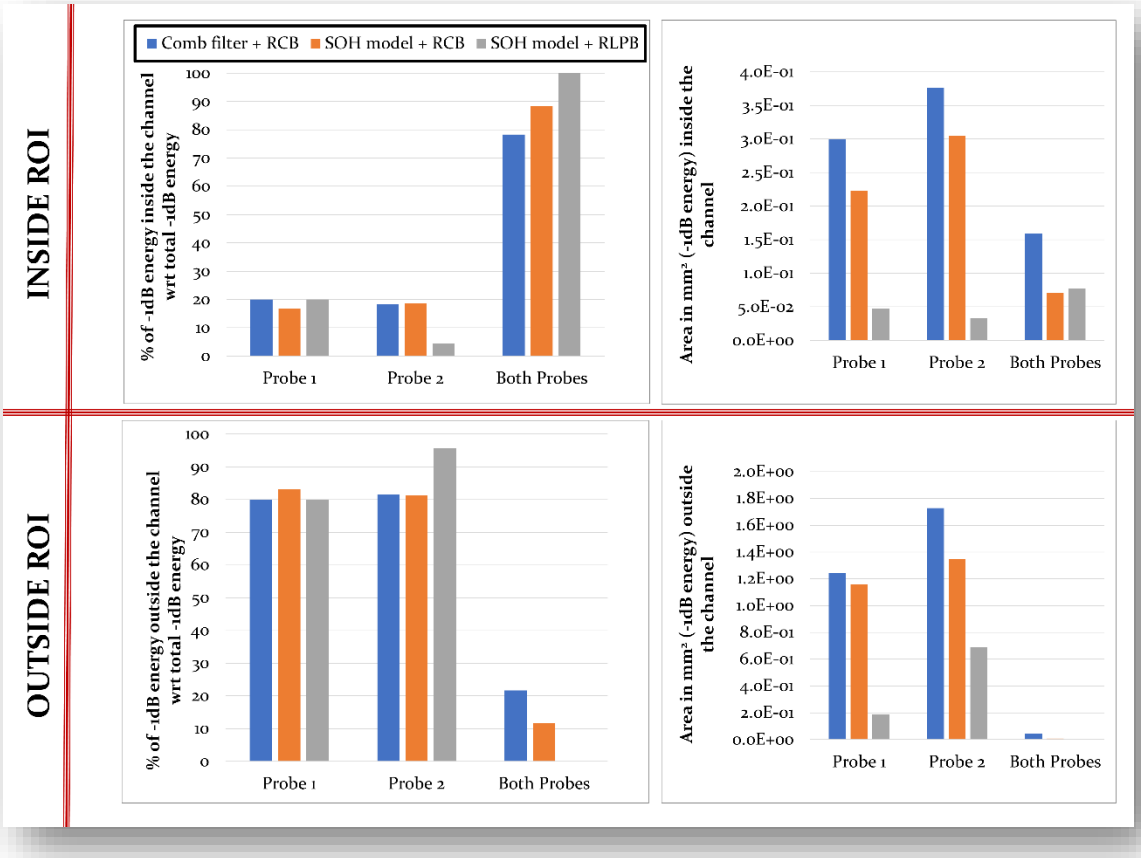


Figure 4.7 Quantitative analysis of the PAM maps corresponding to experimental set 1 during the 1st insonation. The percentage of the -1dB energy (i.e. energy on the PAM maps above the 80% of the maximum PAM energy displayed on the map) inside and outside the region of interest (i.e. the area of the channel) with respect to the total -1dB energy on the PAM maps is presented on the two left subfigures for all combinations of filtering and beamforming approaches, and for all array configurations. The two subfigures on the right present the area in mm^2 that the -1dB energy occupies inside (top subfigure) and outside (bottom subfigure) the channel for all possible combinations of filtering and beamforming methods, and all array configurations.

To justify further the choice of -1dB energy as a measure of quantitative comparison of the PAM maps, an additional comparison between the PAM maps of Fig. 4.6 has been performed based on the -3dB energy, i.e. the energy on the PAM maps that is above 50% of the maximum energy displayed on the map. These results are presented in Fig. 4.8. Comparing Fig. 4.7 and Fig. 4.8, it is concluded that in terms of energy inside and outside the region of interest, the -3dB criterion, in contrast to the -1dB criterion, does not provide any clear distinction between the different combinations of filtering and beamforming. As far as the area inside and outside the region of interest, both energy thresholds provide the same conclusions, and demonstrate an advantage of the SOH model combined with RLPB over the other combinations across all the examined array configurations. As a conclusion, since the two thresholds provide the same qualitative conclusions, it is safe to assume that the use of the -1dB energy threshold does not provide biased results and allows more clear comparison of the methods since the noise introduced in the calculation of energy is reduced.

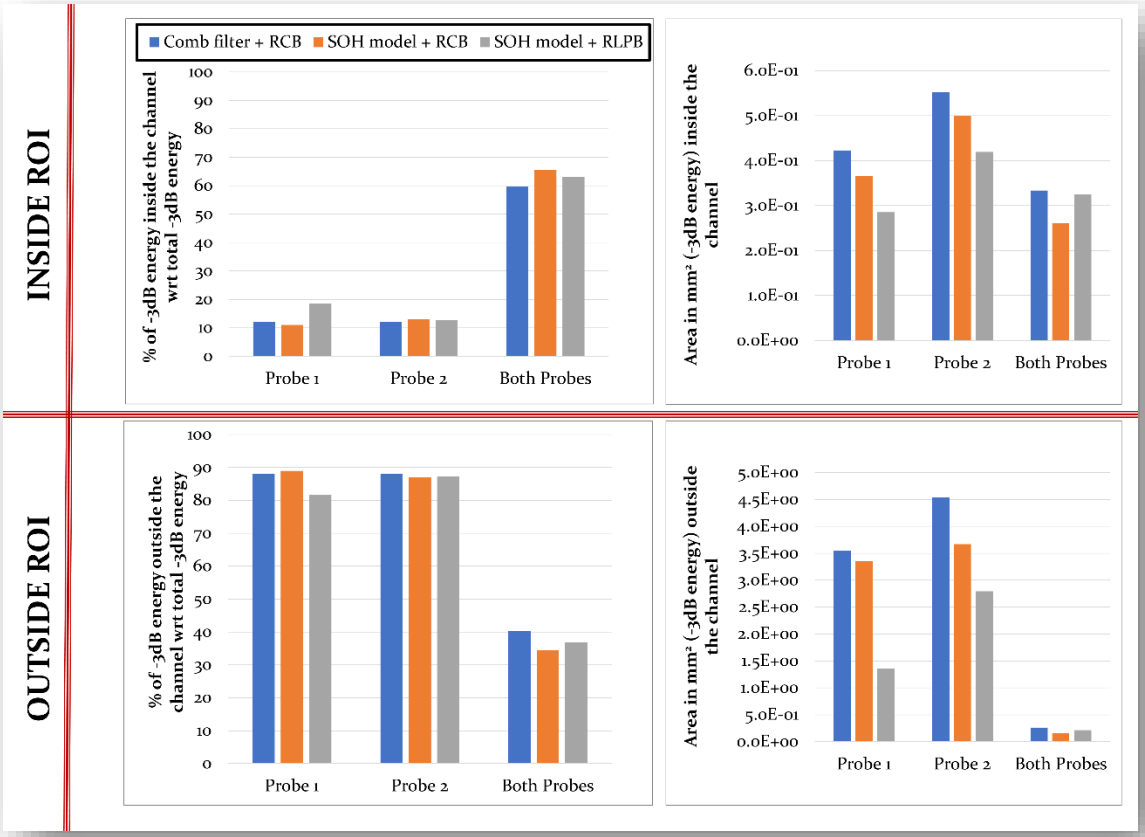


Figure 4.8 Quantitative analysis of the PAM maps corresponding to experimental set 1 during the 1st insonation. The percentage of the -3dB energy (i.e. energy on the PAM maps above the 50% of the maximum PAM energy displayed on the map) inside and outside the region of interest (i.e. the area of the channel) with respect to the total -3dB energy on the PAM maps is presented on the two left subfigures for all combinations of filtering and beamforming approaches, and for all array configurations. The two subfigures on the right present the area in mm^2 that the -3dB energy occupies inside (top subfigure) and outside (bottom subfigure) the channel for all possible combinations of filtering and beamforming methods, and all array configurations.

Proceeding, now, to the second insonation (Fig. 4.9), following flushing of the channel to remove all non-embeded nuclei, filtration alone is once again found to have minimal impact on the qualitative information provided by the cavitation maps. However, by contrast to Fig. 4.6, it can be noted that the estimated source energy on the PAM maps of Fig. 4.9 is significantly higher for the case of the SOH model compared to the comb filter. By studying the spectra of the filtered RF signals more closely (Fig. 4.10), two important observations are made. Firstly, the comb filter removes the energy at the fundamental frequency less efficiently compared to the SOH model, and secondly, a significant portion of the broadband energy at multiples of the fundamental frequency is removed when the comb filter is applied. This is due to the fixed number of stopbands defined in the comb filter, compared to the SOH model for which an initial optimisation step allows estimation of the number of harmonics present. The relative relationship between the remaining energy at the fundamental frequency erroneously considered as broadband energy, and the broadband energy erroneously removed due to fixed number of stopbands in the comb filter determines the relationship between the PAM source energy estimated using the comb filter or the SOH model. Looking at the filtered signals of Figure 4.10, SOH can be deemed to produce a more faithful representation of broadband source energy.

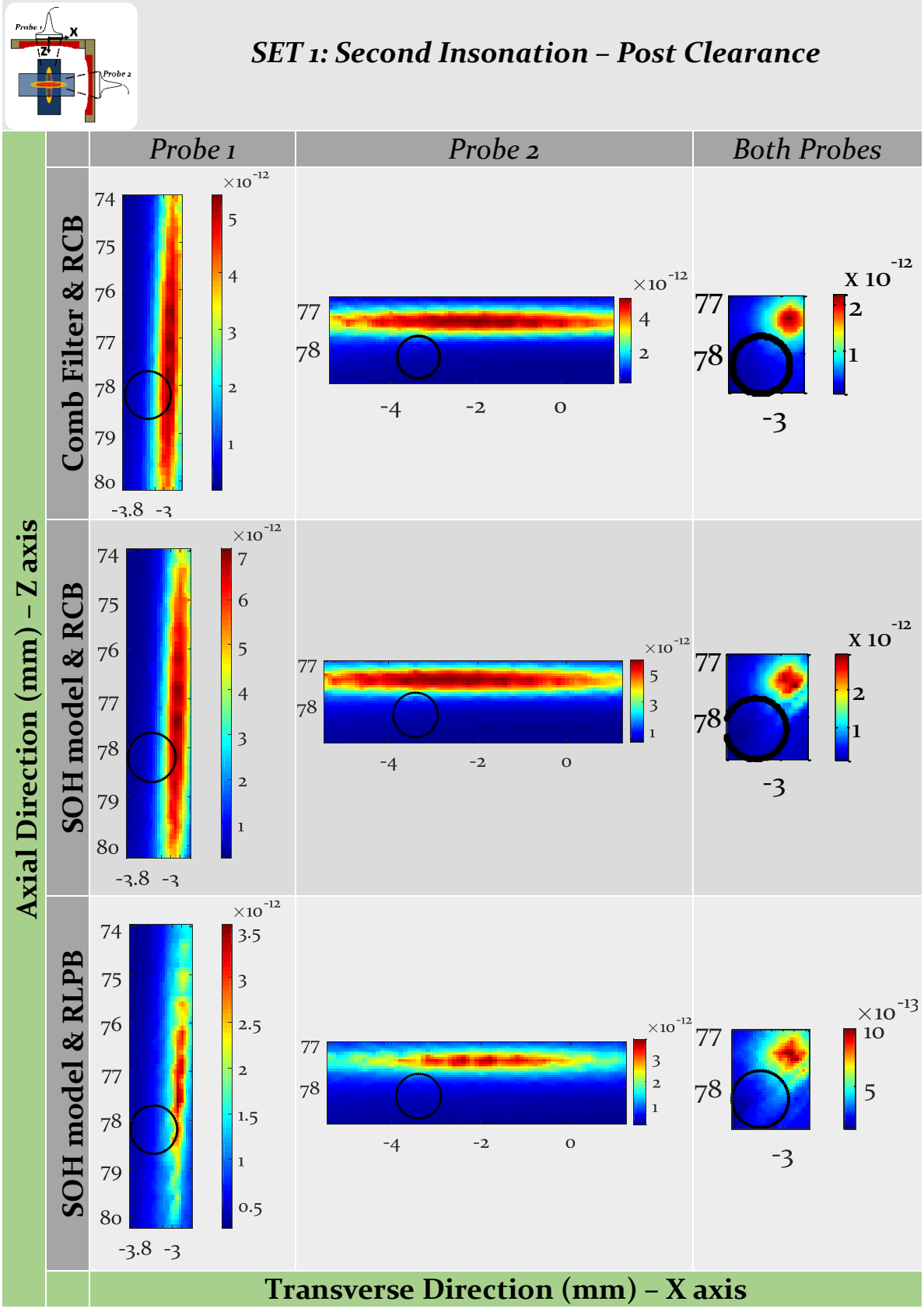


Figure 4.9 PAM maps corresponding to experimental set 1 during the second insonation, after channel clearance (driving frequency = 0.5MHz) for single and dual array configurations and different combinations of filtering (comb filter or SOH model) and beamforming (RCB or RLPB) approaches. The location of the channel is indicated in each map with a black circle.

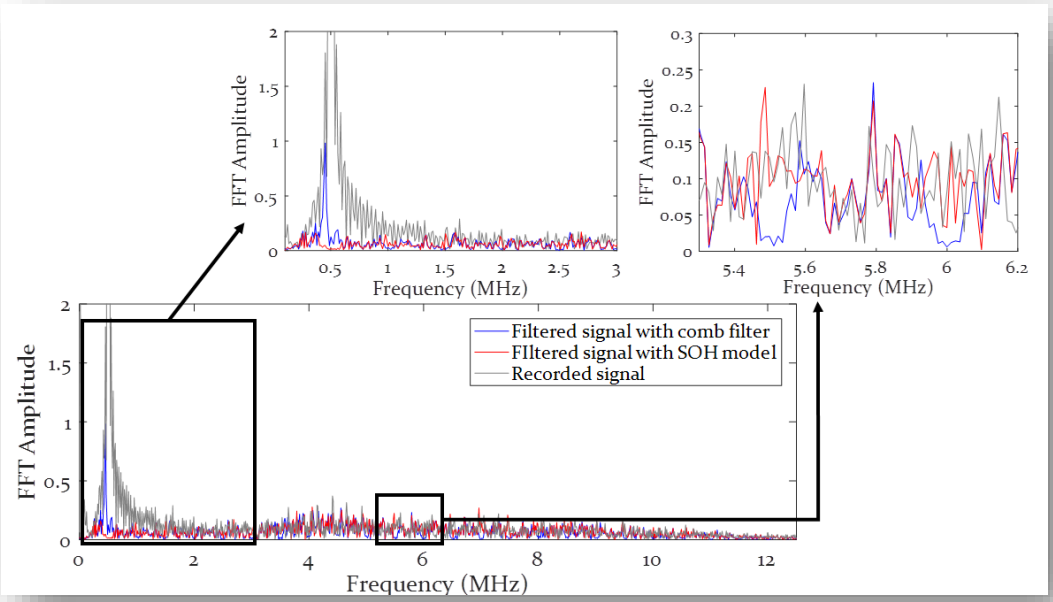


Figure 4.10 Spectral analysis of the RF signal recorded by the middle channel of probe 1 corresponding to the experimental set 1 during the second insonation, after being filtered with either a comb filter (bandwidth = 0.1MHz, order = 25) or the SOH model (polynomial order = 2, number of cycles = 8) for harmonic frequencies removal.

On the other hand, the choice of the beamforming algorithm clearly alters the performance of PAM (Fig. 4.9 rows 2 and 3) especially in the single array configurations. It is observed that the extent of the cavitation activity is significantly restricted when RLPB is applied, potentially allowing improved correlation between the PAM maps and the fluorescent microscopy image, which is indicative of the location of the extravasated nanocups. To further confirm this observation, Fig. 4.11 displays the PAM maps corresponding to either of the two arrays of detectors for the cases where the SOH model has been chosen as a filtering technique and either RCB or RLPB has been applied. The fluorescent microscopy image is overlaid with the PAM maps and -1dB contours have been drawn (white lines) in all the above cases indicating the extent of the regions of high acoustic activity, at this point defined as higher than 80% of the maximum value for each PAM map. For the first probe (top right subfigure in Fig. 4.11)

it is clear that RLPB outperforms RCB, as it is able to map activity only outside the channel and only towards the correct direction where inertial cavitation is expected to take place according to the microscopy images. By studying, now, the PAM maps generated by the second probe, similar conclusions can be drawn. More specifically, sources of inertial cavitation are correctly localised outside the channel by both RCB and RLPB. However, the extent of the cavitation region in the case of RLPB is significantly closer to the ground truth in terms of location compared to RCB, allowing better localisation and estimation of the extravasation caused.

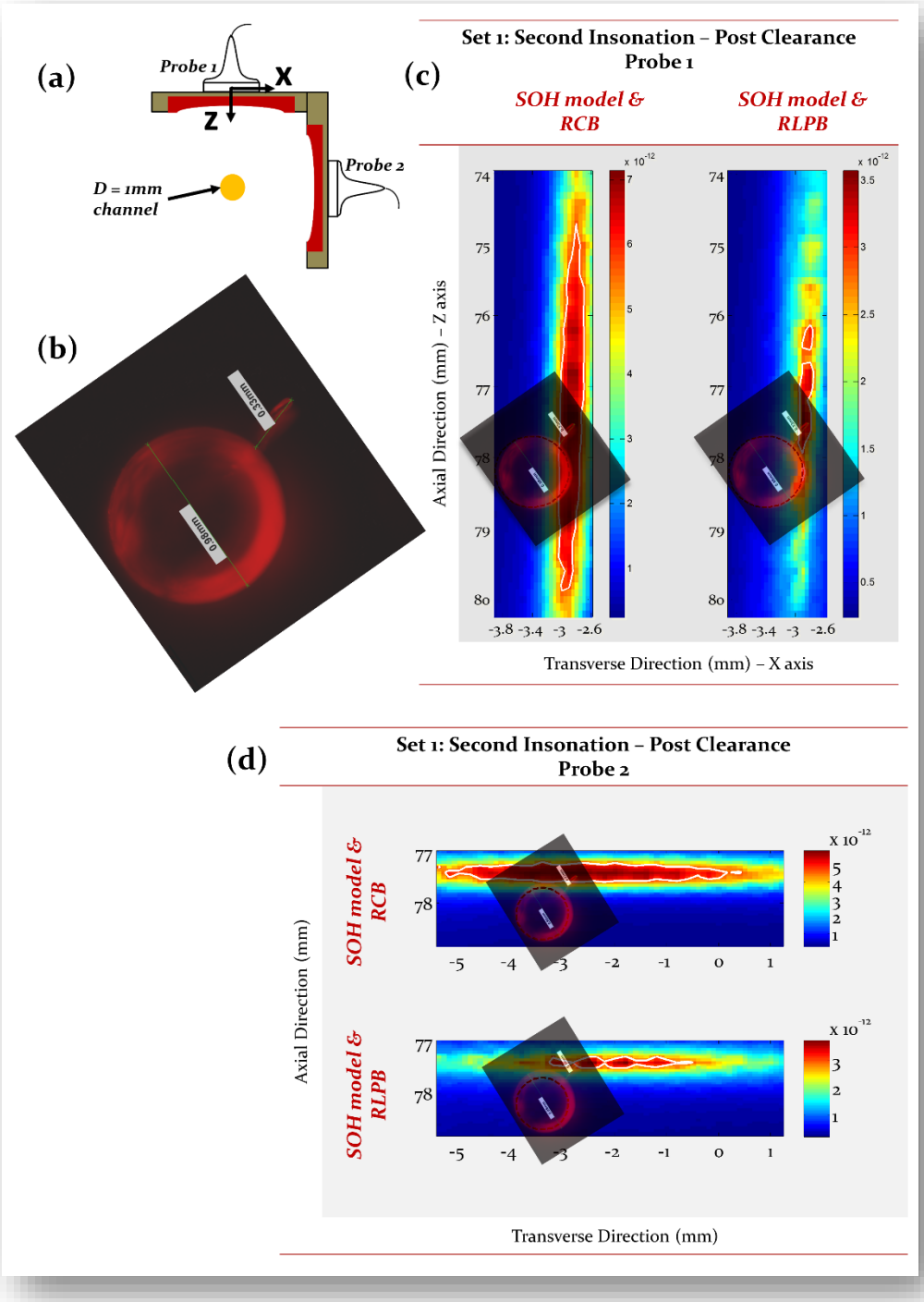


Figure 4.11 PAM maps corresponding to experimental set 1 during the 2nd insonation, after channel clearance (driving frequency = 0.5MHz) for the single array configurations (probe 1 in subfigure (c) and probe 2 in subfigure (d)). Fluorescent microscopy images are overlaid with the PAM maps to indicate the regions of extravasation. A magnified version of the fluorescent microscopy image is provided in subfigure (b). The RF data is filtered using the SOH model prior to PAM, and either RCB or RLPB are used as a beamforming technique. Contours corresponding to 80% of the maximum PAM energy for each map (-1dB contours) are displayed (white lines). The location of the channel is indicated in each map with a black dashed circle. A schematic of the experimental setup is presented in subfigure (a) to clarify the direction of the PAM maps in subfigures (c) and (d).

Quantitative analysis of the PAM maps in Fig. 4.9 requires the definition of a region of interest. In this part of the experiment, it is of interest to quantify the area of maximum energy on the PAM maps that correlates well with the fluorescent microscopy images, and it is located outside the channel region, which has been flushed with water and no nanocups, and therefore, no cavitation is expected in this region. Additionally, it is important to quantify the extent of the area that the -1dB energy occupies outside the region of interest, to assess the error in source localisation. The region of interest has been defined as a circle with centre determined by the location of maximum fluorescence and radius defined by the distance between the closest point on the channel wall and the location of maximum fluorescence. Making sure that the region of interest does not overlap with the channel area, the analysis presented for the 1st insonation is repeated here, and the results are presented in Fig. 4.12.

It is observed that in the case of the dual array configuration, no method combination seems to clearly outperform the others. Focussing on the single array configurations, it is observed that the combination of the SOH model and RLPB beamformer provide higher percentage of -1dB energy inside the region of interest compared to the other two combination, especially in the case of probe 1. Additionally, by observing the extent of the area of -1dB energy outside the region of interest, it is observed that in the case of the SOH model and the RLPB beamformer the extent is significantly reduced, constituting approximately 1/5 of the area that the other two combinations demonstrate. Finally, it is useful to note that in all cases the replacement of comb filtering with the SOH model does not provide a significant advantage, as it was also observed qualitatively in the PAM maps of Fig. 4.9.

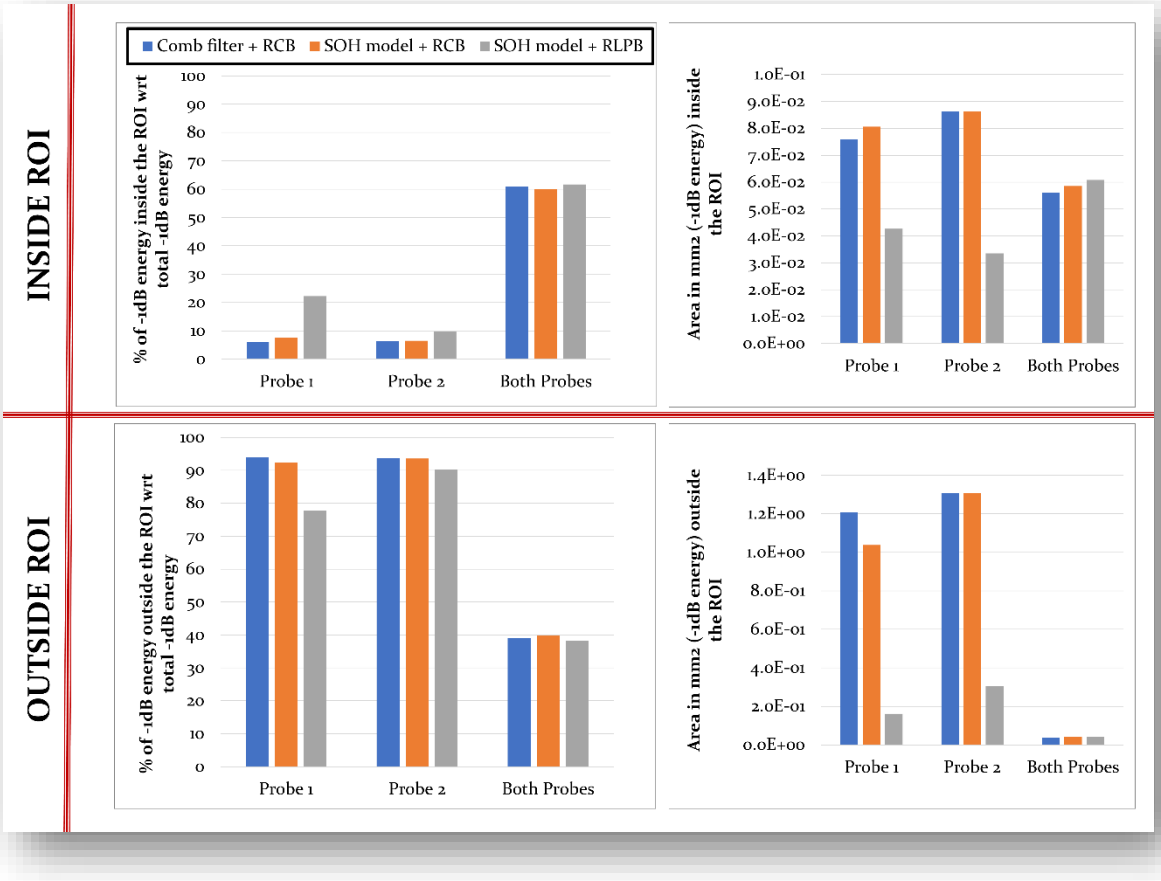


Figure 4.12 Quantitative analysis of the PAM maps corresponding to experimental set 1 during the 2nd insonation. The percentage of the -1dB energy (i.e. energy on the PAM maps above the 80% of the maximum PAM energy displayed on the map) inside and outside the region of interest (i.e. the area of increased fluorescence on the fluorescent microscopy images) with respect to the total -1dB energy on the PAM maps is presented on the two left subfigures for all combinations of filtering and beamforming approaches, and for all array configurations. The two subfigures on the right present the area in mm^2 that the -1dB energy occupies inside (top subfigure) and outside (bottom subfigure) the region of interest for all possible combinations of filtering and beamforming methods, and all array configurations.

Set 2 (First insonation at 1.55MHz, Second insonation at 0.5MHz)

Unlike the previous data set, the use of a 1.5 MHz insonation frequency and a peak rarefactional pressure amplitude of 3.5 MPa for the first insonation now significantly increases the likelihood of harmonic generation within the bandwith of the receiving array (4-11 MHz).

The analysis of this data set begins with the effect that the filtering approach has on the performance of PAM during the first insonation. As shown in Fig. 4.13, substituting the comb filter with the SOH model results in better containment of the mapped cavitation activity inside the channel in the case of the dual array configuration.

The two most likely explanations for this observation are that the majority of the cavitation activity outside the channel is either due to extravasation of nanocups and subsequent cavitation, or not real and potentially the result of harmonic energy (reflections from the walls of the channel) not efficiently removed by the comb filter. In order to further investigate this hypothesis, the spectra of the recorded signals when filtered with either the comb filter or the SOH model are presented in Fig. 4.14. The SOH model is able to filter out the harmonics present in the signal compared to the comb filter. Specifically, a leakage of harmonic energy is observed in the frequency bands surrounding the first and second harmonic, and this latent harmonic energy erroneoulsy classified as broadband is potentially the reason for the excessive extent of cavitation activity mapped outside the channel in Fig. 4.13 (row 1, column 3). Therefore, it seems more likely that the cavitation activity outside the channel is due to harmonic energy not efficiently removed by the comb filter.

Comparing the PAM maps generated for the same filtering method (i.e. the SOH model) but with different beamforming algorithms, RCB and RLPB, the localisation of the sources of inertial cavitation is once again significantly improved, particularly for the single array configurations (Fig. 4.13, rows 2 and 3, columns 1 and 2). In particular, by looking closely in the axial direction of the PAM maps generated by the second probe, the channel location could be anywhere in the span -4mm to +2mm in the case of RCB, while this range is significantly reduced for RLPB, spanning -2mm to 1mm, or a twofold improvement.

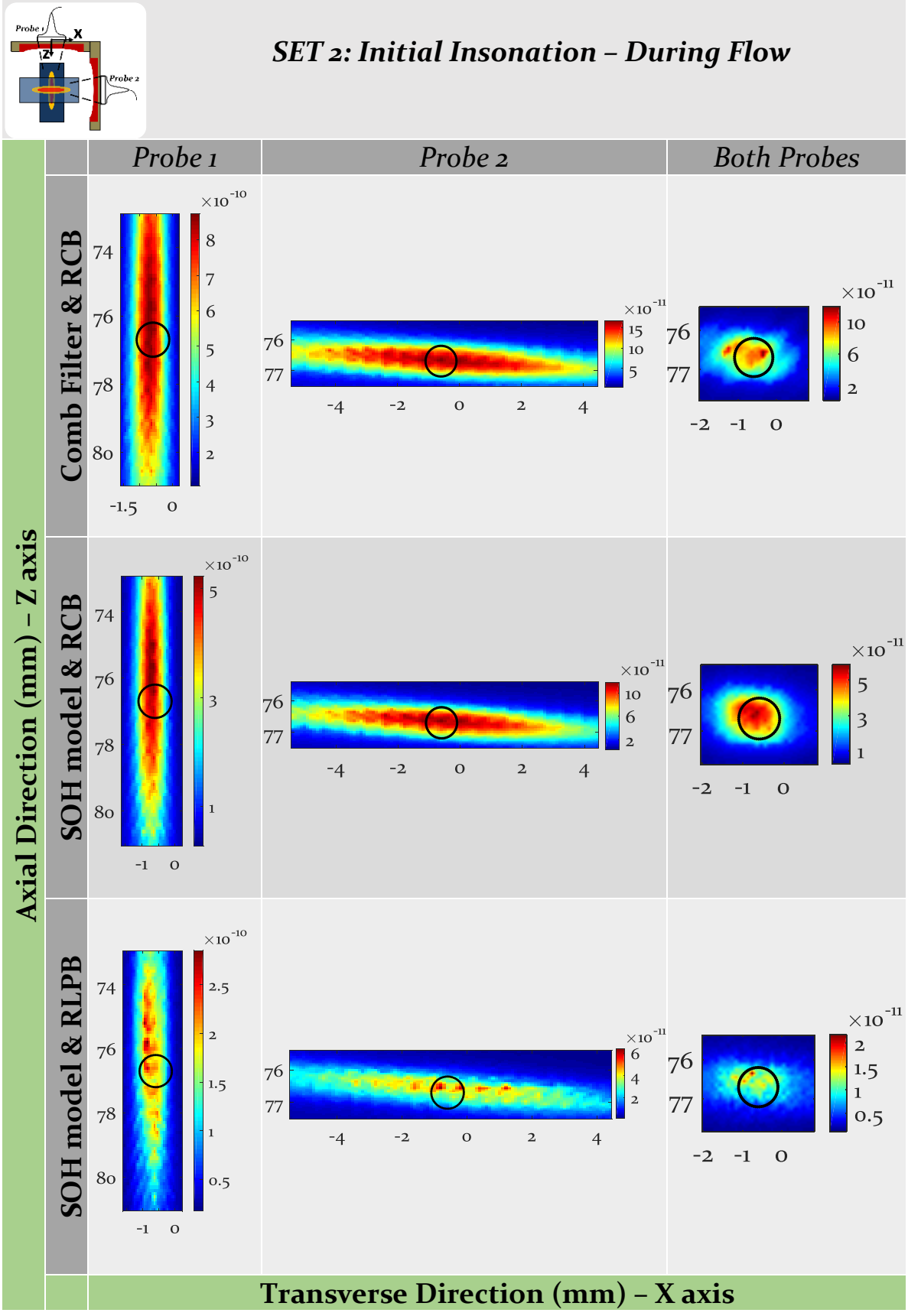


Figure 4.13 PAM maps corresponding to experimental set 2 during the first insonation (driving frequency = 1.5MHz) for single and dual array configurations and different combinations of filtering (comb filter or SOH model) and beamforming (RCB or RLPB) approaches. The location of the channel is indicated in each map with a black circle.

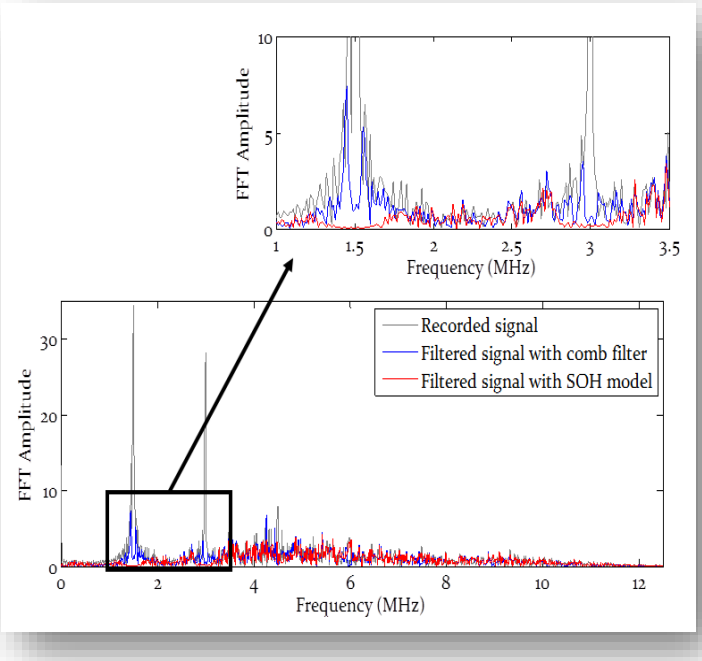


Figure 4.14 Spectral analysis of the RF signal recorded by the middle channel of probe 1 corresponding to the experimental set 2 during the first insonation (driving frequency = 1.5MHz), after being filtered with either a comb filter (bandwidth = 0.1MHz, order = 25) or the SOH model (polynomial order = 2, number of cycles = 8) for harmonic frequencies removal.

To confirm these observations a similar quantitative analysis, as that for set 1, is performed, and the results are presented in Fig. 4.15. As far as the effect of the filtering approach is concerned, a small decrease is observed in the percentage of the -1dB energy outside the region of interest when the comb filter is substituted by the SOH model for the single array configurations, and it becomes much more apparent, i.e. four-fold decrease, in the case of the dual array configuration. Additionally, by observing the extent of the area outside the region of interest, similar conclusions can be drawn. A clear decrease in the extent of the outside region is observed when SOH model replaces comb filtering, especially in the single array configurations.

In terms of the choice of the beamforming algorithm, the extent of the area outside the region of interest is reduced dramatically when RLPB replaces RCB, regardless of the array configuration. More precisely, in the case of RLPB the extent of this area is approximately 10% and 1% of the corresponding area for RCB in the case of probe 1 and probe 2 respectively. Finally, by comparing the energy in the region of

interest, the choice of the beamforming algorithm seems to have a significant impact only in the case of probe 2, where RLPB significantly outperforms RCB by estimating approximately 3 times more energy inside the region where cavitation is expected to take place, resulting in improved source localisation.

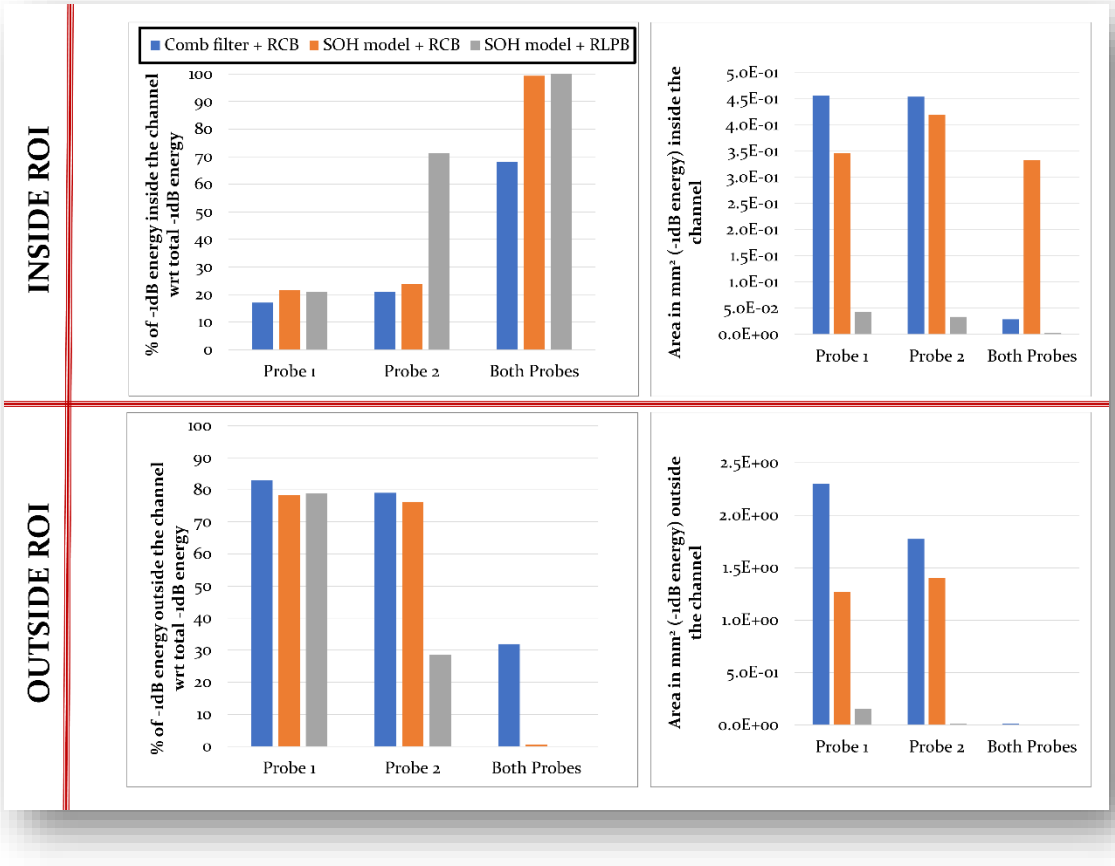


Figure 4.15 Quantitative analysis of the PAM maps corresponding to experimental set 2 during the 1st insonation. The percentage of the -1dB energy (i.e. energy on the PAM maps above the 80% of the maximum PAM energy displayed on the map) inside and outside the region of interest (i.e. the area of the channel) with respect to the total -1dB energy on the PAM maps is presented on the two left subfigures for all combinations of filtering and beamforming approaches, and for all array configurations. The two subfigures on the right present the area in mm^2 that the -1dB energy occupies inside (top subfigure) and outside (bottom subfigure) the channel for all possible combinations of filtering and beamforming methods, and all array configurations.

During the second insonation in this experimental set the driving frequency changes to 0.5MHz. Therefore, it is expected that the effect of the SOH model will not be as significant as during the first insonation, as already discussed in the analysis of the first experimental set. Indeed, as Fig. 4.16 suggests, cavitation is falsely mapped partly inside the channel for the dual array configuration regardless of the filtering approach (Fig. 4.16, rows 1 and 2, column 3), although clearance of the channel has taken place. This observation suggests that the point spread function of RCB, which is used in both of these maps, could be the reason for the incorrect mapping of activity inside the channel. Replacing RCB with RLPB results in significant improvement of PAM source localisation performance, since cavitation is now mapped only outside and on the boundaries of the channel (Fig. 4.13, row 3, column 3).

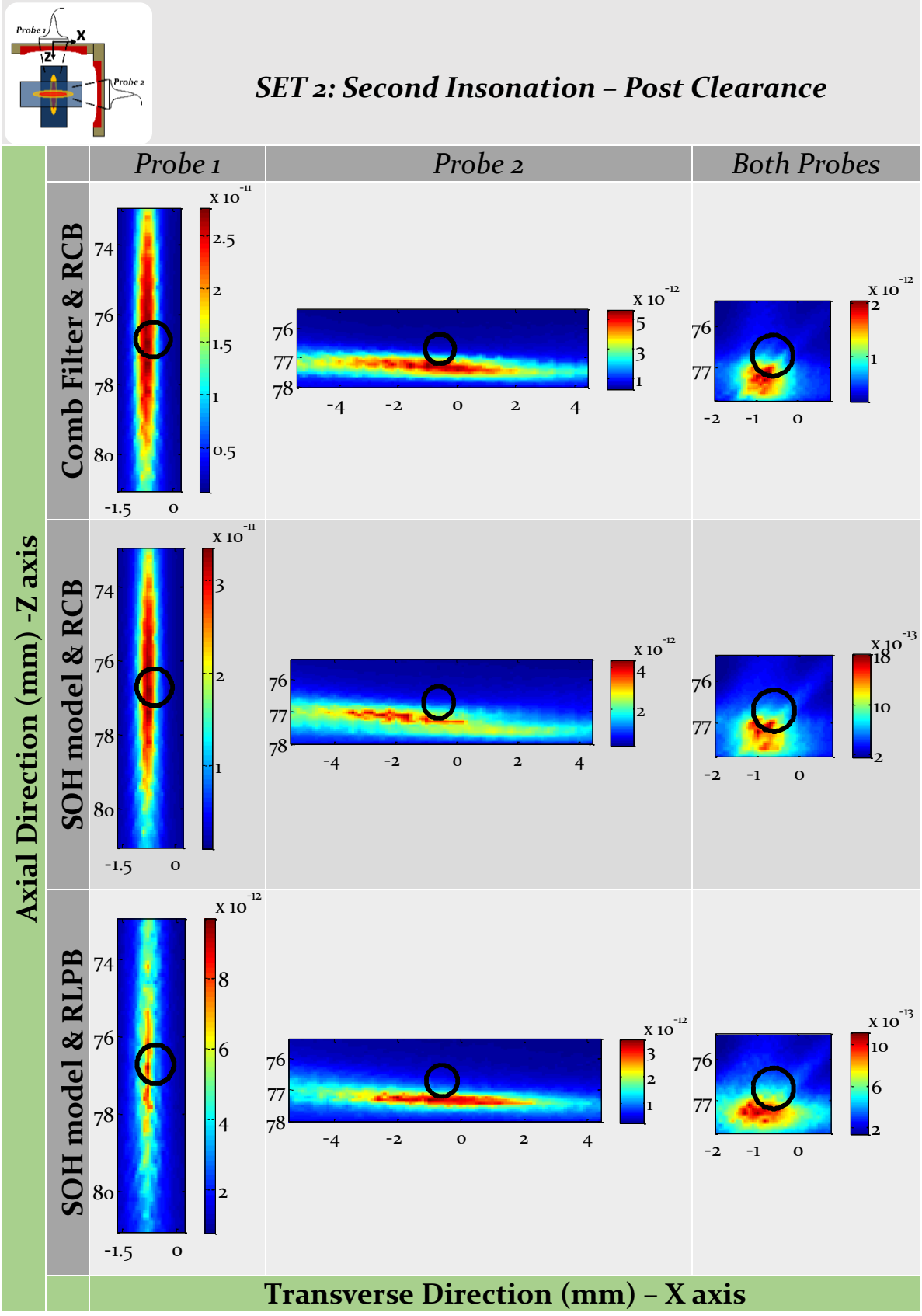


Figure 4.16 PAM maps corresponding to experimental set 2 during the second insonation, after channel clearance (driving frequency = 0.5MHz) for single and dual array configurations and different combinations of filtering (comb filter or SOH model) and beamforming (RCB or RLPB) approaches. The location of the channel is indicated in each map with a black circle.

Additionally, by studying the spectra of the recorded signals when filtered with either the comb filter or the SOH model (Fig. 4.17), the SOH model is found to effectively remove energy at the fundamental frequency, but fails to detect and remove energy at the second and third harmonic in this instance. The reason for that is potentially their low amplitude compared to the noise level, and, as it has been demonstrated in section 3.3, a low narrowband-to-broadband signal ratio could degrade the performance of the SOH model. It is, therefore, assumed that the relative relationship between the unfiltered energy at the fundamental frequency in the case of the comb filter, and the unfiltered energy at the second and third harmonic in the case of the SOH model will determine in this specific set of data which method performs more efficiently.

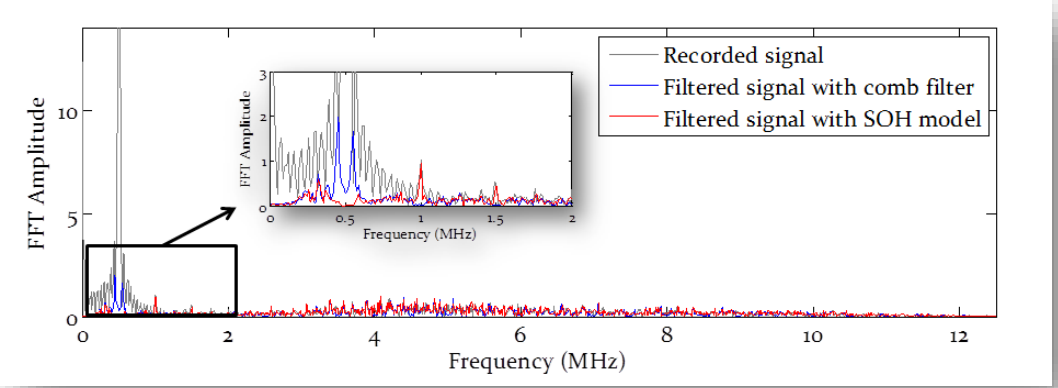


Figure 4.17 Spectral analysis of the RF signal recorded by the middle channel of probe 1 corresponding to the experimental set 2 during the second insonation (driving frequency = 0.5MHz), after being filtered with either a comb filter (bandwidth = 0.1MHz, order = 25) or the SOH model (polynomial order = 2, number of cycles = 8) for harmonic frequencies removal.

In order to study in further detail the effect of the beamforming algorithm on mapping the extent of extravasation, -1dB contours have been drawn (white lines) on the PAM maps corresponding to the single array configuration for the cases where the

SOH model has been applied, and either RCB or RLPB was selected as a beamforming approach (Fig. 4.18). The reason for presenting only the PAM maps for the second probe is that, as can be seen from the microscopy image (Fig. 4.18) and the dual array configuration PAM maps, the cavitation activity in this specific frame is located at the bottom of the channel with respect to probe 1. The better transverse resolution of probe 2 allows correct localisation of the source outside the channel regardless of the beamforming algorithm. However, the cavitation region is elongated in the axial direction due to the poor axial resolution of PAM with a single probe. However, Fig. 4.18 shows that for the case of RLPB the main -1dB contour coincides better with the location of the extravasated nanocups on the fluorescent microscopy image compared to RCB.

Quantitative analysis of the PAM maps in Fig. 4.16, similar to that performed for experimental set 1, is performed and the results are presented in Fig. 4.19. As far as the filtering approach is concerned, the observation that the choice for the applied filter does not have an obvious impact on the source localisation is reinforced by the results in Fig. 4.19. More precisely, no clear decrease in the percentage of the -1dB energy or the extent of the area of -1dB energy outside the region of interest is observed. On the contrary, the choice of the beamforming algorithm significantly affects the percentage of -1dB energy inside the region of interest. Especially for the single array configurations, the percentage of -1dB energy inside the region of interest is double for RLPB compared to RCB. Additionally, the extent of the area of -1dB energy outside the region of interest is dramatically decreased, by at least 90% when RCB is replaced by RLPB, in the case of probe 1. However, this is not the case for probe 2 or the dual array configuration, potentially due to the location of the sources with respect to each probe, and the corresponding axial and transverse PAM resolution.

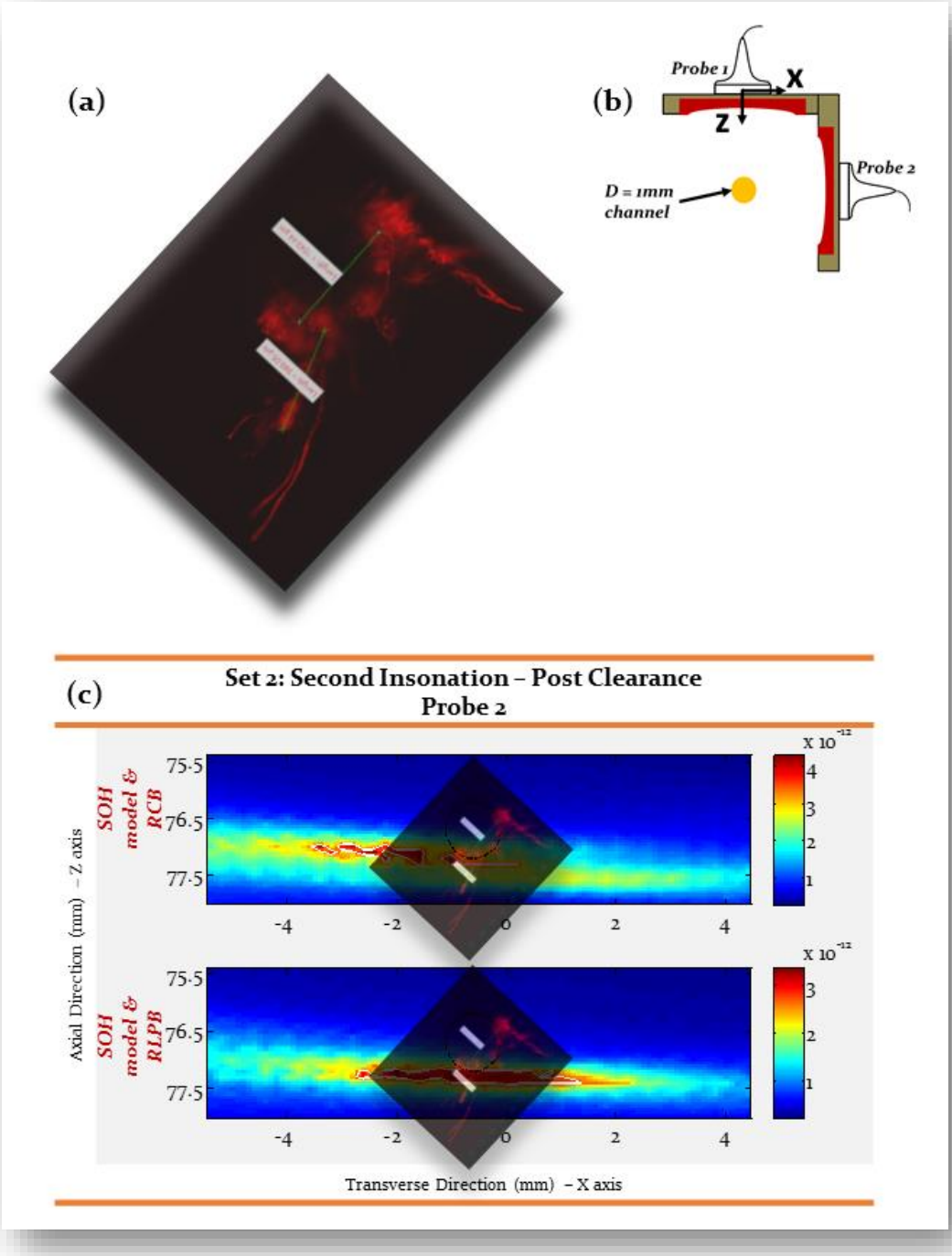


Figure 4.18 PAM maps (subfigure (c)) corresponding to experimental set 2 during the 2nd insonation, after channel clearance (driving frequency = 0.5MHz) for the single array configuration (probe 2). Fluorescent microscopy images are overlaid with the PAM maps to indicate the regions of extravasation. The RF data is filtered using the SOH model prior to PAM, and either RCB or RLPB are used as a beamforming technique. Contours corresponding to 80% of the maximum PAM energy for each map (-1dB contours) are displayed (white lines). The location of the channel is indicated in each map with a black dashed circle. A magnified version of the fluorescent microscopy image is presented at the bottom subfigure (subfigure (a)). A schematic of the experimental setup is presented in subfigure (a) to clarify the direction of the PAM maps in subfigure (c).

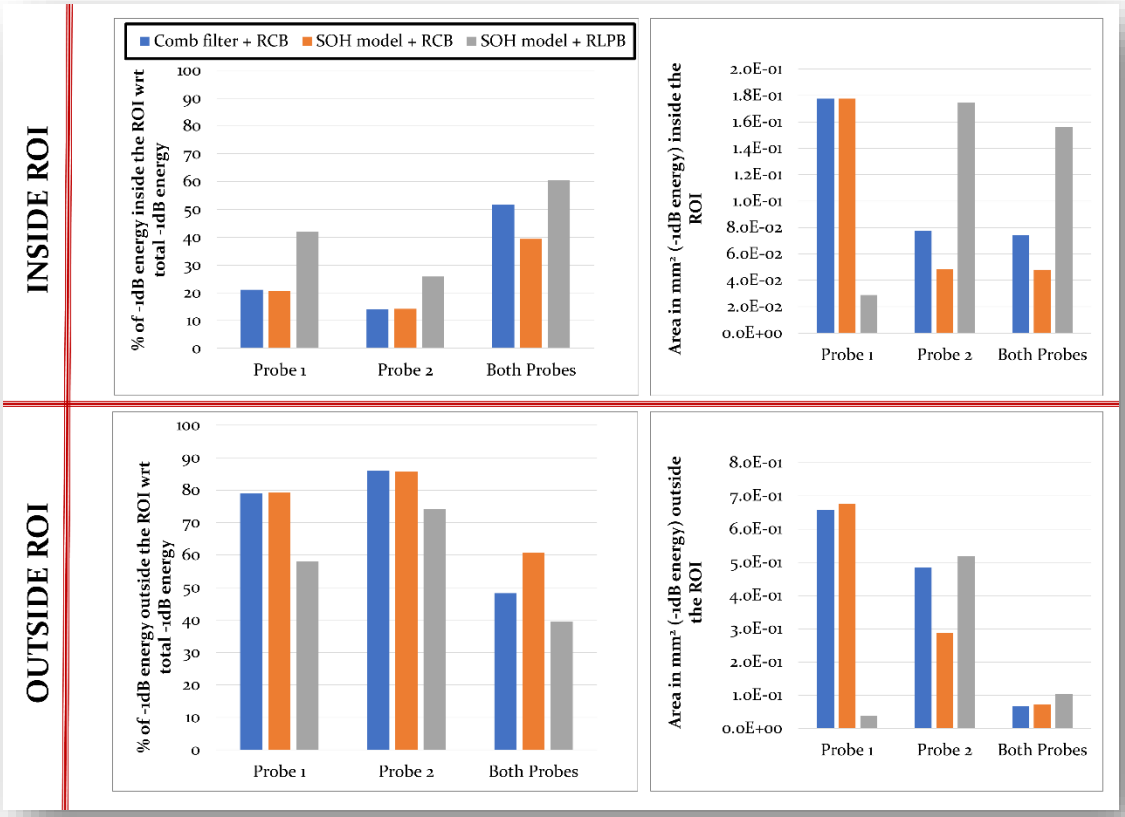


Figure 4.19 Quantitative analysis of the PAM maps corresponding to experimental set 2 during the 2nd insonation. The percentage of the -1dB energy (i.e. energy on the PAM maps above the 80% of the maximum PAM energy displayed on the map) inside and outside the region of interest (i.e. the area of increased fluorescence on the fluorescent microscopy images) with respect to the total -1dB energy on the PAM maps is presented on the two left subfigures for all combinations of filtering and beamforming approaches, and for all array configurations. The two subfigures on the right present the area in mm^2 that the -1dB energy occupies inside (top subfigure) and outside (bottom subfigure) the region of interest for all possible combinations of filtering and beamforming methods, and all array configurations.

Set 3 (First insonation at 0.5MHz, Second insonation at 1.5MHz)

During this experiment, the driving frequencies in the first and second insonation have been switched compared to the previous experimental set.

In the first part of the experiment, with flowing nanocups, expansion of the cavitation activity around the channel was observed, which was subsequently confirmed on the brightfield microscopy image presented in Fig. 4.20. The potential reason for the major channel damage observed is the high pressure amplitude applied. At moderate pressures, finger-like projections are expected, as observed in the previous two experimental sets, and potentially observed on the right part of the channel in Fig. 4.20. However, in this case, the high induced pressure at the focal region is likely to cause not only nanocups, but also the agar gel to cavitate. Such accumulation of cavitation events under these experimental conditions might lead not only to extravasation of nanocups but also to mechanical compromise of the channel, and it is potentially the reason behind the extended damage of the channel observed in Fig. 4.20.

Since PAM analysis of RF data during the first insonation at 0.5MHz driving frequency has already been presented (set 1), analysis of this experimental set will focus on the second insonation. After channel clearance, cavitation activity should only take place outside the channel. However, insonation at 1.5 MHz means that the confocal spot between the two HIFU transducers is now too small to excite the entire perivascular region. Therefore, only a portion of the ring of extravasated nanocups and potentially agar gel surrounding the channel will be able to cavitate, and this is expected to occur over a small perivascular region of characterstic dimension comparable to the wavelength at 1.5 MHz (on the order of 1 mm).

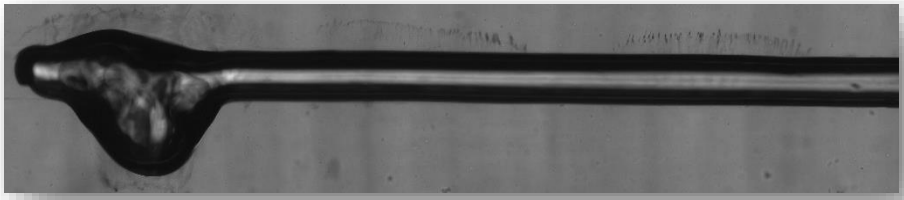
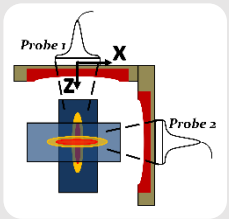


Figure 4.20 Bright field microscopy image along the channel corresponding to experimental set 3, indicating the location and extent of extravasation.

Multiple cavitation events are expeted to occur over the confocal region of the two transducers. The RF data chosen to produce Fig. 4.21 were chosen because they represent two simultaneous cavitation events ocurring within the field of view of both arrays. These two events can be clearly distinguished when the dual array configuration is used regardless of the filtering and beamforming method applied, due to the significant improvement in PAM resolution caused by the addition of the second array. However, when a single array configuration is used, the two events can only be distinguished by probe 2 because they are aligned transverseley to the array, a direction in which PAM resolution is significantly better than in the axial direction.



SET 3: Second Insonation – Post Clearance

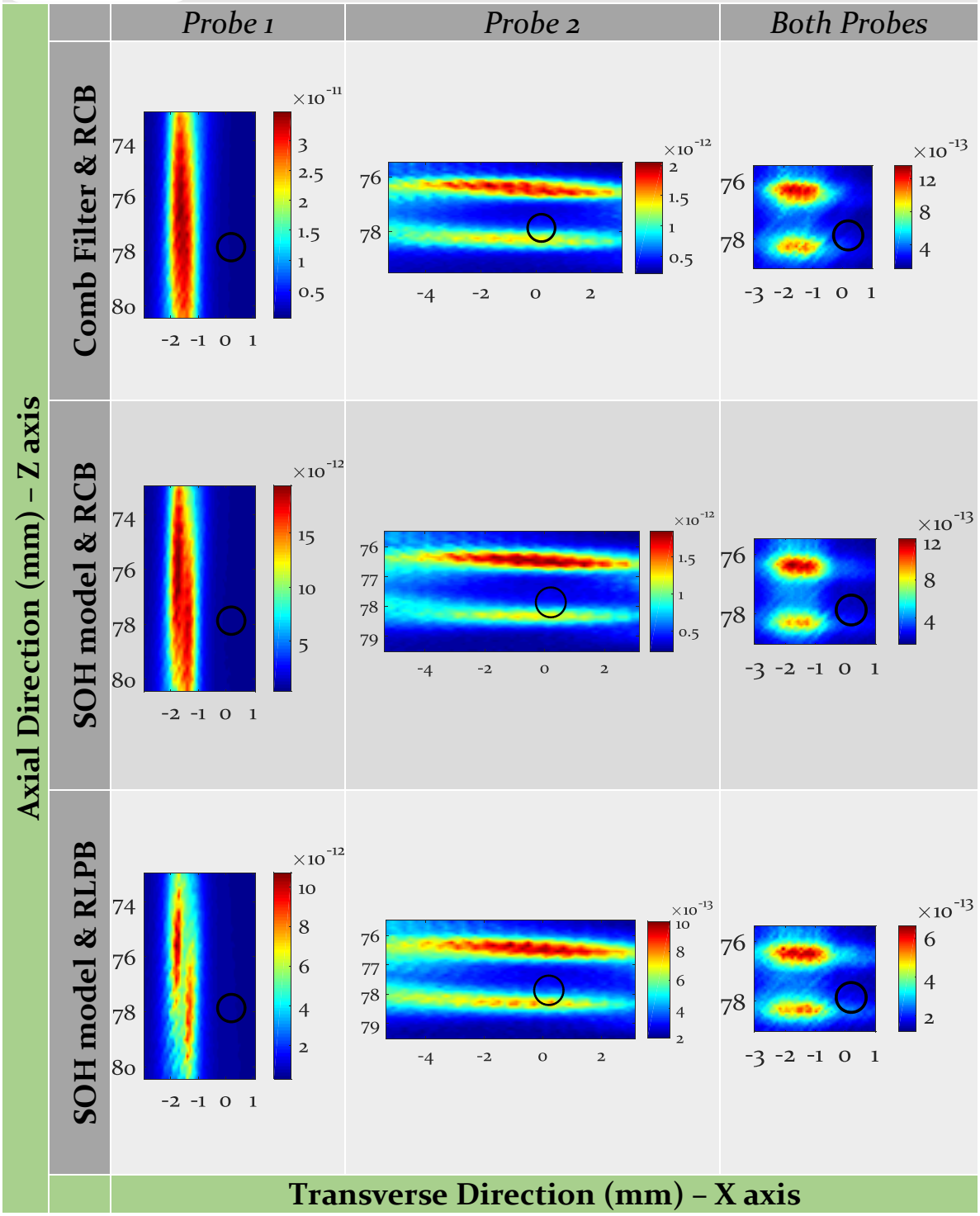


Figure 4.21 PAM maps corresponding to experimental set 3 during the second insonation, after channel clearance (driving frequency = 1.5MHz) for single and dual array configurations and different combinations of filtering (comb filter or SOH model) and beamforming (RCB or RLPB) approaches. The location of the channel is indicated in each map with a black circle.

Focussing, now, on probe 1, separation of the two events is only possible when a combination of the SOH model, as a filtering method, and RLPB, as a beamforming technique is applied. More specifically, when a comb filter is used to remove the harmonics present in the recorded signal compared to the SOH model, there is some leakage of harmonic energy that is not filtered out and is subsequently mapped on PAM as broadband energy.

This observation can be supported by the relative comparison of the spectra of the filtered signals from the middle element of probe 1 using either of the two filtering approaches (Fig. 4.22). The overestimation of broadband energy, considering the same beamforming algorithm, in this case RCB, leads to expansion of the cavitation region (Fig. 4.21 row 1 column 1). By contrast, when comb filtering is replaced with the SOH model, the separation of the two sources begins (Fig. 4.21 row 2 column 1), but they are still not clearly distinguishable. Finally, by altering the beamforming technique, a significant improvement in the resolution is observed in both axial and transverse PAM resolution. More specifically, the extent of each source in both directions is significantly reduced compared to RCB, and the location of the two sources can be estimated more accurately. The offset in the axial direction of approximately 2mm as demonstrated in the dual array PAM maps can now be approximated with higher accuracy. Additionally, the improvement in the transverse direction allows the complete separation of the two sources, which was not previously possible with RCB, making it possible for the first time to quantify the offset between the sources in this direction, which is estimated to be approximately 0.5mm.

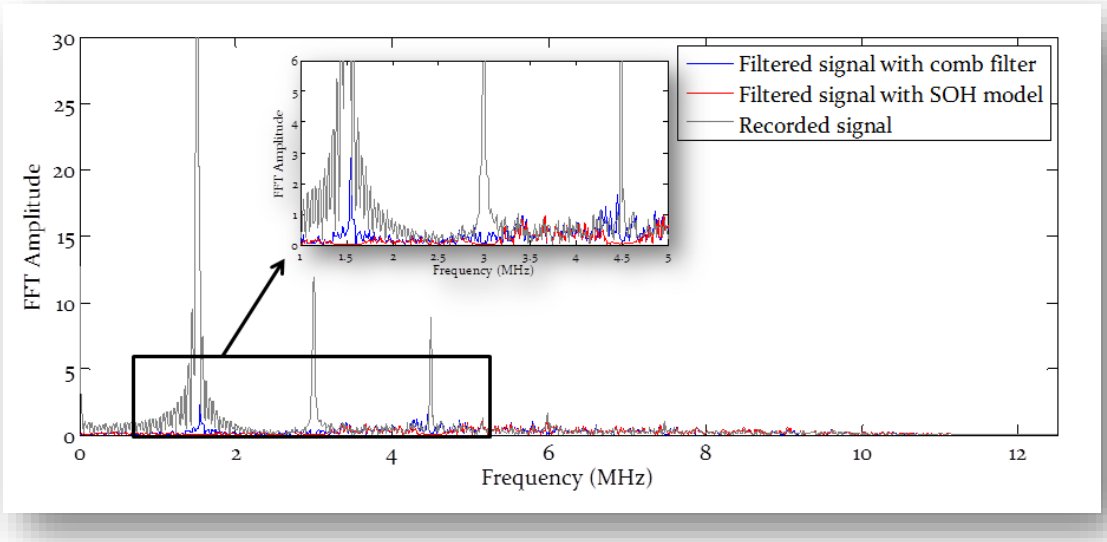


Figure 4.22 Spectral analysis of the RF signal recorded by the middle channel of probe 1 corresponding to the experimental set 3 during the second insonation (driving frequency = 1.5MHz), after being filtered with either a comb filter (bandwidth = 0.1MHz, order = 25) or the SOH model (polynomial order = 2, number of cycles = 8) for harmonic frequencies removal.

4.4 CONCLUSIONS

In the present chapter, a new generation of fluorescent sub-micron cavitation nuclei and a bi-static experimental apparatus utilizing two orthogonal HIFU transducers and PAM arrays was used to investigate the effect of the chosen filtration method and passive beamforming algorithm on the spatial resolution achievable by either one or two arrays in mapping sources of inertial cavitation, compared to an optical 'gold standard'. To enable assessment of the effect of filtration, both a frequency where no significant harmonic generation occurs (0.5MHz) and a frequency and amplitude where there is measurable generation of harmonics (1.5MHz, 3.5MPa) were used.

Across all cases, use of the SOH model on its own only yields significant improvements in the spatial definition of PAM maps for signals that contain a very significant narrowband component, typically captured under 1.5 MHz exposure. The

ability of the proposed data-adaptive filtering method to detect the number of harmonics present at any point in the recorded signal, along with the estimation of the time-varying amplitude of the harmonic signal, allows more accurate harmonic energy rejection, while avoiding unnecessary removal of broadband energy due to wide-bandwidth, fixed-order comb filters. It is expected that the effect of the SOH model will be more dramatic under *in vivo* experimental conditions. The multiple sources of reflections and nonlinear scattering, as well as the high attenuation of the signal-of-interest due to the propagation through multiple tissue layers will result in burring of the broadband signal into high-amplitude time-varying harmonic signals, whose removal with conventional comb filtering is extremely challenging.

On the other hand, replacement of the currently available data-adaptive beamforming algorithm, RCB, with the proposed RLPB beamformer has a very noticeable impact on the PAM resolution in almost all situations. More specifically, it has been consistently shown that the region of cavitation activity was significantly reduced by RLPB, matching more accurately the extent of the expected cavitation region with that displayed on the microscopy images. Additionally, more accurate localisation of the sources was achieved in the more clinically relevant single array configurations, and reliable distinction between the channel and the extravasation region is possible depending on the location of the extravasated region with respect to the array. Finally, in the presence of multiple simultaneous cavitating regions, the combination of the RLPB beamformer with SOH filtration was uniquely able to achieve correct separation and significantly improved localisation and estimation of the extent of such regions, compared to RCB. More precisely, sources approximately 0.5mm in the transverse and 2mm in the axial direction apart at a distance approximately 77mm away from the array (probe 1) are distinguished and correctly localised by RLPB, while

RCB identifies them as one cavitation region of approximate dimensions 1mm transversely by 7mm axially (Fig. 4.21). It is also important to note at this point that these results regarding source separation closely agree with the simulation results presented in section 2.3 (Part II). Separation of source regions is crucial for further improvement of the PAM spatial resolution. Application of super-resolution techniques for vascular imaging in the brain that employ deconvolution techniques based on the PSF of the imaging system has already been reported in the literature (O'Reilly and Hynynen, 2013). For such an approach to be potentially applied also in the present work, accurate localisation and separation of individual sources or clusters of sources is necessary. The improvement in PAM resolution provided by RLPB therefore paves the way for such approaches to be introduced in the context of PAM.

In conclusion, the proposed SOH model and RLPB are expected to enable significant improvements in the spatial accuracy of PAM as a monitoring technique *in vivo*. Assessment of the performance of the proposed methods under clinically relevant conditions, including a non-static environment with multiple tissue layers present in the propagation path, would be the next step towards the establishment of the potential and advantages of the technique over currently clinically available imaging methods.

4.5 REFERENCES

Kwan, J.J., Graham, S., Myers, R., Carlisle, R., Stride, E., Coussios, C.C., 2015. Ultrasound-induced inertial cavitation from gas-stabilizing nanoparticles. Phys. Rev. E 92, 23019.

Kwan, J.J., Lajoinie, G., de Jong, N., Stride, E., Versluis, M., Coussios, C.C., 2016. Ultrahigh-Speed Dynamics of Micrometer-Scale Inertial Cavitation from Nanoparticles. Phys. Rev. Appl. 6, 44004.

Kwan, J.J., Myers, R., Coviello, C.M., Graham, S.M., Shah, A.R., Stride, E., Carlisle, R.C., Coussios, C.C., 2015. Ultrasound-Propelled Nanocups for Drug Delivery. Small 11, 5305–5314.

Narayanan, J., Xiong, J.-Y., Liu, X.-Y., 2006. Determination of agarose gel pore size: Absorbance measurements vis a vis other techniques. J. Phys. Conf. Ser. 28, 83.

O'Reilly, M.A., Hynynen, K., 2013. A super-resolution ultrasound method for brain vascular mapping. Med. Phys. 40.

CHAPTER 5

CONCLUSIONS & FUTURE WORK

The overall aim of the present DPhil thesis was to enhance the performance of Passive Acoustic Mapping (PAM) in detecting and localising sources of acoustic emissions, and particularly inertially cavitating bubbles, in order to facilitate the clinical translation of this promising new technique.

The main conclusions from the research presented in this thesis are summarised here and set against this overarching objective. Additionally, areas of further validation and improvement that are likely to motivate future work are also identified and discussed.

5.1 CONCLUSIONS

The range of ultrasound-based therapies has been dramatically expanded in the last decade, seeking to exploit the full range of bioeffects generated by ultrasound in tissue. Despite its wide applicability, non-invasiveness, cost-effectiveness, and portability, the main barrier to widespread clinical adoption is the lack of a reliable, equally cost-effective monitoring technique that could provide meaningful treatment feedback, particularly in the context of cavitation-based therapies.

The ultrasound-based technique known as Passive Acoustic Mapping (PAM) could very well provide this missing link. This approach allows passive mapping of sources of acoustic activity using signals recorded from multiple sensors, and has the significant advantage of being able to provide concurrent monitoring with respect to the treatment. The wide range of areas where PAM has been already applied, ranging from monitoring cavitation-mediated drug release and drug delivery to opening of the blood brain barrier, indicates the great potential of the technique, while at the same time revealing the current limitations of the method that need to be addressed prior to clinical adoption.

An overview of ultrasound-based therapies, their underlying physical mechanisms and accompanying bioeffects was provided in Chapter 1. The currently available monitoring techniques were also critically presented, describing where Passive Acoustic Mapping could prove most useful. An extensive analysis of the principles and components of PAM was provided, and discussion of the PAM process pipeline revealed the main components of PAM that need to be optimised in order to improve the performance of the method in detecting and localising the sources of acoustic emissions.

As Fig.1.1 suggests, accurate detection and classification of the sources of interest by signal-of-interest isolation, as well as reliable localisation of these sources by high-performance signal beamforming, are the two parts of the PAM process that require further development and are expected to have a significant impact on the overall performance of PAM. The main three goals of this DPhil thesis, as presented in Chapter 1, can therefore be summarised as follows:

1. Optimal data-adaptive beamforming for improved spatial resolution and artefact suppression
2. Optimal signal-of-interest separation from interfering signals
3. Combination of the proposed methods in a challenging application where PAM spatial resolution is of great importance

In Chapter 2, the first challenge relating to optimal array signal beamforming was addressed. Robust Linear Programming Beamforming (RLPB), a new beamforming approach based on the minimisation of the higher-order statistics of the array output, was proposed as an alternative to the Robust Capon Beamformer (RCB), whose minimisation problem accounts only for the variance of the array output. Although both approaches are data-adaptive and allow correction for array calibration errors, the poor resolution of RCB especially in the axial direction was the motivation behind the investigation of a new beamforming method. Especially in clinically relevant scenarios, at longer targeting depths with multiple tissue layers present, and the necessity to separate sources of acoustic emissions that are relatively close, the source resolvability provided by the beamforming algorithm is crucial.

The performance of the two beamformers was initially compared in simulations. The emissions from a single or two bubbles were modelled using the Keller-Miksis model, and it has been demonstrated that both beamformers are able to accurately estimate the source energy of a single bubble as long as an accurate calibration of all the elements of the array is available. Additionally, the two-bubble scenario allowed comparison of the resolution limits in both the axial and transverse directions of RCB and RLPB. RLPB was found to outperform RCB, by being able to separate two cavitation sources at a distance of 0.08mm apart in the transverse direction, while the limit for RCB was 0.2mm. In the axial direction, even at a distance of 2mm between the sources (significantly smaller than the corresponding theoretical resolution), successful resolvability was observed for both RCB and RLPB. The difference between them is the level of the energy dip between the two source locations. In RLPB it is almost double, facilitating source resolvability and providing an indication of better performance.

In vitro experimentation consisting of cavitating regions rather than individual cavitating bubbles yielded similar conclusions. The ability of the two data-adaptive beamformers to separate two regions of cavitation at a fixed distance between them, arranged either along the transverse or the axial direction of the array, and at increasing depth with respect to the array, was investigated. It was shown that a 22% and 14% increase in the axial and transverse resolution respectively was achieved by RLPB compared to RCB. This promising outcome is the first indication that the application of more sophisticated beamforming approaches could successfully address the problem of PAM spatial resolution. However, further validation of the performance of the beamforming technique is required under *in vivo* experimental conditions with multiple sources of interference present. The ability of the beamformer to suppress interference

could then be evaluated, in situations where the ε parameter is expected to play a more significant role. Finally, it is important to comment on the computational cost of the two beamforming approaches, as this aspect is crucial for the real-time performance of PAM. In the case of RCB, the eigendecomposition of the covariance matrix of the array output is the most computationally demanding part of the process. On the other hand, RLPB requires the solution of a linear programming problem that could be solved using an interior-point method that has been proven to be robust in solving complex large-scale linear programs. The polynomial computational complexity of the algorithm could potentially limit the real-time execution of the algorithm, especially when large data sets are used as an input. Significant research has been reported attempting to lower the computational cost under certain conditions, and several software packages that implement different variations of the interior-point method are commercially available. Combination of such software with parallelisation of the PAM algorithm, by solving the linear programming problem simultaneously for multiple voxels of a grid on different cores of a CPU or a GPU, could lead to improved performance and higher PAM frame rate.

In Chapter 3, the improvement of the signal-of-interest detection in the presence of interfering signals was addressed by proposing the Sum-Of-Harmonics (SOH) model, a data-adaptive parametric model for estimation of sets of narrowband signals and subsequent estimation of the remaining broadband component. Depending on the application, the signal-of-interest could either be the broadband component , indicative of inertial cavitation, or the narrowband component, such as harmonics, sub- and super-harmonics, which arise from non-inertial cavitation. Under *in vivo* experimental conditions, it is expected that the driving frequency and its harmonics will dominate the spectrum of the recorded signals due to strong reflections from the multiple interfaces

in the signal propagation path, making it challenging to extract the broadband component. The signal-of-interest will potentially also be of lower intensity and occupy a higher frequency band, being, therefore, significantly affected by attenuation. Accurate classification of the signals according to their frequency signature, and reliable detection of the signal-of-interest prior to beamforming is thus crucial for the correct localisation of the acoustic sources of interest. The proposed time-domain parametric model for narrowband and broadband signal detection is expected to significantly outperform a pre-defined, with fixed characteristics, comb filter, especially under time-varying, *in vivo* conditions.

Simulations were performed to investigate the effect of the different parameters of the model, indicating that more accurate detection is achieved as the NBR increases. The choice of a polynomial function to approximate the variations in signal amplitude over time proved efficacious, and as the order of the polynomial function increases the estimation error decreases. Finally, splitting of the signal in several cycles parts improves the detection of amplitude changes, and allows parallelisation of the process that can significantly lower the execution time.

In vitro experimentation illustrated the value of the proposed SOH method in recovering a weak broadband signal in the presence of high-amplitude harmonic signals. PAM maps generated using the SOH model as a filtering approach provided reliable localisation of sources of inertial cavitation that spatially coincided with the physical area where cavitation nuclei are expected to be. On the other hand, the use of different pre-defined comb filters was unable to achieve similar performance in classifying narrowband and broadband signals, leading in some cases in partial narrowband signal rejection or broadband signal (signal-of-interest) loss depending on the fixed characteristics of the signal. As a consequence, PAM maps generated using

such non-data-adaptive filtering approaches either localise sources of inertial cavitation outside the expected region, or underestimate the source energy that led in some cases to misinterpretation of the onset of inertial cavitation.

As a general comment, it is important to point out that the proposed SOH method allows concurrent estimation of narrowband and broadband components, instead of rejecting one to estimate the other, and it could be used to simultaneously study multiple phenomena occurring simultaneously during ultrasound therapies. Finally, it has considerable potential as a signal classification and detection method not only in the context of PAM, but also in conventional ultrasound imaging or other imaging modalities.

Finally, in Chapter 4, a new generation of fluorescent sub-micron cavitation nuclei and a bistastic experimental apparatus utilizing two orthogonal HIFU transducers and PAM arrays was used to investigate the effect of the chosen filtration method and passive beamforming algorithm on the spatial resolution achievable by either one or two arrays in mapping sources of inertial cavitation, compared to an optical 'gold standard'. A first insonation was applied to extravasate the cavitation nuclei from the channel through which they were flowing. Following flushing of the channel, a second insonation was applied that was expected to excite cavitation only in the perivascular region.

Although the dual array configuration significantly improves the spatial resolution of PAM, it is not clinically relevant, and the main goal is to optimise the PAM resolution for single array configurations. It was shown that more accurate signal detection, and therefore, source localisation is achieved when the SOH model is used compared to a comb filter, especially when there is increasing overlap between the

driving frequency and its harmonics, and the receive bandwidth of the array. Although a dramatic improvement in PAM source localisation was not observed, the analysis presented was the first indication that more reliable narrowband signal detection (in terms of both number of harmonics present in the signal and energy in each of these frequency bands) was achieved with the SOH model compared to the comb filter. In a clinical context, high-amplitude harmonic signals due to nonlinear propagation, reflections and scattering are highly likely to hinder the detection of broadband signals at challenging depth, which could potentially be more efficaciously addressed by the SOH model than a pre-defined comb filter.

As far as beamforming is concerned, significant improvements in source localisation were demonstrated for RLPB, compared to RCB. More specifically, the region of cavitation activity mapped with RLPB was significantly smaller matching in multiple cases more precisely, compared to RCB, the extent of the region where nanocups have extravasated according to microscopy. Another important feature observed was the multiple source resolvability achieved by RLPB that could be used later on along with super-resolution imaging techniques to further improve PAM source localisation. This observation could be interpreted as a combination of improved PSF and interference suppression; however, such a conclusion would require further investigation to be validated. Future *ex vivo* and *in vivo* experimentation with the proposed combination of filtering and beamforming methods will provide further evidence on the PAM source localisation performance, and potentially reveal other limitations that need to be addressed prior to clinical translation.

5.2 FUTURE WORK

Throughout the research chapters in this DPhil thesis, several aspects of PAM have been discussed, different assumptions have been made complying with the chosen experimental conditions, and multiple results have been presented that could motivate points for future work, and they are all summarised and discussed here.

Both simulation and experimental results presented in Chapter 2 suggest a significant improvement in the spatial resolution of PAM due to the introduction of a data-adaptive higher-order-statistics-based beamformer, namely RLPB. However, further simulations and experimentation are required to validate these initial findings. More specifically, definition of the PSF both in simulations and *in vitro* experiments for a single inertially cavitating bubble is important in order to accurately determine the theoretical resolution limits of PAM based on RLPB. Additionally, previous work has shown that multi-bubbles interactions, which have not been addressed in the present work, are potentially one of the key reasons for PAM performance degradation. Such bubbles interactions should be modelled and further studied in order to determine the level of influence that they have on the performance of PAM in correctly distinguishing and localising multiple sources of cavitation activity. Additionally, detailed knowledge of the PSF of the system could be useful for combining PAM with super-resolution approaches, in which regions of cavitation activity could be de-convolved with respect to the PSF, and result in improvements in the spatial resolution of PAM.

Another parameter that is important in the performance of PAM is ε. As already discussed, a compromise between interference suppression ability and array calibration errors correction ability needs to be made when a value for ε is chosen. Ideally, an extra step of optimisation with respect to ε should be introduced in the PAM process,

according to specific criteria that might change depending on the application. However, this would be time-consuming, and would hinder real-time execution of PAM. Instead, a study initially in terms of simulations, could be performed to analyse the effect that errors in the sensors positions have on the performance of PAM for different values of ε. Such a study could potentially help de-correlate the impact of ε on PAM with respect to steering vector mismatches (array calibration errors) and interference suppression ability, and facilitate the choice of a pre-optimised value for ε, especially if an approximate array calibration is available.

A challenging scenario for PAM that could be encountered *in vivo* and has not been addressed in the present work is when the ratio of the signal-of-interest with respect to the background noise (SNR) is low. As discussed in Chapter 3, in cases where the broadband component of the recorded signal is buried amidst high-amplitude narrowband signals due to significant attenuation of the higher frequencies as the signal propagates through multiple tissue layers, the SOH model is able to retrieve it more accurately than a fixed comb filter. However, beamforming of this signal using either RCB or RLPB has not been tested in situations where the SNR is very low. The performance of the beamformer in low SNR conditions in conjunction with its ability to deal with multi-bubble interaction and interference suppression will also play a significant role in situations where adjacent sources of different intensity (potentially cavitating nanocups of different size) must be identified correctly and the correct energy assigned to each of them. Simulations of single bubbles of different radius, relevant to the expected sizes of nanocups, and varying distance between them could be the first step in order to assess the performance of the proposed beamformer under such demanding conditions.

As already mentioned, one of the parameters resulting in low SNR is the attenuation of the higher-frequencies of the signal-of-interest. Investigation of the attenuation profile with respect to frequency for different tissue types could enable attenuation correction of the signal prior to beamforming, and potentially improve the PAM quality. In the cases where the calibration of the array elements is available, it could also be incorporated in the pre-processing of the signals in order to de-convolve the signal from the array response and recover the source energy more efficiently, as already demonstrated in the simulations in Chapter 2.

One of the limitations of the beamforming algorithms currently proposed for PAM is that they do not account for changes in phase of the signals as they propagate through multiple layers of tissue. In *in vivo* conditions it is expected that the signal-of-interest will propagate through different tissue types, with different speeds of sound, until it reaches the array of detectors, causing changes in the phase of the signals. One way of addressing this issue would be to consider the optimisation of the l_∞-norm of the array response with respect to complex, instead of real, weights for the array elements, since complex weights applied on the signal of each detector can induce changes not only to its amplitude, but also to its phase. Such an alteration in the beamforming algorithm is expected to have a more significant impact under clinical conditions, and *in vivo* experimentation could assess the impact that such an alteration would have in source localisation achieved by PAM-RLPB.

As far as the SOH model is concerned, its performance was evaluated in *in vitro* experimental conditions and the results presented in Chapters 3 and 4 are very promising. The validation of the method *in vivo* is though yet to be performed. The non-static environment under clinical conditions with high-amplitude harmonics due to reflections from multiple tissue layers is going to alter the conditions imposed for the

SOH model. The narrowband components of the signal are expected to vary with respect to time (e.g. movement of different body structures due to breathing) more dramatically compared to *in vitro* static conditions, and attempts to approximate these amplitude changes with a polynomial function might not provide accurate results. At this point, different functions should be considered as alternatives depending on the recorded signals, and in order to achieve this access to multiple *in vivo* experimental data sets would be beneficial.

Finally, PAM as a real-time monitoring technique would require high frame rates, comparable to currently used monitoring techniques. In order to achieve real-time performance, real-time implementation of the individual components is required, which could be achieved by parallelisation of their multiple independent steps on the cores of the CPU or GPU. As far as the PAM process in general is concerned, a first level of parallelisation could be defined with respect to the voxels in the defined grid. Since the estimation of the source strength of a voxel is independent with respect to the other voxels in the grid, parallel, instead of serial, execution of all the steps in the PAM pipeline for all voxels could significantly improve the frame rate. Additionally, as far as the filtering and beamforming processes are concerned several commercially available software packages/libraries are available for solving nonlinear least squares and linear programming problems respectively implementing potentially different variations and algorithms. Selection of the appropriate software depending on criteria such as computational complexity and accuracy of the algorithm, and integration in the generally parallelised PAM algorithm could be an initial approach towards real-time implementation of PAM.